THE UNIVERSITY *of* EDINBURGH

THE UNIVERSITY *of* EDINBURGH

Universidad de Granada

Thermodynamic processes involved in wave energy extraction

Encarnacion Medina-Lopez

Joint PhD Programme

Thesis submitted in fulfilment of the requirements for the joint degree of Doctor of Philosophy - Energy Systems PhD - at the University of Edinburgh and Doctora - Programa de Doctorado en Dinámica de los Flujos Biogeoquímicos y sus Aplicaciones - at the University of Granada.

2017

Information

Thesis title

Thermodynamic processes involved in wave energy extraction

Author

Encarnación Medina López

Principal Supervisors

Prof Antonio Moñino Ferrando (Universidad de Granada) & Prof Alistair G.L. Borthwick (University of Edinburgh)

Second supervisors

Prof Asunción Baquerizo Azofra (Universidad de Granada) & Dr Tom Bruce (University of Edinburgh)

Date of submission:

1st September 2017

"Necesitamos especialmente de la imaginación en las ciencias. No todo es matemáticas y no todo es simple lógica, también se trata de un poco de belleza y poesía."

"We especially need imagination in science. It is not all mathematics, nor all logic, but it is somewhat beauty and poetry."

Maria Mitchell, 1818–1889
First American woman to work as a professional astronomer

Abstract

Wave energy is one of the most promising renewable energy sources for future exploitation. This thesis focuses on thermodynamic effects within Oscillating Water Column (OWC) devices equipped with Wells turbines, particularly humidity effects. Previous theoretical studies of the operation of OWCs have resulted in expressions for the oscillation of the water surface in the chamber of an OWC based on linear wave theory, and the air expansion–compression cycle inside the air chamber based on ideal gas theory.

Although in practice high humidity levels occur in OWC devices open to the sea, the influence of atmospheric conditions such as temperature and moisture on the performance of Wells turbines has not yet been studied in the field of ocean energy. Researchers have reported substantial differences between predicted and measured power output, and performance rates of OWCs presently coming into operation. The effect of moisture in the air chamber of the OWC causes variations on the atmospheric conditions near the turbine, modifying its performance and efficiency. Discrepancies in available power to the turbine are believed to be due to the humid air conditions, which had not been modelled previously.

This thesis presents a study of the influence of humid air on the performance of an idealised Wells turbine in the chamber of an OWC using a real gas model. A new formulation is presented, including a modified adiabatic index, and subsequent modified thermodynamic state variables such as enthalpy, entropy and specific heat. The formulation is validated against experimental data, and found to exhibit better agreement than the ideal approach. The analysis indicates that the real gas behaviour can be explained by a non–dimensional number which depends on the local pressure and temperature in the OWC chamber. A first approach to the OWC formulation through the calculation of real air flow in the OWC is given,

which predicts a 6% decrease in efficiency with respect to the ideal case when it is tested with a hypothetical pulse of pressure. This is important because accurate prediction of efficiency is essential for the optimal design and management of OWC converters.

A numerical model has also been developed using computational fluid dynamics (CFD) to simulate the OWC characteristics in open sea. The performance of an OWC turbine is studied through the implementation of an actuator disk model in Fluent®. A set of different regular wave tests is developed in a 2D numerical wave flume. The model is tested using information obtained from experimental tests on a Wells–type turbine located in a wind tunnel. Linear response is achieved in terms of pressure drop and air flow in all cases, proving effectively the applicability of the actuator disk model to OWC devices. The numerical model is applied first to an OWC chamber containing dry air, and then to an OWC chamber containing humid air. Results from both cases are compared, and it is found that the results are sensitive to the degree of humidity of the air. Power decreases when humidity increases.

Finally, results from the analytical real gas and numerical ideal gas models are compared. Very satisfactory agreement is obtained between the analytical and the numerical models when humidity is inserted in the gaseous phase. Both analytical and numerical models with humid air show considerable differences with the numerical model when dry air is considered. However, at the resonance frequency, results are independent of the gas model used. At every other frequency analysed, the real gas model predicts reduced values of power that can fall to 50% of the ideal power value when coupled to the radiation–diffraction model for regular waves. It is recommended that real gas should be considered in future analyses of Wells turbines in order to calculate accurately the efficiency and expected power of OWC devices.

Resumen

La energía undimotriz, o energía de las olas, es una de las energías renovables más prometedoras para el futuro. Esta tesis estudia la termodinámica de dispositivos de columna de agua oscilante (Oscillating Water Column, OWC). Estudios previos sobre este tipo de dispositivos ofrecen expresiones para la oscilación de la columna de agua dentro de la cámara del dispositivo basadas en teoría lineal de ondas, así como de los fenómenos de expansión y compresión del aire dentro de la cámara basados en teoría de gas ideal.

Aunque en la práctica altos niveles de humedad se presentan en zonas costeras, la influencia de diferentes condiciones atmosféricas (tales como temperatura y humedad) en el rendimiento de turbinas Wells no ha sido estudiado en el campo de las energías marinas. Distintos informes apuntan a diferencias sustanciales entre potencia estimada y potencia obtenida en distintas plantas en operación. El efecto de la humedad en la cámara de aire del OWC provoca cambios en el entorno de la turbina, modificando su funcionamiento y eficiencia. La humedad contenida en la cámara de aire se plantea como causa de las diferencias de potencia observadas.

Esta tesis presenta el estudio de la influencia de aire húmedo en el funcionamiento de una turbina Wells en la cámara de un OWC usando un modelo de gas real. La formulación que se presenta a continuación incluye la modificación del índice adiabático, y la consecuente modificación de las distintas variables de estado, tales como entalpía, entropía y calor específico. La formulación es validada con datos experimentales, mostrando una mejor aproximación a las condiciones de laboratorio que el modelo clásico de gas ideal. El análisis indica que el comportamiento del gas real puede explicarse con el uso de un número adimensional que depende de la presión y la temperatura.

Una primera aproximación a la formulación del OWC se realiza a través del cálculo del flujo de aire a través de la turbina con el modelo de gas real, observándose una disminución en eficiencia del 6% frente al modelo ideal cuando se considera un pulso de presión ideal.

Más adelante se desarrolla un modelo numérico basado en CFD (Computational Fluid Dynamics) para simular las características del OWC en un canal de oleaje. El funcionamiento de la turbina Wells se simula mediante el uso de un modelo de disco actuador (Actuator Disk Model, ADM) en Fluent®. Se ensayan distintos oleajes regulares en un canal 2D, y estos se calibran con ensayos de laboratorio de oleaje en el canal, y de funcionamiento de una turbina Wells en túnel de viento. La respuesta lineal entre presión y caudal es obtenida para la turbina, demostrando la aplicabilidad de los ADMs al estudio de dispositivos OWCs.

Este modelo numérico se aplica primero en condiciones de aire seco, modificando después las condiciones del mismo para simular el aire húmedo. Los resultados muestran que la potencia del dispositivo depende del grado de humedad del aire, decreciendo la potencia disponible cuando aumenta la humedad.

Finalmente, se comparan los resultados del modelo teórico y el modelo numérico con aire seco y aire húmedo, obteniendo resultados similares para el modelo teórico de gas real y el modelo numérico con humedad. Ambos se diferencian considerablemente del modelo numérico con aire seco, salvo para condiciones de resonancia, donde los resultados son independientes del modelo de gas usado. En los demás casos, el modelo de gas real predice diferencias de hasta el 50% respecto a la teoría clásica cuando este se acopla con el modelo de radiación-difracción frente a oleajes regulares.

Acknowledgements

First and foremost, I would like to thank my supervisors, Prof Antonio Moñino Ferrando, and Prof Alistair Borthwick, for the tremendous amount of support and encouragement received over the past years. They were a fantastic team to work with, and made me grow to become a better engineer, and most important, a better person.

I would also like to thank Prof William Allsop for his guidance and support when I decided to start a PhD, and for infecting me with his enthusiasm in maritime engineering. I am also very grateful to Dr Aggelos Dimakopoulos for introducing me to the world of numerical modelling. To them, and to all the people at HR Wallingford, thank you for those very important months that brought me to this point.

The Policy and Innovation Group of the University of Edinburgh played a key role during the development of this thesis. They helped me understand how my research could be applied in the real world, and I discovered with them a new side of marine energy. For this and more, I would like to extend my gratitude to Mr Henry Jeffrey and the amazing PIGs. I want to thank Dr Adrian de Andres, he supported me unconditionally, and from him I learned how to think different. I would also like to thank my colleagues at the University of Granada. The "Grupo de Dinámica de Flujos Ambientales" has been my home for a long time. My path in marine energy started there, and their motivation helped me understand the marine energy field from a different perspective.

I am truly grateful to all my friends in the Institute for Energy Systems, and particularly to Yvonne, Anna, Kevin, Philip, Valerie, Thomas, and Manuel, these

past few years would have been very difficult without their support. The good times we spent together are a fundamental part of this thesis.

Quiero agradecer especialmente a mis padres, Encarni y Benjamín, por ser el ejemplo de esfuerzo y superación que ha marcado mi camino desde siempre. A mi hermana Ana, porque ella es la que me hace creer que puedo conseguir lo que me proponga. Y a mi abuela Encarna, por esperar siempre lo mejor de mí.

Y finalmente, a Leo. Él ha sido la voz de la razón y de la serenidad durante estos últimos diez años de mi vida. Él es mi apoyo, pero sobretodo es la persona que me hace querer ser mejor. Gracias por arriesgarte, por motivarme, por escucharme. Gracias por acompañarme en este largo camino.

Declaration

I declare that this thesis has been composed solely by myself and that it has not been submitted, either in whole or in part, in any previous application for a degree. Except where otherwise acknowledged, the work presented is entirely my own.

Encarnacion Medina-Lopez
September 2017

Declaración

El doctorando Encarnación Medina López y los directores de la tesis Antonio Moñino Ferrando y Alistair G.L. Borthwick, garantizamos, al firmar esta tesis doctoral, que el trabajo ha sido realizado por el doctorando bajo la dirección de los directores de la tesis y hasta donde nuestro conocimiento alcanza, en la realización del trabajo se han respetado los derechos de otros autores a ser citados, cuando se han utilizado sus resultados o publicaciones.

The PhD candidate Encarnacion Medina-Lopez and the supervisors Antonio Moñino Ferrando and Alistair G.L. Borthwick, guarantee by signing this thesis that the work has been developed by the PhD candidate under the supervision of the thesis supervisors. As far as our knowledge reaches, the rights of other authors to be cited when their results or publications are used have been respected.

Septiembre de 2017.

Directores de la Tesis (Supervisors) Doctorando (PhD candidate)

Fdo.: Fdo.:

Contents

List of Tables

List of Figures

Chapter 1

Introduction

1.1 A brief introduction to ocean energy

The major influx of energy to our planet is in the form of solar energy, which drives atmospheric wind circulation. Surface shear between wind and the free surface of large water bodies, like oceans and seas, causes the generation of gravity waves. Wave energy is available in all oceans and seas and has huge potential, given that the Sun exports about 1×10^{15} MWh/year of energy to the Earth. The energetic potential of waves has been estimated as more than 2×10^{12} MWh/year, United Nations (2000). This amount is higher than all the wind energy potential on Earth (1.5×10^{12} MWh/year).

Like wind, ocean energy is diffuse, which makes energy extraction difficult. Technical approaches to ocean energy have been studied since the 1980s, whereas wind energy conversion to electricity has been studied for more than 100 years (the first windmill used for production of electricity was built by Prof James Blyth in Scotland, July 1887, Price (2005)). Furthermore, windmills have been used for mechanical power for more than two millennia. Considerable advances have therefore taken place in our understanding of wind energy extraction, and these provide a useful template for more recent studies of ocean energy devices, in particular tidal stream power turbines.

Ocean energy resources can be divided into four types, United Nations (2000) and Uihlein & Magagna (2016):

- Tidal energy — Energy transferred to oceans from the Earth's rotation through gravitational attraction involving the Sun and Moon. This can be divided into two subtypes: tidal range and tidal current.
- Ocean wave energy — Mechanical energy from wind retained by waves.
- Ocean thermal energy — Energy stored in warm surface waters that can be made available using the temperature difference with water in ocean depths.
- Salt gradient energy — Energy coming from salinity differences between freshwater discharges into oceans and ocean water.

Currently, all ocean energy technologies except tidal range can be considered to be at an early stage of development, ranging from the conceptual stage up to the demonstration stage. Ocean wave and tidal current energy are the two types of ocean energy which are most advanced, and are expected to contribute significantly to the supply of energy in future. The other sources of energy are not considered sufficiently mature. Although many projects have been developed in the last decade, and plants are being tested, they have not reached the expected power, Uihlein & Magagna (2016).

Tidal current has been assessed during recent years for several candidate sites around the world. In certain cases, direct measurements have been performed *in situ*. In the past decade numerical modelling techniques have been increasingly applied to assess tidal current energy resources by simulating current velocities, Uihlein & Magagna (2016). Recent studies have also assessed the hydrodynamic effects of power extraction and consider changes to the flow field, change in water surface elevation, and disturbances in tidal dynamics, (see *e.g.* Serhadlıoğlu *et al.* (2013)).

As with tidal stream power, ocean wave energy resources have also been the subject of assessment in recent years. The first wave energy resource assessments were made using buoy data limited to local conditions, Gonçalves *et al.* (2014). The second generation of assessments included buoy data in combination with deep water numerical models which can assess offshore wave resources and overcome the limitations of first generation assessments, Gonçalves *et al.* (2014). More recent tools incorporate radar measurements and model wave generation and propagation

in coastal regions, Uihlein & Magagna (2016). Wave forecasting is performed by statistical techniques or physical models. An example of a wave forecasting system based on physical models is the wave model WAM that is incorporated into the Integrated Forecast System (IFS) of the European Centre for Medium–Range Weather Forecasts (ECMWF), Reikard (2011).

Wave Energy Converters (WECs) are devices used to convert wave energy into electricity. There are many technologies applicable to wave energy conversion, but most of them can be categorised as attenuators, point absorbers, over–topping devices, submerged pressure differential devices, oscillating wave surge converters, bulge systems, rotating mass devices, and oscillating water columns, AquaRET (2012).

Attenuators are long structures compared with the wavelength and are placed in parallel to the wave direction. Attenuators are composed of a series of cylindrical sections linked together by flexible hinged joints that allow individual sections to rotate relatively to each other, López *et al.* (2013). An example of an attenuator device is Pelamis, Pelamis Wave Power (2017).

Point absorbers are significantly smaller regarding the diameter. They collect energy in all directions through their movement. These devices generate electricity from their bobbing or pitching actions, by converting the up–and–down pitching motion of the waves into rotary movements, or oscillatory movements, López *et al.* (2013). An example of a point absorber is the PowerBuoy device, Ocean Power technologies (2017).

Over-topping devices are those in which waves cause a structure to increase its potential energy, kinetic, or both. Water is forced to pass over the structure to a reservoir above sea level, and is later released back to the sea through turbines. An example of an over–topping device is the WaveDragon, Wave Dragon (2017).

Submerged pressure differential devices consist of point absorbers typically located near the shore and fixed to the seabed. Such devices use the pressure difference generated between the wave crests and troughs as waves pass over the devices. An example of a submerged pressure differential device is the Archimedes Wave Swing, Archimedes Wave Swing (2017).

Another type of WEC device is the oscillating wave surge converter. These are

articulated or flexible structures positioned perpendicular to the wave direction. In this way, the oscillating wave surge converter moves back and forth due to wave impact, López *et al.* (2013). An example of an oscillating wave surge converter is the Oyster device, Aquamarine's Oyster (2017).

Water pressure or bulge systems consist of a tube filled with water, moored to the seabed, which is oriented heading into the waves. The water enters through the stern and the passing waves cause pressure variations along the length of the tube, creating a "bulge". As the bulge travels through the tube it grows, gathering energy, AquaRET (2012). An example of bulge wave system is Anaconda, Anaconda (2017).

Rotating mass point absorbers use the movement of the device, either by heaving or swaying. This motion drives either an eccentric weight or a gyroscope causes precession. In both cases the movement is attached to an electric generator inside the device, AquaRET (2012).

Finally, Oscillating Water Columns (OWCs) are partially submerged, hollow structures. The device is open to the sea below the water line, enclosing a column of air on top of a column of water. Waves cause the water column to rise and fall, which in turn compresses and decompresses the air column. This trapped air is allowed to flow through a turbine, which usually has the ability to rotate regardless of the direction of the airflow. The rotation of the turbine is used to generate electricity.

Figure 1.1 provides sketches of the main different types of WEC devices.

WECs can also be classified according to the location of the device as "on–shore", "near–shore", in the "shallow–water region", and "deep–water off–shore".

Several prototype OWC devices have been constructed and operated with different degrees of success over the last decades. Examples of on–shore, near–shore and breakwater OWC devices include Limpet (Scotland), Mutriku (Spain), and Pico (Portugal), The Carbon Trust (2005).

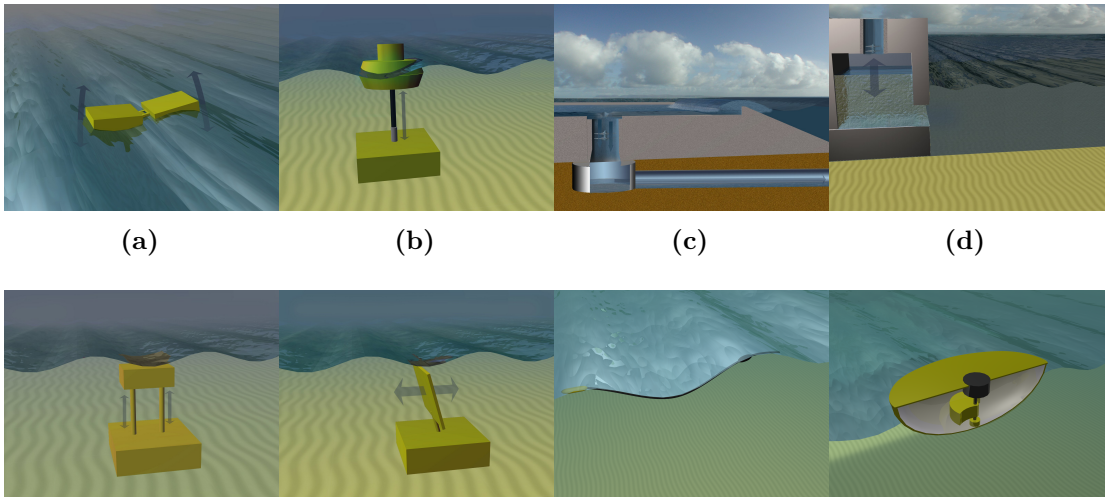

(a) (b) (c) (d)

(e) (f) (g) (h)

Figure 1.1: WECs devices; (a) attenuator, (b) point absorber, (c) over-topping, (d) oscillating water column (OWC), (e) submerged pressure differential, (f) oscillating wave surge converter, (g) water pressure or bulge system, (h) rotating mass point absorber. [Source: AquaRET (2012)]

1.2 Literature review

Ocean energy offers future opportunities for device developers and stakeholders working in renewable energy technology, and in 2009 presented the highest annual growth rate in the sector (Krewitt *et.al* (2009)). To bring forward such technology, research is being undertaken aimed at field deployment of single prototypes and arrays of wave energy converters (WECs). The OWC has been the subject of much dedicated research (Falcão (2010)) and is one of the few devices to have been tested at full scale under prototype conditions (Cruz (2008)). Oscillating water columns are composed of a chamber in which air is compressed and expanded by wave action. The energy transmitted to air is converted to power by passing air through a turbine, The Carbon Trust (2005).

Much research attention has focused on the effect of key parameters on the performance of OWCs in delivering power to the grid (see e.g. Medina-Lopez *et al.* (2016)). OWCs are found to be sensitive to power take-off (PTO) performance, turbine and air flow dynamics, the effect of random sea states, control strategies, and optimization. Among others, Gato & Falcão (1984), Gato & Falcão (1989),

Raghunathan (1995), and Sarmento *et al.* (1990) have carried out detailed studies of the technical behaviour of the Wells turbine when used as a PTO device. Korde (1991) identified mechanical improvements to the PTO device, and Jeffery (1984) suggested methods to handle the random nature of sea waves based on signal control. Researchers have proposed ways to maximize turbine efficiency, based on direct control of either the turbine rotation dynamics (Gato & Falcão (1989), Justino & Falcão (1999), and Falcão (2002)), or the air flow through the turbine shaft (Falcão & Justino (1999)).

Accurate power and efficiency predictions are prerequisites in the design analysis of an OWC converter. According to SI Ocean (2014), reliable prediction of energy extraction leads to improved design, better management during service time, increased annual energy production, and lower capital and operating costs. Observed deviations between results from ideal gas theory and experimental measurements provide a first approach to investigating the differences between predicted and actual power efficiency values in OWC plants currently under development (The Carbon Trust (2005)). Predicted efficiency values for wave-pneumatic-electric conversion fall within the 40 - 70 % range, whereas observed values fall as low as 10 %. This is especially relevant to the deployment of devices in less energetic wave climates such as the Mediterranean Sea (Stefanakos et al. (2004)). In such cases, efficient performance of the converter is vital, noting that Jalón *et al.* (2016) have found that optimal device performance can be attained in waves of peak periods about $6 \simeq 7\,s$.

From a theoretical standpoint, the physics of an OWC is usually described mathematically in terms of a classical radiation–diffraction problem, following Evans (1982), Sarmento & Falcão (1985) and Evans & Porter (1995). Reviews of the mathematical formulation and various analytical solutions accounting for boundary conditions imposed by either a coastline or a breakwater are given by Martins–Rivas & Mei (2009–I) and Martins–Rivas & Mei (2009–II).

Previous theoretical research on air compression and expansion inside an OWC has assumed the processes to be adiabatic involving ideal gas, without accounting for prevailing atmospheric conditions. Even when the assumption that a process is adiabatic appears totally justified (see e.g. Falcão & Justino (1999) and Sheng *et al.* (2013)), local temperature and moisture conditions might lead to deviation

from the polytropic ideal gas model. In fact, air confined inside the chamber and surrounding the OWC is a mixture of dry air and water vapour under ambient sea conditions. The influence of air temperature and moisture on turbine performance is well known in the case of gas turbines and power plants (see e.g. Yang & Su (2004), Ibrahim & Rahman (2010) and Singh & Kumar (2012)). It is therefore expected that such ambient conditions will influence the performance of the PTO turbine system of an OWC device.

In a study of deviations from ideal gas behaviour of the steady flow of an air-water vapour mixture through an OWC chamber model, Medina-Lopez *et al.* (2016) found that, in order for mass flow and enthalpy to remain conservative over a given pressure drop, the temperature change through the turbine could not be obtained assuming an ideal adiabatic polytropic process. A temperature correction had therefore to be applied in accordance with a real gas equation of state based on the virial expansion (Prausnitz (1999)). Estimates of pneumatic power using the real gas equation of state were lower than obtained using an ideal gas model (Medina-Lopez *et al.* (2016)). In the general field of thermodynamics, many researchers have formulated models in terms of the virial expansion coefficients for the polytropic process of a real gas (examples include Malic (1955), Pitzer & Curl (1957), Gel'man & Smolkin (1966), El–Twaty & Prausnitz (1981) and Wisniak (2003)). Use of virial coefficients in deriving the equations of state for real gases has been predominantly undertaken in the context of the chemical industry (Tsonopoulos (1974) and Tsonopoulos & Heidman (1990)). This has brought forward a useful methodology by which to calculate the system variables of a real gas in terms of variations from ideal gas values. A preliminary study by Medina-Lopez *et al.* (2016) has shown that application of real gas formalism to the air–water vapour mixture in an OWC is required for the accurate prediction of OWC efficiency.

In recent years, numerical simulation has become a powerful tool for the study of wave energy converters, Whittaker (2003). Numerical simulation provides a framework in which specific aspects of the OWC response can be extensively analysed under conditions otherwise unattainable in prototypes or test facilities. This has facilitated further research investigations into OWC optimization. Teixeira *et al.* (2013) used numerical flumes to study the coupling between aerodynamic and

hydrodynamic processes inside the chamber, and to examine the effect of chamber geometry and turbine parameters on OWC performance.

Gkikas & Athanassoulis (2014) and Davidson *et al.* (2015) used linear and non–linear system identification methods to study the multi–frequency excitation of water within an OWC chamber. López *and co-workers* (López & Iglesias (2014), López *et al.* (2014), López *et al.* (2015)) carried out numerical simulations to study OWC performance related to different turbine damping values and tidal level variations. Representation of the power take-off system can also be analysed numerically, Bingham *et al.* (2015). Such models have led to the further development of system identification models which have been applied to wave energy converters in several ways. Starting from numerical simulation, identification models allow the representation of the performance of wave energy converters based upon an impulse–response scheme when it is difficult to describe mathematically all the governing processes. Certain cases deal with the simulation of OWC processes such as damping and tide influence, based upon neural networks, López & Iglesias (2014). In other cases, full black-box parametric models have been carried out to study wave energy converters, Gkikas & Athanassoulis (2014), Davidson *et al.* (2015).

A recent study by Jalón *et al.* (2016) investigated maximization of energy extraction according to the time scale considered (sea state, season, year). Further steps have also been taken to improve OWC design not only in terms of technological features, but also in the minimization of environmental impacts and subsequent restoration costs. Research has been carried out on the advantages of using OWC devices as coastline protection elements by Abanades *et al.* (2014) and Mendoza *et al.* (2014), and for enhanced energy dissipation in breakwater structures by He & Huang (2014).

1.3 Motivation and aim of the thesis

This thesis focuses on an improved understanding of the performance of oscillating water columns (OWCs) as wave energy converters, following Medina-Lopez *et al.* (2016). The present standard OWC formulation is based on ideal gas theory with further considerations of compressibility or incompressibility, but without implementing real gas features. Although such features might be negligible

when interpreting the process of conversion from wave to pneumatic energy, the properties of real gas could affect the performance of the Wells turbine and the process of final extraction from the power take–off system. A real gas model would allow designers to include the effect of air moisture when calculating turbine performance. The thesis will show that the ideal gas law should be replaced by a real gas thermal equation of state, leading to new expressions for the adiabatic law, the correction of air density and the influence of water vapour.

At the time of writing, several pilot plants have been tested at different sites around the world with expected power as follows (see The Carbon Trust (2005)): Pico (Azores, $400\,kW$), Limpet (Islay Island, $500\,kW$), Port Kembla (Australia, $300\,kW$), Trivandrum (India, $150\,kW$), and Sakata (Japan, $60\,kW$). Calculations for these plants have been based on a classical ideal gas formulation, which means the predictions are likely to be inaccurate compared to the actual performance, in most cases overestimating power outputs. Therefore, a more reliable theoretical model should be used for the design and operation of those devices.

New devices are likely to be designed and tested for offshore performance in regions of relatively calm wave activity such as off the Mediterranean coast, with the intention of expanding the power extraction network. At such locations, where moderate marine climate conditions occur, a more accurate way to estimate OWC performance is required. Previous work has revealed that the application of a real gas model to simulate the behaviour of a physical model of an OWC chamber demonstrated that significant discrepancies occur between predicted and measured values of turbine performance, in terms of flow rate, moisture and temperature (as can be seen in Chapter 2). Evidence of turbine efficiency reduction provided by the previous experimental tests would suggest that noticeable reductions would occur in the estimated power of full–scale OWC plants. Research needs to be focused on the development of a full real gas model for an OWC device, which can be generalized to any other kind of power take–off turbine.

Therefore, **the aim of this thesis is to develop and validate a new formulation that includes humidity effects in order to estimate accurately the performance of an OWC under actual working conditions**.

1.3.1 Objectives

The main research objectives are as follows:

- To devise a mathematical formulation for the polytropic process of a real gas that describes the adiabatic compression-expansion cycle of the dry air–water vapour mixture in an OWC wave energy converter. The real gas formulation allows us to determine the deviation in PTO efficiency from the expected value under an ideal gas assumption. In order to check the reliability of the formulation, experimental data from wind tunnel testing of an OWC chamber will be used to verify the values of state variables calculated using the deduced process equation.

- To insert the real gas formulation into the classic OWC formulation of Martins–Rivas & Mei (2009–I). The theoretical model will be coupled with the radiation–diffraction formulation to analyse the discrepancies between real gas and ideal gas behaviour, and their effect on OWC performance and efficiency.

- To study the performance of an offshore OWC converter in a 2D numerical flume, accounting for the implementation of the linear response of the PTO system (*i.e.* a Wells turbine). The proposed model represents an idealisation whereby the main features of the wave–device interaction can be visualized without loss of generality. Regarding the turbine performance simulation, the numerical model is adjusted using experimental data from a laboratory study of a Wells turbine. The proposed methodology provides a basis for investigating the OWC performance under average wave conditions in relatively calm coastal waters. Such conditions are likely to occur at potential deployment locations for off–shore wave energy converters in intermediate to shallow–water areas, such as off the Mediterranean and Atlantic coastlines of Southern Spain.

- To test the OWC 2D numerical model with humid air and compare results with those corresponding from dry air model. The comparison will focus on pressure, air flow, and power estimates.

- To compare the proposed real gas model for OWC with data from numerical

results. The accuracy of the theory will be checked against the numerical tests with humid air.

1.4 Synopsis

This thesis comprises four main chapters, as follows. Chapter 2 describes preliminary work using a physical model of an OWC chamber. A summary is given of the laboratory tests undertaken, and the main findings and consequent milestones for the real gas model are discussed. Chapter 3 presents a derivation of the real gas model for OWC performance. Chapter 4 outlines the development of a 2D numerical model to simulate OWC performance with the commercial package ANSYS Fluent®, and discusses wave generation and numerical model validation tests. Two case studies are presented. Chapter 5 presents the results, in particular the coupling between the real gas model and the wave–structure interaction theory. Moreover, a comparison between the real gas theoretical model and the numerical model is described. Humidity is inserted in the numerical model in order to check the accuracy of the theoretical model proposed in this thesis. Chapter 6 summarises the main conclusions and suggests ideas for future work.

	Dry air	Humid air
Analytical	AM1	AM2
Numerical	NM1	NM2

Table 1.1: Models used in the thesis.

Table 1.1 summarises the models developed in this thesis. Dry and humid air conditions are analysed using analytical and numerical models. Model AM1 (analytical, dry air) is based on classical OWC theory (*e.g.* Martins–Rivas & Mei (2009–I)). Model AM2 (analytical, humid air) is the new model developed in this thesis for real gas conditions. The theoretical development is described in Chapter 3, and the application to an OWC chamber is presented in Chapter 5. Model NM1 (numerical model, dry air conditions) is established in Chapter 4 together with the definition of the Actuator Disk Model theory to simulate the Wells turbine. Finally, model NM2 (numerical model, humid air conditions) is

tested in Chapter 5, and compared with NM1. Please note that NM2 models an ideal gas with the same properties as the real gas developed in AM2.

1.5 Published papers

Papers related to the contents of this thesis are summarised below. These have been published in indexed journals, and presented in international conferences.

The following paper was published before the start of this thesis and contains the main research on the physical model treated later in Chapter 2:

- Medina-Lopez *et al.* (2016). **Medina-Lopez E.**, Moñino A., Clavero M., Del Pino C. & Losada M. A. Note on a Real Gas Model for OWC Performance. *Renewable Energy*, Vol. 85, pp. 588–597.

The next papers have been published during the development of this thesis:

- Medina-Lopez *et al.* (2017). **Medina-Lopez E.**, Moñino A., Borthwick A.G.L. & Clavero M. Thermodynamics of an OWC containing real gas. *Energy*, Vol. 135, pp. 709–717. Contains the theoretical development presented in Chapter 3.
- Medina-Lopez *et al.* (2017). **Medina-Lopez E.**, Bergillos R.J., Moñino A., Clavero M. & Ortega-Sanchez M. Effects of Seabed Morphology on Oscillating Water Column Wave Energy Converters. *Energy*, Vol. 135, pp. 659–673. Contains an application of the numerical model presented in Chapter 4, corresponding to the second case study shown in Section 4.5.

This paper is currently under review:

- Moñino *et al.* (2017). Moñino A., **Medina-Lopez E.**, Clavero M. & Benslimane S. Numerical simulation of a simple OWC problem for turbine performance. *International Journal of Marine Energy*, *Under review.* Contains the basis of the numerical model presented in Chapter 4.

The following publications have been presented in international conferences:

- Damage to the Mutriku OWC breakwater – general lessons. **Medina-Lopez E.**, Allsop W., Dimakopoulos A. & Bruce T. Coasts, Marine Structures & Breakwaters Institution of Civil Engineers (ICE) Conference 2017. Liverpool (UK).

- Experimental study of the Oscillating Water Column technology on a Wells turbine. **Medina-Lopez E.** 19th International Congress on Project Management & Engineering. International Project Management Association (IPMA) 2015. Granada (Spain).

- Conjectures on the failure of the OWC breakwater at Mutriku. **Medina-Lopez E.**, Allsop W., Dimakopoulos A. & Bruce T. Coastal Structures & Solutions to Coastal Disasters Joint Conference (COPRI) 2015. Boston (USA).

- Flow characterisation and numerical modelling of OWC wave energy converters. Dimakopoulos A., Cooker M., **Medina-Lopez E.**, Longo D. & Pinguet R. European Wave and Tidal Energy Conference (EWTEC) 2015. Nantes (France).

Chapter 2

Preliminary work: physical model tests of an OWC chamber

As the starting point for the present thesis, this chapter briefly discusses previous results obtained by the author related to the origins of the theoretical development and the wind tunnel experimental data (used for validation purposes). It should be noted that the work presented in this chapter has been extracted from previous research undertaken by the author in her Master's thesis titled "Experimental study of the Oscillating Water Column technology on a Wells turbine", which was submitted in July 2014 for the award of Master in Environmental Hydraulics, directed by the Universities of Málaga and Granada (Spain). **So, I declare that the results shown in this chapter are previous work, and are not part of the new body of knowledge presented for the award of the PhD. The information provided in this chapter provides the starting point of the remaining thesis.**

Moreover, the results obtained in the Master's thesis have been published in the Elsevier's Journal *Renewable Energy* as "Note on a Real Gas Model for OWC Performance. Renewable Energy, Vol. 85, pp. 588–597.". The information summarised in this chapter has been extracted from Medina-Lopez *et al.* (2016).

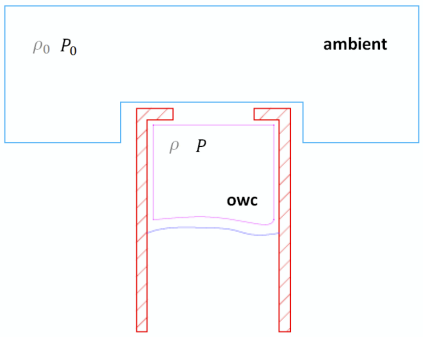

Figure 2.1: Control volume scheme.[Source: Medina-Lopez *et al.* (2016)]

2.1 Fundamentals of air exchange through the turbine in OWC devices

In an OWC system, the turbine operates as the power take off system for pneumatic into electric energy conversion. The primary input for the design of a turbine is pneumatic power based upon the pressure amplitude and the volumetric flow rate at turbine inlet. This section presents the basis of the model for OWC behaviour using the classical ideal gas formulation.

2.1.1 Classical formulation

In the classical formulation, the external thermodynamic pressure in the OWC chamber is assumed constant whereas the pressure inside the chamber is time–dependent. In figure 2.1 the thermodynamic pressures P_0 and P represent the external reference pressure and the total pressure inside the OWC chamber, respectively. The difference between these pressures is the manometric pressure inside the chamber (p):

$$p = P - P_0 \,. \tag{2.1}$$

Following Sarmento *et al.* (1990) & Martins–Rivas & Mei (2009–I), the continuity equation applied to the control volume of air inside the chamber may be written:

$$Q_T^m = -\frac{d}{dt}\left(\rho V\right) = -\left(\rho\frac{dV}{dt} + V\frac{d\rho}{dt}\right) \,, \tag{2.2}$$

where Q_T^m is the mass flow through the turbine, ρ is the air density inside the chamber, V is the air volume inside the chamber, and t is time. It is assumed the

process follows the adiabatic law:

$$pV^{\gamma} = constant\,, \tag{2.3}$$

where γ is the adiabatic gas constant for ideal gas. Equation 2.3 is a particular case of the general equation $pV^n = constant$ for a polytropic system, where n is the polytopic gas index. When $n = \gamma = C_p/C_v$ the polytropic equation becomes the adiabatic law described by equation (2.3). Consequently,

$$\frac{\rho}{\rho_{ref}} = \left(\frac{p}{p_{ref}}\right)^{1/\gamma}\,, \tag{2.4}$$

taking the solution (ρ_0, p_0) as a reference, and the linear relations between pressure and density are established, as in Martins–Rivas & Mei (2009–I) (please note this expression will be modified later in this thesis, following the real gas approach), as:

$$\rho = \rho_0 + \left(\frac{\rho_0}{\gamma p_0}\right) p\,. \tag{2.5}$$

Appendix I provides a complete review of the OWC classical formulation.

2.1.2 Air–water vapour mixture density

The primary characteristics of the air–water vapour mixture are deduced from the properties of the vapour fraction present in dry air. Using the *Clapeyron-Clausius* equation, Stull (2000) (see figure 2.2), the saturation vapour pressure e_s is defined as:

$$e_s = e_0 \cdot exp\left[\frac{L}{R_v}\left(\frac{1}{T_0} - \frac{1}{T}\right)\right]\,, \tag{2.6}$$

where $e_0 = 0.611\,\mathrm{kPa}$ is the partial saturation pressure at temperature $T_0 = 273\,\mathrm{K}$; T is temperature (K); L is the latent vaporization heat; $R_v = 461\,\mathrm{J/K \cdot kg}$ is the water vapour constant, and $L/R_v = 5423\,\mathrm{K}$. The saturation pressure represents the equilibrium state at which no more vapour is present in dry air without further condensation, and depends solely on temperature.

However, the vapour pressure at any temperature (any non–equilibrium state) can be fixed from a given value of relative humidity RH, expressed as the vapour concentration in dry air with reference to the vapour concentration at equilibrium:

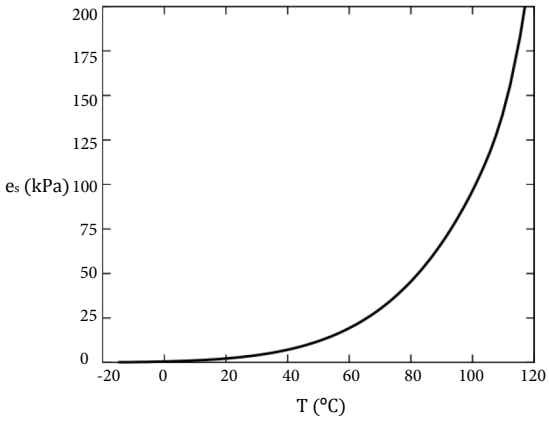

Figure 2.2: Clapeyron-Clausius relation between saturated vapour pressure and air temperature. [Source: Medina-Lopez *et al.* (2016)]

$$RH = \frac{e}{e_s}\,. \tag{2.7}$$

The density of vapour in the air–water vapour mixture, which is known as absolute humidity is given by:

$$r = \frac{m_v}{m_a} = \frac{\varepsilon e}{p - e}, \tag{2.8}$$

where: m_v is the mass of vapour, m_a is the mass of dry air, $\varepsilon = R_a/R_v = 286.7/461 = 0.622$ is the ratio of gas constants for dry air and water vapour respectively, and p is the pressure of the air–water vapour mixture. To deduce the second equality in equation (2.8) it must be kept in mind that the pressure of the mixture is the sum of the partial pressures of dry air p_a and water vapour e:

$$p = p_a + e\,, \tag{2.9}$$

and the ideal gas equation is applied for both dry air and vapour.

The density of the gas consisting of moist air, ρ_g, can be expressed as the ratio of dry air and vapour masses to the total volume V_g of the gas mixture:

$$\rho_g = \frac{m_a + m_v}{V_g}, \tag{2.10}$$

where the state equations for the partial pressures of dry air and water vapour

are:

$$p_a = \frac{m_a}{V_g} R_a T \,, \tag{2.11}$$

and:

$$e = \frac{m_v}{V_g} R_v T \,, \tag{2.12}$$

accounting for the fact that dry air and water vapour occupy the same volume V_g in the mixture. It should be noted from the previous expressions that neither $p_a/R_a \cdot T$ or $e/R_v \cdot T$ are the densities of dry air and water vapour at the pressure p_g of the mixture.

From equations (2.8) and (2.10):

$$\rho_g = \frac{m_a(1+r)}{V_g}. \tag{2.13}$$

On the other hand, from equations (2.11) and (2.12):

$$\begin{aligned} \frac{m_a}{V_g} = \frac{p_a}{R_a T} = \frac{p_g - e}{R_a T} &= \frac{p_g}{R_a T} - \frac{1}{R_a T}\frac{m_v R_v T}{V_g} \\ &= \frac{p_g}{R_a T} - \frac{1}{R_a T}\frac{r m_a R_v T}{V_g}. \end{aligned} \tag{2.14}$$

Cancelling m_a/V_g from both sides and recalling that $\rho_a = p_g/R_a \cdot T$ is the density of dry air at mixture pressure p_g:

$$\frac{m_a}{V_g} = \frac{\rho_a}{1 + r/\varepsilon}. \tag{2.15}$$

The density of air–water vapour mixture finally reads from equations (2.13) and (2.15):

$$\rho_g = \rho_a \frac{1+r}{1+r/\varepsilon} = \rho_a \frac{1+r}{1+1.608r}. \tag{2.16}$$

It is clear from equation 2.16 that the density of moist air is lower than the density of dry air, the degree of discrepancy depending on the humidity through the mixing ratio. Therefore, the conditions of turbine performance can be corrected by means of the water vapour content in dry air. Lower flow density affects the

performance of the turbine, as a less dense air yields a lower drag force on the blades and lower power generated by the turbine.

2.1.3 Equation of state for the real gas

Consider the equation of state for N moles of an ideal gas:

$$pV = NR_0T\,, \tag{2.17}$$

where R_0 is the universal gas constant. Real gas is expected to deviate from ideal, and so equation 2.17 is not satisfied for all p and T. To deal with real gas, we start by defining the compressibility factor per gas mole, $\mathbb{Z}$, Prausnitz (1999), as:

$$\mathbb{Z} = \frac{pv}{R_0T}\,, \tag{2.18}$$

Noting that $v = V/N$. For an ideal gas, $\mathbb{Z} = 1$. A modification to the equation of state is carried out using the *Kammerling–Ones equation* (also known as the *Virial Expansion*) Prausnitz (1999):

$$\mathbb{Z} = \frac{pv}{R_0T} = 1 + \frac{B}{v} + \frac{C}{v^2} + \dots\,, \tag{2.19}$$

where the coefficients B and C depend solely on the temperature (using experimental data).

Hence, an equation of state for a real gas is derived using $\mathbb{Z}$ defined in equation (2.19), Yang & Su (2004), Tsonopoulos & Heidman (1990) as follows:

$$p = \mathbb{Z}\rho_g R_g T\,, \tag{2.20}$$

where ρ_g and R_g are the real gas density and gas constant, determined from equation (2.10). Therefore the compressibility factor $\mathbb{Z}$ is expressed by equation (2.19) using the alternative form proposed by Tsonopoulos & Heidman (1990), with truncated series up to the coefficient B' ($B' = B/M$, where M is molar weight):

$$\mathbb{Z} = 1 + \frac{B'p_c}{R_gT_c}\frac{p_r}{T_r}\,. \tag{2.21}$$

In the previous expression p_c and T_c are the critical values of pressure and temperature for a given gas. Critical temperature and its corresponding pressure

value represent the state beyond which a gas cannot be liquefied by compression, and they are standard reference values used for calculations with reduced state variables T_r and p_r, so that $T_r = T/T_c$ and $p_r = p/p_c$. In the case of water, $T_c = 647\,\mathrm{K}$ and $p_c = 218\,\mathrm{atm} = 220.89 \cdot 10^5\,\mathrm{Pa}$ (air and water vapour properties are summarised in Appendix II). The advantage of the previous formulation is that equation (2.21) can therefore be calculated from, Tsonopoulos & Heidman (1990):

$$\frac{B' p_c}{R_g T_c} = f_0 + \omega f_1 + \chi_{mol} f_2\,, \tag{2.22}$$

where: f_0, f_1 and f_2 are temperature correlation functions; ω is the acentric factor; χ_{mol} is the molar fraction of vapour in dry air. In the case of the air-water vapour mixture (the real gas):

$$\begin{cases} \omega \simeq & 0 \\ f_0 = & 0.145 - \dfrac{0.33}{T_r} - \dfrac{0.1385}{T_r^2} - \dfrac{0.0121}{T_r^3} - \dfrac{0.000607}{T_r^8} \\ f_2 = & \dfrac{0.0297}{T_r^6} - \dfrac{0.0229}{T_r^8}\,. \end{cases} \tag{2.23}$$

From the virial terms and compressibility factor, it is straightforward to calculate the specific heat, $C_{p\,g}$, and the enthalpy, H_g, for the real gas as deviations from the ideal gas values (C_p^*, H^*), Yang & Su (2004):

$$C_{p\,g} = C_p^* + \delta C_p^* p\,, \tag{2.24}$$

and:

$$H_g = H^* + \delta H^* p\,, \tag{2.25}$$

where the deviations of specific heat and enthalpy from ideal gas values are:

$$\delta C_p^* = -\frac{R_g T_c}{p_c} \frac{d^2}{dT_r^2} \left(f_0 + \chi_{mol} f_2\right)\,, \tag{2.26}$$

and:

$$\delta H^* = \frac{R_g T_c}{p_c} \left[\left(f_0 + \chi_{mol} f_2\right) - T_r \frac{d}{dT_r} \left(f_0 + \chi_{mol} f_2\right) \right]\,. \tag{2.27}$$

2.1.4 Calculation of thermodynamic variables

Once the corrected expressions of specific heat and enthalpy have been deduced, the conservation of enthalpy can be applied to a thermodynamic process in a real gas, *i.e.* the air flow through the turbine in an OWC system. Making use of equations (2.24) to (2.27) adopting a similar procedure to Yang & Su (2004), conservations of enthalpy and flow are applied between turbine inlet and outlet, with known values of local temperature T_{in}, pressure p_{in}, and humidity at the inlet. Enthalpy for the ideal gas is expressed as:

$$H^* = C_p T + \frac{1}{2} U^2 \,, \tag{2.28}$$

where the velocity at the turbine outlet, U_{out}, is computed from equations (2.25) and (2.28) for the real gas as:

$$U_{out} = \sqrt{2(H_g - C_p T_{out} - \delta H^* p_{out})} \,, \tag{2.29}$$

Here the temperature T_{out} should not be evaluated through the adiabatic process equation $T^{ad}_{out} = T_{in}(p_{out}/p_{in})^{(\gamma - 1/\gamma)}$ because strictly speaking this last expression is only valid for ideal gas. Instead of using this last equation, a new value of $T_{out} \neq T^{ad}_{out}$ is guessed until the continuity equation between turbine inlet and outlet is satisfied:

$$\rho_g U S|_{in} = \rho_g U S|_{out} \,. \tag{2.30}$$

The iterative procedure, in which the effect of moisture is implemented through the modified air density, produces new pressure and temperature values for the real gas, required to match the continuity condition. Following the proposed methodology, discrepancies between the ideal gas and the real gas model can be computed and corrections from standard predictions can be applied.

2.2 Experimental set up

The turbine performance was tested for a total of three different environmental conditions: so called “dry air” (non forced humidity, environmental conditions, $\approx$ 35% relative humidity), humid air with minimum humidity (50% relative humidity), and humid air with maximum humidity (70% relative humidity).

The wind tunnel comprised a poly-methylmethacrylate (*PMMA*) structure with a test section of 3 m length and 360 mm× 430 mm cross-section, see figure 2.3. Wind speed, up to 20 m/s, was controlled by a variable frequency converter connected to an electric fan at the downstream end of the tunnel, which has a maximum power of 2.2 kW.

The test turbine was mounted in a nylon—cast chamber representing a simplified OWC structure, as shown in figure 2.5b. The turbine was of diameter $D = 0.03\,\mathrm{m}$, cross–sectional area of $3.5906 \cdot 10^{-4}\,m^2$ (centre to blade tip), and turbine blade area $2.4271 \cdot 10^{-4}\,m^2$. Turbine solidity was $\sigma = 0.82$, following Raghunathan (1995) (Appendix III provides a complete description of the turbine performance coefficients and the turbine geometry specifications).

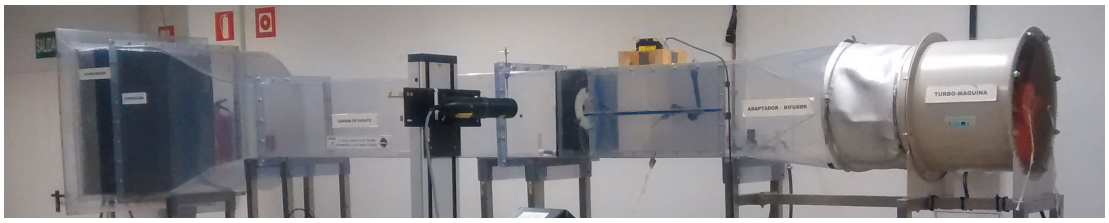

Figure 2.3: Wind Tunnel. [Source: Medina-Lopez *et al.* (2016)]

Turbine calibration tests reveal a linear response between pressure drop and flow discharge (see figure 2.4).

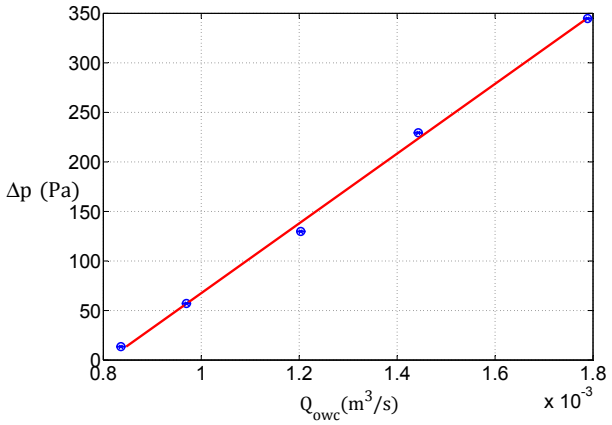

Figure 2.4: Air flow and pressure drop in turbine. Dry tests. [Source: Medina-Lopez *et al.* (2016)]

The pressure distribution was observed using pressure taps (up to 64 channels) connected to a scanner working at a sampling period of 0.0016 s. The accuracy of the pressure system was 0.1% of the measurements. The uncertainty of the measurements was negligible, as depicted in figure 2.4. Six pressure taps were located around the turbine: two of them in the flow direction to measure total pressure, and the remaining four taps sampling perpendicular to the flow direction, for the static pressure measurement. Two static pressure taps and two total pressure taps were placed upstream of the turbine, and two static pressure taps were placed downstream.

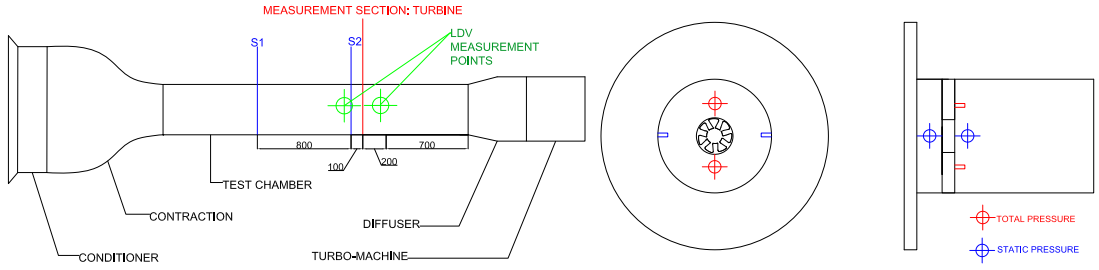

(a) Final set up.

(b) Pressure taps distribution in the measurement section.

Figure 2.5: Schematic showing final set–up scheme and pressure taps. [Source: Medina-Lopez *et al.* (2016)]

Air velocity was measured upstream and downstream of the turbine by a *Laser Doppler Velocimeter (LDV)*, with water particles sprayed in the air flow as seeding. It should be noted that water drops as seeding particles in air could have caused a problem: given that larger water drops move with a strong delay and generate vertical velocity components, whereas smaller water particles tend to evaporate, Longo & Losada (2012). However, several researchers have used *LDV* to measure wind speed in a tunnel using water drops as seeding, Longo (2012). By locating the water gun outside the wind tunnel with the nozzle pointing toward the honeycomb section, it was possible that large water drops were captured by the honeycomb section (following Longo (2012)). To confirm the correct measurement by the *LDV*, an alternative check measurement was undertaken using a *Prandtl Tube*.

Humidity and temperature were measured by remote sensors located at representative sections *S1* and *S2* upstream of the turbine, shown in figure 2.5a; the

first sensor was placed near the entrance to control the input humidity. In addition, an external sensor was used to measure the external reference temperature and humidity. Tests were conducted under constant external humidity conditions. Figure 2.5a shows the final set up, the thermo-hygrometer sensors and the LDV measurement points.

2.3 Results

Experimental results are now presented alongside the theoretical calculations according to the dry air–water vapour mixture methodology, discussed in previously.

2.3.1 Pressure drop and air flow

Figure 2.6 plots the measured pressure drop as a function of flow discharge for different humidity values. For dry air, the turbine response is linear according to calibration. As the humidity increases, the pressure drop diminishes and changes its functional dependence at a given discharge. The pressure drop reduces to 40 % of the dry power value at an air flow of about $2\,m^3/s$ at maximum humidity. From the perspective of turbine performance and efficiency, as moisture increases, greater air flow values are required to preserve a given pressure drop.

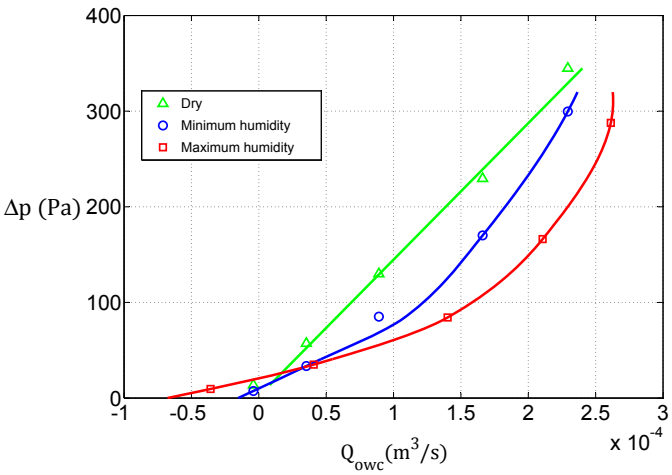

Figure 2.6: Pressure drop as a function of air flow in turbine. All tests. [Source: Medina-Lopez *et al.* (2016)]

In order to account for the humidity content in the three test cases, the non-dimensional pressure is calculated as:

$$p^* = \frac{p}{\rho w^2} \left(\frac{1 - RH}{RH} \right) , \tag{2.31}$$

while the non-dimensional flow discharge is computed as $\Phi = V_x/U$, see Appendix III.

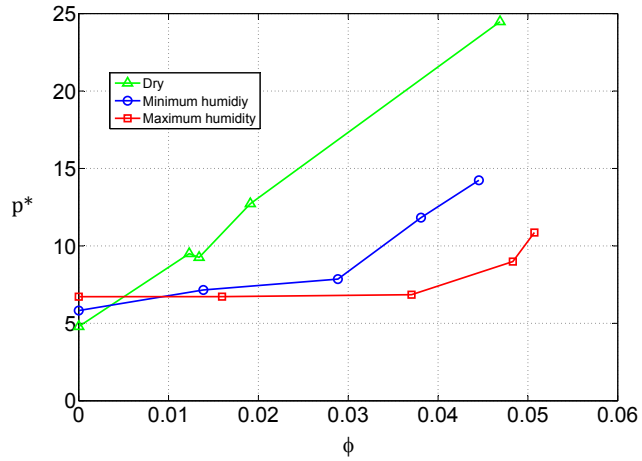

Figure 2.7: Non-dimensional pressure drop and air flow in turbine. All tests. [Source: Medina-Lopez *et al.* (2016)]

Figure 2.7 presents the results in a generalized form as non–dimensional pressure drop (using (2.31)) against non–dimensional flow discharge. It can be observed in figure 2.7 that non-dimensional pressure drop can be reduced by up to 30 % with respect to the dry air case for the highest moisture case.

2.3.2 Density correction by the air–vapour mixture

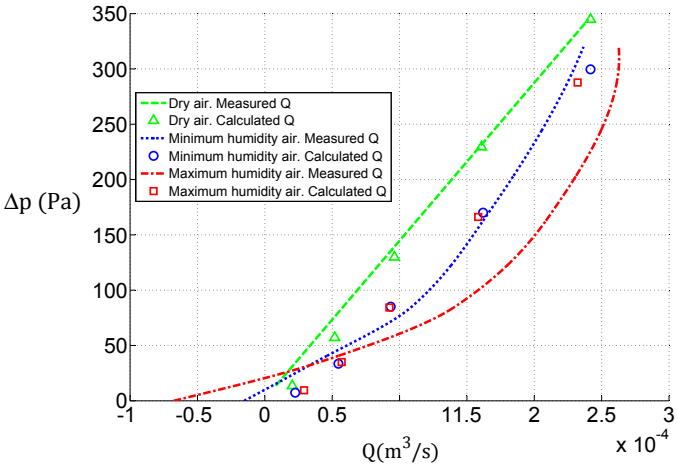

Figure 2.8: Pressure drop as a function of air flow. New humidity curves. Corrected density. $K = 0.014$. [Source: Medina-Lopez *et al.* (2016)]

A first attempt to predict the turbine response under moist air condition was accomplished by substituting the moist air densities calculated by equation (2.16) into the conventional continuity equation (2.2). Although the values provided by the conventional formulation agree reasonably well with the observed values for dry air, there is no good match for the turbine response under moist conditions, as shown in figure 2.8. In short, the classical continuity expression fails to predict accurately the turbine performance when humid air is present, even if the actual turbine also has a linear response in dry air.

2.3.3 Temperature calculations for the real gas model and compressibility factor $\mathbb{Z}$

Using the methodology proposed in previous sections, values of temperature at the turbine outlet are predicted based on the experimental turbine inlet data. Temperature values are calculated from observation of mass flow and application of conservation of enthalpy. Discrepancies can be seen in figure 2.9 with respect to the calculated values under the assumption of adiabatic process for an ideal gas.

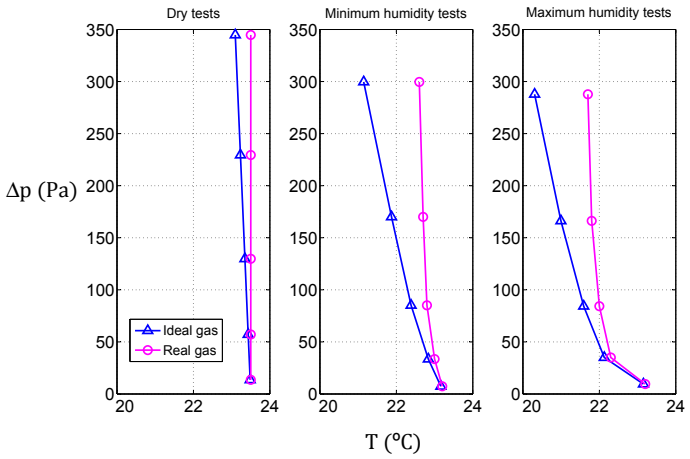

Figure 2.9: Pressure drop versus temperature. All tests. Different temperature calculations. [Source: Medina-Lopez *et al.* (2016)]

The curves present similar behaviour in all cases. For the dry case, the real gas model predicts a fairly constant value of temperature over the complete range of pressure considered, in close agreement with the corresponding values obtained using the ideal gas formulation. However, significant discrepancies are evident between the predicted temperatures obtained using the ideal gas and the real gas methodology. From the results, it is clear that for the continuity flow condition and conservation of enthalpy to be satisfied in the humid air cases, the temperature value must be up to 1 °C above the corresponding ideal gas estimate. In terms of the real gas, the differences can be explained, noting that the adiabatic law, $pV^{\gamma} = constant$, is suitable for an ideal gas. In a real gas, $p = ZvRT$ which means that vRT is not always followed exactly. Then the adiabatic law in its standard form might not be fully applicable, as discussed by Medina-Lopez *et al.* (2016).

The compressibility factor $\mathbb{Z}$ is calculated from equation (2.21) and plotted in figure 2.10. The compressibility factor gives information about the deviation of the real gas behaviour from the expected ideal response. The behaviour of $\mathbb{Z}$ is linear over the whole range studied, *i.e.* between 22.6 °C and 23.2 °C, with overlapping of minimum and maximum humidity curves. The values do not reach 1 (that value would be equivalent to an ideal gas) as temperature decreases.

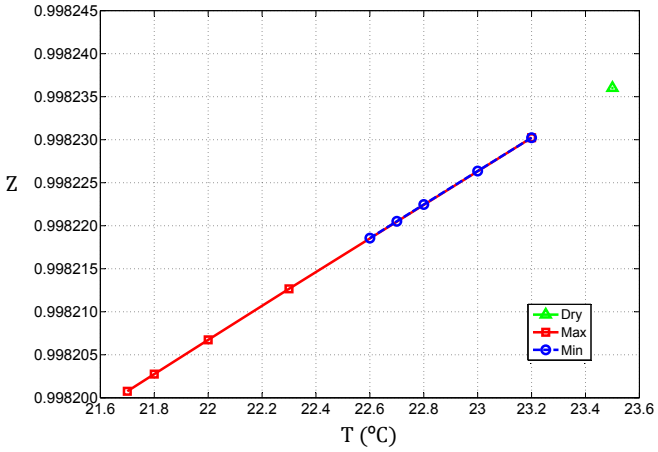

Figure 2.10: Compressibility factor $\mathbb{Z}$. All tests. [Source: Medina-Lopez *et al.* (2016)]

As temperature decreases, the gas behaviour differs from ideal. This is consistent with previous findings that humidity makes the air–water vapour mixture different from an ideal gas.

2.3.4 Power input

Non-dimensional power input calculated from non-dimensional values of pressure drop and flow discharge, following equation (2.32). Results are plotted in figure 2.11.

$$P^* = p^* \Phi \,. \tag{2.32}$$

The power input to the turbine can be reduced up to 33 % with respect to the dry air value as moisture increases. The effect of moisture on turbine power input can be further observed when the power input ratio values in the case of the lowest moisture content are plotted against the flow coefficient, as depicted in figure 2.12. Minimum values of the power input ratio ranging from 0.5 to 0.3 are found when RH exceeds 0.55, depending on the flow coefficient. An asymptotic value of 0.4 is reached for $RH \geqslant 0.65$, indicating the moisture has no added effect on turbine performance beyond that point. It must be noted the results correspond to a stationary flow condition for a generic linear turbine (not a Wells type turbine).

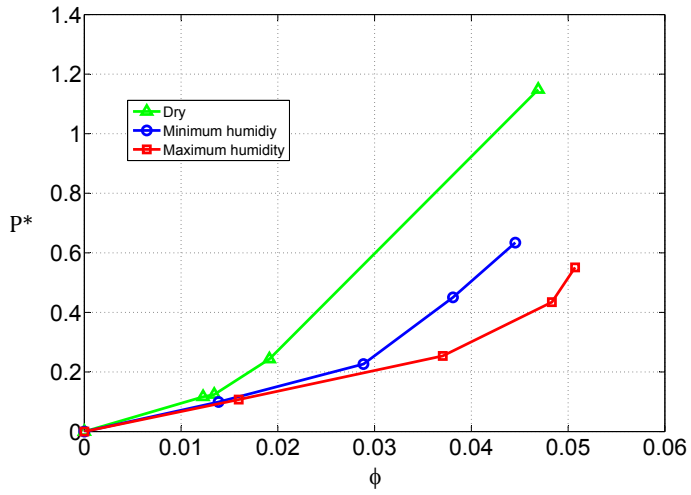

Figure 2.11: Non-dimensional power input as a function of non–dimensional air flow. All tests. [Source: Medina-Lopez *et al.* (2016)]

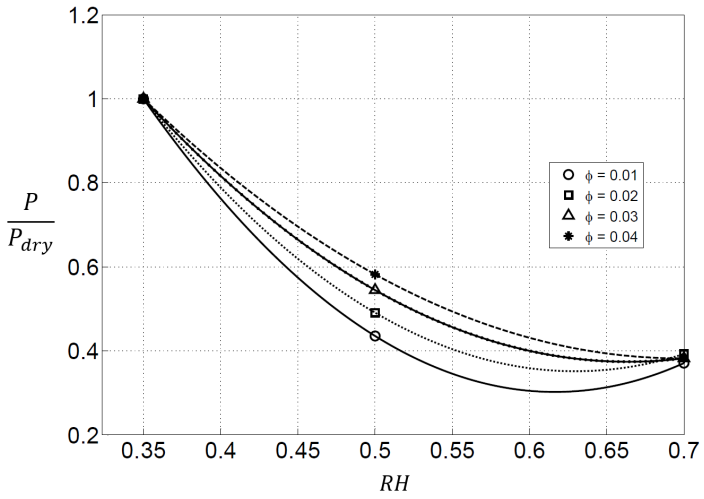

Figure 2.12: Power input ratio as a function of relative humidity. [Source: Medina-Lopez *et al.* (2016)]

2.4 Conclusions

Within the scope of the work presented by Medina-Lopez *et al.* (2016), the reduction in expected power of an OWC due to the presence of moisture in the aircould be significant when applied to the long–term management of an

operational prototype. The greater the moisture content in the standard working conditions of a energy extraction device, the greater the reduction in overall performance. Although the degree of reduction is likely to be design specific, the present results reveal that the effect of moisture on power input and subsequent performance must not be neglected.

This chapter has presented relevant previous experimental measurements obtained by Medina-Lopez *et al.* (2016) on the thermodynamics of a real gas flow through an OWC turbine. Comparisons between experimental measurements and predictions from a real gas model confirmed that significant deviations can occur between predicted and measured turbine performance, the degree of discrepancy depending on flow rate, moisture and temperature.

For a turbine with linear performance in terms of pressure drop and air flow rate under dry air conditions, the experiments reveal that the turbine behaviour under stationary-flow condition deviates from linearity for the air-water vapour mixture.

Following the proposed real gas methodology, it is found that the conservation of air flow rate and enthalpy means that the temperature variation between turbine inlet and outlet does not follow the standard adiabatic law for ideal gas. In fact, the compressibility factor is not exactly unity, which means the real gas differs slightly from the ideal model. The state equation for the real gas differs from that of the ideal gas, and therefore the predicted real gas behaviour deviates from the ideal adiabatic description of the process.

The power input, understood as the available power for the turbine, decreases when moisture increases, exhibiting an asymptotic response as moisture content exceeds 65%.

Chapter 3

Analytical model

This chapter presents the thermodynamic theory of the behaviour of an Oscillating Water Column device. Of particular note is the original theoretical development of the real gas model (model **AM2**, see table 1.1).

3.1 Basic thermodynamic principles and formalism

The basic principles underlying the thermodynamic formulation are set out as follows.

3.1.1 Basic Thermodynamics. Ideal gas

The ideal gas state equation is given by:

$$pv = R_0 T \tag{3.1}$$

where p is pressure, $v = V/N$ is the volume V per mole unit N, R_0 is the universal gas constant, and T is temperature.

An adiabatic process is represented by:

$$pv^{\gamma} = const. \tag{3.2}$$

where $\gamma = C_p/C_v$ is the adiabatic index for ideal gas. It should be noted that

expression (3.2) for the adiabatic process of an ideal gas applies under the following restrictions:

1. The system under consideration is an ideal gas described by the thermal equation of state:
$$pV = NR_0T\,. \tag{3.3}$$

2. The First Principle of Thermodynamics applies for a thermally isolated system. In other words, the balance between internal energy increase and work exerted on the system is exactly zero, so there is no heat exchange with the ambient system:
$$\Delta U - L = \mathbb{Q} = 0 \tag{3.4}$$
where ΔU is internal energy, L is work, and $\mathbb{Q}$ is heat.

3. Given a process in the system, the work applied on the system takes the form:
$$L = -p\Delta V \tag{3.5}$$
provided the process takes place at constant pressure, is reversible, and there is no mass exchange through the boundaries. The system analysed here is considered as simple (homogeneous and isotropic, without electric charge, chemically inert, and its local properties are not affected by changes in the shape of the system), and closed (mass exchange is not allowed through boundaries, but energy exchange is permitted). If the process is reversible and the system is closed (Biel (1986)):
$$L = -\int_{V_1}^{V_2} p\,dV \tag{3.6}$$
which simplifies to equation (3.5) when $p = constant$.

From Molecular Theory (Landau, Ajiezer & Lifshitz (1988)):

$$\Delta U = \frac{3}{2}NR_0\Delta T = -p\Delta V \tag{3.7}$$

where (3.4) and (3.5) have been incorporated. On the other hand, from the

thermal equation of state:

$$p\Delta V + V\Delta p = NR_0\Delta T\,. \tag{3.8}$$

Eliminating ΔT and substituting in (3.7):

$$\frac{3}{2}(p\Delta V + V\Delta p) = -p\Delta V\,, \tag{3.9}$$

which may be rearranged to give

$$\frac{5}{2}p\Delta V + \frac{3}{2}V\Delta p = 0\,. \tag{3.10}$$

Integrating, and recalling that the adiabatic factor is $\gamma = C_p/C_V = 5/3$, we finally get:

$$pV^\gamma = const. \tag{3.11}$$

3.1.2 Internal energy

The First Principle of Thermodynamics states that the required amount of work applied to an adiabatic thermally isolated system (for example a gas enclosed inside a chamber whose volume can be changed by means of a piston–type mechanism) to change its internal energy U, depends only on the initial and final states but not on the type of work itself. Therefore the internal energy can be defined as a state function whose variation equals the work applied to an adiabatic system:

$$\Delta U = L^{adiab}\,. \tag{3.12}$$

If the system is closed but not isolated (*i.e.* it is allowed to undergo thermal energy exchange but not mass exchange), the internal energy variation not only represents the work on the system, which now is non–adiabatic, but also the exchange of heat $\mathbb{Q}$ with the environment during the process:

$$\Delta U = L + \mathbb{Q}\,, \tag{3.13}$$

where according to (3.6) the applied work, assuming a reversible process, is:

$$L = -\int_{V_1}^{V_2} p\,dV\,. \tag{3.14}$$

Over an infinitesimal step, the change in internal energy can be written:

$$dU = dL + d\mathbb{Q}\,, \tag{3.15}$$

and if that infinitesimal process is reversible, following (3.14), we can write:

$$dU = pdV + d\mathbb{Q}\,. \tag{3.16}$$

The above equations reveal the fundamental difference between process and state. In terms of internal energy, the increment is the same for both the adiabatic process and the non–adiabatic process. But there is an important difference in terms of the processes themselves. When no heat exchange is allowed, the internal energy equals the required work to change the system state. But when there is no thermal isolation, energy is not only required in the form of work to change the internal energy but also in the form of heat. It is obvious that the exchanged heat equals the difference between the adiabatic work and non–adiabatic work:

$$\mathbb{Q} = L^{adiab} - L\,. \tag{3.17}$$

An alternative interpretation of (3.12), (3.13) and (3.17) is as follows. The required work to change the system state is greater if the process is adiabatic than if it is not. The latter requires less energy in the form of work, but additional energy in the form of heat (the amount of which can also be determined by the nature of the non–adiabatic work). In any case, the internal energy only depends on the initial and final states, but not on the process itself.

3.1.3 Entropy

Once the concept of heat has been introduced (representing the additional energy required for a closed system to change its internal energy), it is possible to obtain an analytical definition of entropy. Formally, entropy could be interpreted as a measure of the stability of an equilibrium state. This in turn is a measure of the reversibility of a process, Landau, Ajiezer & Lifshitz (1988).

Starting from the differential heat in (3.16), entropy is defined as a state function

whose variation between two states of any system is:

$$S_2 - S_1 \geqslant \int_1^2 \frac{d\mathbb{Q}}{T}, \tag{3.18}$$

where the equality relates solely to a reversible process. The change in entropy in a simple closed system is:

$$\Delta S \geqslant \int \frac{d\mathbb{Q}}{T}. \tag{3.19}$$

For a reversible process,

$$\Delta S_{rev} = \int \frac{d\mathbb{Q}}{T}. \tag{3.20}$$

For an adiabatic process, $d\mathbb{Q} = 0$ at any infinitesimal step, and so:

$$\Delta S_{rev}^{adiab} = 0\,. \tag{3.21}$$

Hence,

$$\Delta S^{adiab} \geq \Delta S_{rev}^{adiab} = 0\,. \tag{3.22}$$

The concepts of entropy and reversibility have a straightforward relationship. Moreover, the change in entropy is a measure of the probability of a system in a future state returning to its previous state, Landau, Ajiezer & Lifshitz (1988). Hence, in a reversible process of a thermally isolated system there is no change in entropy, which implies that both initial and final states are equally probable.

Consider a gas enclosed inside a piston chamber. Although we can increase the internal energy of the gas by compressing it infinitesimally by the piston work, some heat will be transferred to the medium as friction. If we release the piston gradually, the system can be infinitesimally expanded to its initial state, but the medium will not restore the heat lost by friction to the system; in fact, additional heat will again be lost by friction. While the system has returned to its original state in terms of volume and pressure, the medium has changed its internal energy through the exchanged heat (if any). Hence, the medium has not returned to its initial state and the process (*i.e.* the change in system and medium) is not reversible.

From a qualitative standpoint, once the final state is reached the initial state is less likely to be reached again, which means that the variation in entropy takes

a positive value. Conversely, if the piston process is adiabatic no heat exchange will occur. The medium will not change its state and the system could eventually revert to its initial state in terms of internal energy. Any state (considering system and medium) would be equally probable and the entropy in such a process would not be expected to change.

3.1.4 The fundamental equation

Following the previous discussion, the fundamental equation of Thermodynamics for a simple closed system states that the system entropy, S, is an extensive state function depending on the state parameters of internal energy U, system volume V and mole number N:

$$S = S(U, V, N)\,, \tag{3.23}$$

or in the case of unitary variables (per mole unit):

$$s = s(u, v)\,. \tag{3.24}$$

The fundamental equation of Thermodynamics (3.23) can also be expressed in terms of internal energy as

$$U = U(S, V, N)\,. \tag{3.25}$$

In the case of a constant mole number N, equation (3.25) leads to the fundamental differential equation for a simple closed system:

$$dU = TdS - pdV\,, \tag{3.26}$$

which can also be deduced from the differential form (3.16) of the First Principle for a reversible process, when the definition (3.18) of entropy is applied. Several important identifications between fundamental thermodynamic parameters can be deduced from (3.23). In differential form:

$$dS = \left(\frac{\partial S}{\partial U}\right)_{V,N} dU + \left(\frac{\partial S}{\partial V}\right)_{U,N} dV + \left(\frac{\partial S}{\partial N}\right)_{U,V} dN\,, \tag{3.27}$$

and eliminating dS from (3.26) (for a closed system, $N = const$),

$$dS = \frac{1}{T}dU + \frac{p}{T}dV\,. \tag{3.28}$$

Comparing (3.28) with (3.27), the following identities and definitions involving temperature T, pressure p, and chemical potential μ must hold, Biel (1986):

$$\begin{aligned} \frac{1}{T} &= \left(\frac{\partial S}{\partial U}\right)_{V,N}\,, \\ \frac{p}{T} &= \left(\frac{\partial S}{\partial V}\right)_{U,N}\,, \\ \frac{\mu}{T} &= -\left(\frac{\partial S}{\partial N}\right)_{U,V}\,. \end{aligned} \tag{3.29}$$

Finally, the differential form of the fundamental equation (3.25) related to internal energy can be deduced from (3.27):

$$dU = TdS - pdV + \mu dN\,, \tag{3.30}$$

which corresponds to the fundamental differential equation (3.26) applied to a system with $N \neq const$.

Now that entropy has been introduced, the specific heats at constant pressure and volume can be expressed in terms of partial derivatives of entropy, in turn accounting for the heat exchange in the system, as follows:

$$\begin{aligned} C_p &= \frac{T}{N}\left(\frac{\partial S}{\partial T}\right)_{p,N}\,, \\ C_V &= \frac{T}{N}\left(\frac{\partial S}{\partial T}\right)_{V,N}\,. \end{aligned} \tag{3.31}$$

Moreover, if we consider an ideal gas, the application of Molecular Theory reveals that C_p can be described by, Biel (1986):

$$C_p \simeq A + BT + CT^2\,, \tag{3.32}$$

for $300\,K \leqslant T \leqslant 2000K$, where:

$$A \simeq 6cal/mol \cdot K; B \simeq 10^{-3}cal/mol \cdot K^2; C \simeq 10^{-6}cal/mol \cdot K^{-3}\,. \tag{3.33}$$

Given that

$$T \to 0 \;\Rightarrow\; C_p \to C_p^0 \simeq \frac{5}{2}R_0\,, \tag{3.34}$$

the specific heat of the ideal gas becomes

$$C_p = C_p^0 + c(T)\,, \tag{3.35}$$

noting that

$$\lim_{T\to 0} c(T) = 0\,. \tag{3.36}$$

It is clear from (3.23) to (3.25) that a functional connection exists between variables U, S, T, V, p, N and μ. If additional state equations are provided for a system, the independent variables to be used can be replaced by other variables to which they are related. In that sense, the Maxwell relations can be used to link the previous variables to each other through their derivatives, Biel (1986). Hence, the fundamental equation in the form (3.23) can be rewritten in a more convenient way (to be applied later) as:

$$S = S(T, p, N)\,, \tag{3.37}$$

and its differential form in terms of molar quantities:

$$ds = \left(\frac{\partial s}{\partial T}\right)_p dT + \left(\frac{\partial s}{\partial p}\right)_T dp\,. \tag{3.38}$$

From the Maxwell relations in molar quantities, Biel (1986):

$$\left(\frac{\partial s}{\partial p}\right)_T = -\left(\frac{\partial v}{\partial T}\right)_p\,, \tag{3.39}$$

where $v = V/N$ is the specific volume. Using (3.31), the differential form (3.38) can be expressed as:

$$ds = \frac{C_p}{T}dT - \left(\frac{\partial v}{\partial T}\right)_p dp\,. \tag{3.40}$$

3.1.5 Real gas formalism

In certain cases, it is not feasible to determine either the fundamental equation (3.23) for the system or a state equation, (*i.e.* the thermal equation of state (3.1) for a real gas). In such cases the experimental field helps us to infer relations between certain system independent variables, the thermodynamic parameters. For a real gas to be defined, it is necessary to introduce a thermodynamic model such as the ideal gas model or the *Van der Waals* model, to help define intermediate states.

The compressibility factor $\mathbb{Z}$ is defined as

$$\mathbb{Z} = \frac{pv}{R_0 T}, \tag{3.41}$$

where $v = V/N$. The real gas can be described in terms of the Virial expansion (Prausnitz (1999)), given by the Leiden representation:

$$\frac{pv}{R_0 T} \simeq 1 + \frac{B}{v} + \frac{C}{v^2} \cdots , \tag{3.42}$$

or by the Berlin representation:

$$pv \simeq R_0 T + \widehat{B} p + \widehat{C} p^2 \cdots , \tag{3.43}$$

in which:

$$\begin{cases} \widehat{B} = B \\ \widehat{C} = \dfrac{C - B}{R_0 T}. \end{cases} \tag{3.44}$$

The Virial theorem represents a perturbation expansion of statistical mechanics. It provides equations that relate average kinetic energy with average potential energy. The kinetic energy of the system is related to temperature, giving in the case of thermodynamics expressions to define a real gas. Statistical mechanics use probability to define the behaviour of macroscopic system based on the elements the system is composed of, and their interactions, Biel (1986). The second and third virial coefficients B and C are functions of temperature that have to be determined experimentally, and $v = V/N$ is the specific volume. Expressions (3.42) and (3.43) reveal that a real gas does not satisfy the thermal equation of state for an ideal gas, except for those states in which the virial coefficients tend to 0. The

purpose of the real gas model is to provide a basis for the thermodynamic relations between system variables, starting from relations between other independent variables such as (3.42).

To help achieve a better understanding of the above concepts, let us introduce the **modified ideal gas** model, as a first step in the treatment of the real gas. The modified ideal gas is a simple thermodynamic system in which (per mole unit):

$$\begin{cases} pv^m = R_g T\,, \qquad T \geqslant \tilde{T}(p_0) \\ C_p^m = t\left(\dfrac{\partial s^m}{\partial T}\right)_p \;\Rightarrow\; s^m(T,p_0) = \displaystyle\int_0^T \frac{C_p^m(\tau,p_0)}{\tau} d\tau\,, \qquad T \leqslant \tilde{T}(p_0)\,, \end{cases} \tag{3.45}$$

where R_g is the real gas constant, τ is an integration variable, and $\tilde{T}$ is a characteristic temperature depending on pressure p_0. Index m stands for the modified ideal gas and p_0 represents any pressure value. Equation (3.45) states that the modified ideal gas is a system that behaves as an ideal one at temperature greater than the threshold value $\tilde{T}(p_0)$. For temperature lower than $\tilde{T}(p_0)$ the system behaves as a real gas, and the only requirement is that the entropy and specific heat follow the definition for a simple closed system. The entropy of the modified ideal gas for $T = \tilde{T}$ is deduced from (3.45) as:

$$s^m(\tilde{T},p_0) = \int_0^{\tilde{T}} \frac{C_p^m(\tau,p_0)}{\tau} d\tau = s^*(\tilde{T},p_0)\,, \tag{3.46}$$

since for $T = \tilde{T}$, the modified ideal gas behaves as an ideal gas. The superscript * indicates a variable whose value is that of the equivalent ideal gas. Using the state equation for the ideal gas:

$$pv = R_0 T\,, \tag{3.47}$$

and the expression (3.35) for the specific heat, the differential equation (3.40) applied to the ideal gas entropy s^* between any state $0 < T_1 < \tilde{T}$ and $\tilde{T}$ becomes:

$$s^*(\tilde{T},p_0) = s^*(T_1,p_1) + C_p^0 \ln\frac{\tilde{T}}{T_1} + \int_{T_1}^{\tilde{T}} \frac{C(\tau)}{\tau} d\tau - R_0 \frac{p_0}{p_1}\,. \tag{3.48}$$

Substituting in (3.46):

$$s^m(\tilde{T},p_0)=\int_0^{\tilde{T}}\frac{C_p^m(\tau,p_0)}{\tau}d\tau=s^*(T_1,p_1)+C_p^0\ln\frac{\tilde{T}}{T_1}+\int_{T_1}^{\tilde{T}}\frac{C(\tau)}{\tau}d\tau-R_0\frac{p_0}{p_1}. \quad (3.49)$$

Equation (3.49) defines the entropy of the modified ideal gas in terms of the entropy of the ideal gas, and so is a model for which a state function is known. Hence, when the entropy of the real gas is to be defined in terms of the modified ideal gas, all the reference states are defined and the real gas description is consistent with the thermodynamic formalism.

Let us apply now the differential equation (3.40) between two states $T_0 \leqslant \tilde{T} \leqslant T$ (*i.e.* real and ideal behaviour respectively). Taking the expansion (3.43) up to second order:

$$ds=\frac{C_p}{T}dT-\frac{\partial v}{\partial T}dp=\frac{C_p}{T}dT-\left(\frac{R_0}{p}+\frac{dB}{dT}\right)dp\,, \quad (3.50)$$

and integrating:

$$s(T,p)=s(T_0,p_0)+\int_{T_0}^{T}\frac{C_p(\tau,p_0)}{\tau}d\tau-R_0\ln\frac{p}{p_0}-\frac{dB}{dT}(p-p_0)\,. \quad (3.51)$$

Note that the previous expression involves the molar entropy $s(T_0,p_0)$ which remains unknown. To overcome this, we apply the differential equation (3.40) to the modified ideal gas while making use of the state equation of the ideal gas (3.41), and noting that the behaviour is ideal provided $T \geqslant \tilde{T}$. This leads to:

$$s^m(T,p)=s^m(T_0,p_0)+\int_{T_0}^{T}\frac{C_p^m(\tau,p_0)}{\tau}d\tau-R_0\ln\frac{p}{p_0}-\frac{dB}{dT}(p-p_0)\,. \quad (3.52)$$

Subtracting (3.51) and (3.52):

$$s(T,p)=s(T_0,p_0)+s^m(T,p)-s^m(T_0,p_0)+\int_{T_0}^{T}\frac{C_p(\tau,p_0)-C_p^m(\tau,p_0)}{\tau}d\tau-\frac{dB}{dT}(p-p_0)\,. \quad (3.53)$$

As $T_0 \to 0$, then $s(T_0,p_0) \to 0$ and $s^m(T_0,p_0) \to 0$. Hence,

$$s(T,p)=s^m(T,p)+\int_{T_0}^{T}\frac{C_p(\tau,p_0)-C_p^m(\tau,p_0)}{\tau}d\tau-\frac{dB}{dT}(p-p_0)\,. \quad (3.54)$$

For a given real gas with $C_p(\tau, p_0)$, it is always feasible to choose a modified ideal gas such that:

$$\begin{cases} C_p^m(\tau, p_0) = C_p(\tau, p_0) & \tau \leqslant \tilde{T}(p_0) \\ C_p^m(\tau, p_0) = C_p^* = \lim\limits_{p_0 \to 0} C_p(\tau, p_0) & \tau \geqslant \tilde{T}(p_0)\,. \end{cases} \tag{3.55}$$

Here, the gas behaves as real at lower temperatures and as ideal at higher temperatures. Combining (3.55) and (3.54) an expression of the molar entropy for the real gas is obtained as

$$\boxed{s(T,p) = s^*(T,p_0) - \frac{dB}{dT}p} \tag{3.56}$$

Equation (3.56) states that the molar entropy of a real gas equals the entropy of an ideal gas plus a correction accounting for the second virial expansion coefficient. This demonstrates that given a relation between system independent variables such as the virial expansion (3.42), thermodynamic formalism can be applied to obtain a relation between system variables that would otherwise be unknown. Once the molar entropy of a real gas is defined, the other real gas system variables can be deduced.

The specific heat of a real gas is deduced by substituting (3.56) in to (3.31) to give:

$$\boxed{C_p = C_p^* - T\frac{d^2B}{dT^2}p} \tag{3.57}$$

To determine the change in enthalpy of a real gas it is necessary to deduce beforehand the chemical potential. Consider the Gibbs–Duhem equation, Biel (1986):

$$d\mu = -sdT + vdp\,. \tag{3.58}$$

Then, integrating (3.58) for both real and ideal gas:

$$\begin{aligned} \mu(T,p) - \mu(T,p_0) &= \int_{p_0}^{p} v dp\,, \\ \mu^*(T,p) - \mu^*(T,p_0) &= \int_{p_0}^{p} v^* dp\,. \end{aligned} \tag{3.59}$$

Taking the limit $\mu(T,p_0) \to 0$ and $\mu^*(T,p_0) \to 0$ for $p_0 \to 0$, and subtracting both

expressions:

$$\mu(T,p) - \mu^*(T,p_0) = \int_0^p (v - v^*)dp\,. \tag{3.60}$$

Using the virial expansion (3.43) and recalling that $v^* = R_0T/p$, the following expression is obtained for the chemical potential of the real gas:

$$\boxed{\mu(T,p) = \mu^*(T,p) + Bp} \tag{3.61}$$

Finally, from the Euler equation, Biel (1986), the molar enthalpy is defined as:

$$h = Ts + \mu\,, \tag{3.62}$$

and using (3.56) and (3.61), we get:

$$\boxed{h(T,p) = h^*(T,p) + Bp - \frac{dB}{dT}p} \tag{3.63}$$

For C_v the approximation is not straightforward. Instead, the expression for specific heat at constant volume taking into account the First Law of Thermodynamics ($du = Tds - pdv$), may be written as

$$C_v = \left(\frac{\partial u}{\partial T}\right)_v\,. \tag{3.64}$$

Using the differential form of the molar internal energy u, and integrating between two pressure states (p_0 and p), the following expression for the real gas internal energy is obtained:

$$u(T,p) = u^*(T) - T^2\frac{R_0}{v}\frac{dB}{dT}\,. \tag{3.65}$$

Substituting equation (3.65) into equation (3.64) and rearranging, gives

$$\boxed{C_v \approx C_v^* - \frac{R_0}{v}\frac{d}{dT}\left(T^2\frac{dB}{dT}\right)} \tag{3.66}$$

where B is the second virial coefficient, defined by Tsonopoulos & Heidman (1990) as

$$\frac{Bp_c}{R_0T_c} = f_0 + \omega f_1 + \chi_{mol} f_2\,. \tag{3.67}$$

The f coefficients, also called *temperature correlation functions*, are calculated

through the Tsonopoulos-Heidman approximation, (Tsonopoulos & Heidman (1990)), which expresses the coefficients as functions of the reduced temperature of the real gas, T_r, given by:

$$\begin{cases} f_0 = & 0.145 - \dfrac{0.33}{T_r} - \dfrac{0.1385}{T_r^2} - \dfrac{0.0121}{T_r^3} - \dfrac{0.000607}{T_r^8}, \\ f_1 = & 0.0637 + \dfrac{0.331}{T_r^2} - \dfrac{0.423}{T_r^3} - \dfrac{0.008}{T_r^8}, \\ f_2 = & \dfrac{0.0297}{T_r^6} - \dfrac{0.0229}{T_r^8}. \end{cases} \tag{3.68}$$

where ω is the accentric factor, whose value is almost zero ($\omega \simeq 0$) for symmetric molecules such as H_2O. In equation (3.67), χ_{mol} is the molar fraction of water vapour in dry air for a given real gas. The ideal gas values needed to calculate the equivalent real gas values are calculated as, Biel (1986):

$$\Delta s^* = R_0 log\left(\frac{T^{5/2}}{p}\right), \tag{3.69}$$

and

$$C_p^* = 1010 J/K \cdot kg\,, \tag{3.70}$$

for ideal dry air.

$$u^* = \frac{3}{2} R_0 T\,, \tag{3.71}$$

and

$$h^* = u^* + pV\,. \tag{3.72}$$

Equations (3.56), (3.57), (3.61), (3.63), and (3.66) define the thermodynamic variables of a real gas in terms of those of the corresponding ideal gas. Provided a value for the virial coefficient B is supplied, usually from experimental data, then the full thermodynamic description of the real gas can be achieved. In that sense, the equations can be used together with the Tsonopoulos innovation (Tsonopoulos & Heidman (1990)) to develop improved expressions for the thermodynamic variables of the real gas, Yang & Su (2004).

3.1.5.1 Non dimensional thermodynamic parameters for a real gas

The thermodynamic parameters derived before are non–dimensionalized in order to gain a universal perspective of their behaviour under different moisture levels. Using the Π *Buckingham Theorem*, we obtain the following non dimensional numbers:

$$\Delta\tilde{s} = \left|\frac{T^3 R_0}{p^2 B v}\right| \Delta s\,, \tag{3.73}$$

$$\tilde{C_p} = \left|\frac{T}{pB}\right| C_p\,, \tag{3.74}$$

$$\tilde{u} = \left|\frac{T R_0}{p^2 B v}\right| u\,, \tag{3.75}$$

and

$$\tilde{h} = \left|\frac{T R_0}{p^2 B v}\right| h\,. \tag{3.76}$$

Figures 3.1 to 3.4 show the variations in $\Delta\tilde{s}$, $\tilde{C_p}$, $\tilde{u}$ and $\tilde{h}$ with T_r for three different conditions, ideal gas, intermediate conditions ("mid"), and real gas. All variables are expressed per mole unit. The reduced temperature range corresponds to that of the experiments conducted by Medina-Lopez *et al.* (2016).

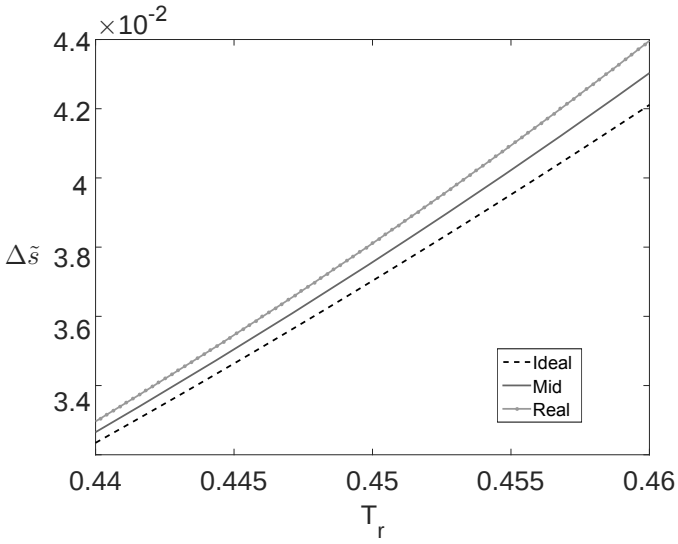

Figure 3.1: Variations of non dimensional entropy with reduced temperature for a real gas.

Figure 3.1 indicates that entropy progressively increases with temperature, due to

an associated increase in heat in the real gas system. Moreover, the real gas is more entropic than the ideal gas, which implies a lower level of energy is available for the real gas. This behaviour is corroborated by comparing the entropy–temperature curve with the enthalpy and internal energy counterparts. Energy for the real gas is lower than for ideal gas. Thus it can be concluded that the real gas is more entropic than the ideal gas, which translates to lower available energy for the real gas. Moreover, figure 3.1 shows that the starting hypothesis of reversible process cannot be applied to the OWC. The process then would be adiabatic irreversible, which gives some hysteresis to the system, in terms of starting and finishing point of the inhalation / exhalation cycles. However, this might be caused by changes in the adiabatic index n: as the cycle starts with an adiabatic process, and is followed by a different adiabatic process (with a different n), the sequence makes the entropy of the overall cycle grow, although each process is reversible.

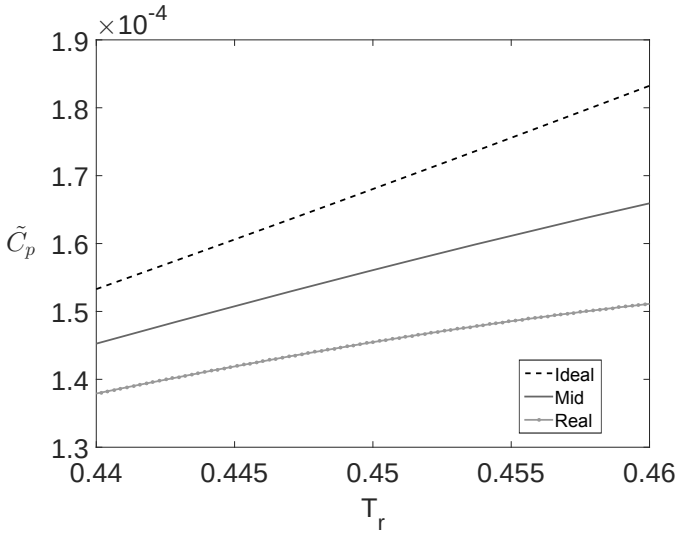

Figure 3.2: Variations of non dimensional specific heat at constant pressure with reduced temperature for a real gas.

Figure 3.2 shows that the non–dimensional specific heat at constant pressure is consistently lower for a real gas. The heat needed to increase the temperature of a real gas by one degree is lower than that for an ideal gas because of intermolecular forces which are only represented by the real gas formulation. In the case of a real gas, when heat is supplied to the system, molecular agitation increases because of repulsive intermolecular forces that promote collisions. This raises the kinetic energy of particles in the system, and so increases the temperature, resulting in

less external energy available to increase the system temperature. This leads to lower specific heat for a real gas than for an ideal gas. If the specific heat at constant pressure for water vapour is considered, then C_p for real gas would be lower, being in–between the dry air value and the water vapour one.

The finding can be further explained by considering a scenario where the ideal gas represents a mix of oxygen and hydrogen, whose specific heats at constant pressure are $0.9J/K \cdot g$ and $14.3J/K \cdot g$ respectively. If there is twice the amount of hydrogen than oxygen, then the specific heat of the mix will be $9.8J/K \cdot g$. So, if an equivalent real gas is composed of a molecule of water vapour (formed by independent hydrogen and oxygen molecules present in the ideal gas), the specific heat for the real gas will now be $2J/K \cdot g$.

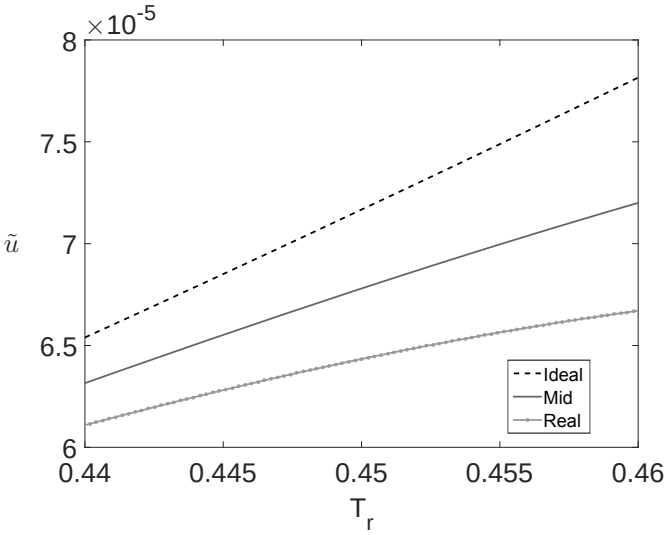

Figure 3.3: Dependence of non dimensional internal energy on reduced temperature for a real gas.

Figure 3.3 shows the variations in internal energy for different humidities in a gas. As in previous figures, internal energy for the real gas is lower than that for the ideal one. Moreover, figure 3.4 presents the dependence of enthalpy for different humidities. The higher the degree of humidity, the lower the enthalpy of the real gas.

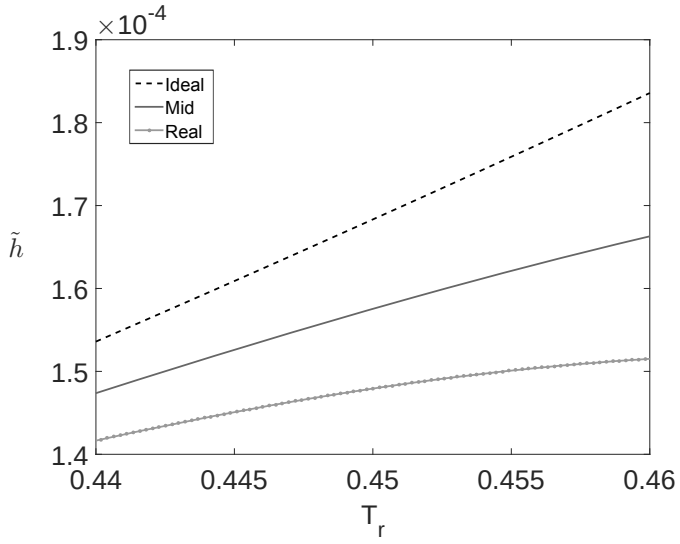

Figure 3.4: Dependence of non dimensional enthalpy on reduced temperature for a real gas.

3.1.5.2 The real gas non dimensional number

A noticeable result is the appearance of a common non–dimensional group, $TR_0 = pB$, in equations (3.73) to (3.76). The group appears as a primary factor in the real gas equation (3.121). In general terms, the group is defined as

$$Rg = -\frac{TR_0}{pB} = \frac{1}{1-\mathbb{Z}}\,. \tag{3.77}$$

Note that Rg takes the following limits depending on the nature of the gas:

$$\begin{cases} Rg \to \infty\,,\ as\,\mathbb{Z} \to 1\,(ideal\,gas)\,, \\ Rg \to 1\,,\ as\,\mathbb{Z} \to 0\,. \end{cases} \tag{3.78}$$

The closer Rg is to 1, the closer the system is to real–gas behaviour. Although the value of $\mathbb{Z} = 0$ is hypothetical and unreal, it provides a useful means by which to obtain a limit that can be used to compare real and ideal gas behaviours. For an example, a mixture of dry air and water vapour with a pressure distribution of $[-100, 100]$kPa, relative humidity between [0% - 100%], and temperature range $[15, 20]^{\circ}$C has values of $\mathbb{Z} \in [0.99 - 0.998]$ and related values of $Rg \in [80 - 500]$.

3.1.5.3 Speed of sound in a real gas

The speed of sound, C_s, appears in analysis of wave energy extraction devices through the relationship between pressure and density, and affects compressibility. The objective now is to obtain a preliminary way of estimating the speed of sound in a real gas. Although the speed of sound is not utilised directly herein, it should be noted that C_s must be modified following any change to n in future calculations related to OWC chambers.

The speed of sound in an ideal gas is similar to wave propagation in an elastic bar, but with a noticeable difference: gases are highly compressible and their density changes with pressure (Wu (1990)). In this context, the one-dimensional wave equation (see *e.g.* Kreyzsig (2006)) is

$$\frac{\partial^2 \Psi}{\partial t^2} = \left(\frac{\partial p}{\partial \rho}\right)_0 \frac{\partial^2 \Psi}{\partial x^2}\,, \tag{3.79}$$

where Ψ represents a displacement from equilibrium position. The term $\left(\frac{\partial p}{\partial \rho}\right)_0$ is the squared velocity term. If the ideal gas equation is applied, then the speed of sound in an ideal gas undergoing an adiabatic process is

$$C_s^{*2} = \left(\frac{\partial p}{\partial \rho}\right)_0 = \frac{n p_0}{\rho_0}\,. \tag{3.80}$$

Instead, if an adiabatic process of a real gas is now considered, equation (3.80) is modified by applying the real gas equation, $p = \rho \mathbb{Z} R_0 T$ to obtain

$$\left(\frac{\partial p}{\partial \rho}\right) = n \mathbb{Z} R_0 T\,. \tag{3.81}$$

Inserting the definition of the adiabatic index for a real gas (equation (3.120)) leads to

$$C_s^2 = \frac{C_p/C_v}{1 - \dfrac{p}{\mathbb{Z}}\left(\dfrac{\partial \mathbb{Z}}{\partial p}\right)_T} \mathbb{Z} R_0 T\,. \tag{3.82}$$

Equation (3.82) depends on the compressibility factor $\mathbb{Z}$, pressure and temperature (which can be determined from experimental measurements), and the specific heats for the real gas. The compressibility factor $\mathbb{Z}$ therefore depends solely on p and T.

Following the same approach taken previously to n, equation (3.82) can be simplified using equations (3.121) to (3.124) to give

$$C_s = \sqrt{\frac{C_p}{C_v}\mathbb{Z}^2 R_0 T}\,. \tag{3.83}$$

3.1.6 Processes of simple closed systems

In a simple system, a process is governed by a relationship between system variables, which describes the states through which the system evolves, Biel (1986). The process equation usually takes the form $x = const$ where x is any state function. The main difference between a state equation and a process equation is that the former describes any system state, while the latter is only suitable for those states attached to the process.

In general, changes in system state functions during a process are related to the energy budget of the system in terms of heat exchange and applied work. A first step in deducing a process equation is to define all variables pertaining to the fundamental equation 3.23. Hence, for a given process in which a certain state parameter y remains constant, the specific heat under constant y can be defined as:

$$C_y = T\left(\frac{\partial s}{\partial T}\right)_y\,, \tag{3.84}$$

and the *index* m as:

$$m = \frac{C_y - C_p}{C_y - C_V}\,. \tag{3.85}$$

A differential equation between state parameters p and V may now be derived. Turning to the fundamental equation (3.37), the differential form of the entropy can be expressed both in terms of (T, p) and (T, v) as:

$$\begin{aligned} ds &= \left(\frac{\partial s}{\partial T}\right)_p dT + \left(\frac{\partial s}{\partial p}\right)_T dp\,, \\ ds &= \left(\frac{\partial s}{\partial T}\right)_v dT + \left(\frac{\partial s}{\partial v}\right)_T dv\,. \end{aligned} \tag{3.86}$$

The change in entropy with respect to temperature in a process under constant

state parameter y is therefore given by:

$$\begin{aligned}\left(\frac{\partial s}{\partial T}\right)_y &= \left(\frac{\partial s}{\partial T}\right)_p + \left(\frac{\partial s}{\partial p}\right)_T \left(\frac{\partial p}{\partial T}\right)_y ,\\ \left(\frac{\partial s}{\partial T}\right)_y &= \left(\frac{\partial s}{\partial T}\right)_v + \left(\frac{\partial s}{\partial v}\right)_T \left(\frac{\partial v}{\partial T}\right)_y .\end{aligned} \tag{3.87}$$

Substituting (3.87) into (3.84) and inserting the result in (3.85), we obtain:

$$m = \frac{T\left(\frac{\partial s}{\partial p}\right)_T \left(\frac{\partial p}{\partial T}\right)_y}{T\left(\frac{\partial s}{\partial v}\right)_T \left(\frac{\partial v}{\partial T}\right)_y} = \left(\frac{\partial v}{\partial p}\right)_T \left(\frac{\partial p}{\partial v}\right)_y . \tag{3.88}$$

Retaining thermodynamic formalism (Biel (1986)), the derivatives of entropy with respect to p and v can be expressed more conveniently in terms of the isobaric expansion coefficient α and the isothermal compressibility coefficient k_T as follows:

$$\begin{aligned}\left(\frac{\partial s}{\partial p}\right)_T &= -\left(\frac{\partial v}{\partial T}\right)_p = -v\alpha ,\\ \left(\frac{\partial s}{\partial v}\right)_T &= \left(\frac{\partial s}{\partial p}\right)_T \left(\frac{\partial p}{\partial v}\right)_T = -\left(\frac{\partial v}{\partial T}\right)_p \left(\frac{\partial p}{\partial v}\right)_T = \frac{\alpha}{k_T},\end{aligned} \tag{3.89}$$

where:

$$\alpha = \frac{1}{V}\left(\frac{\partial V}{\partial T}\right)_{p,N} , \tag{3.90}$$

and:

$$k_T = -\frac{1}{V}\left(\frac{\partial V}{\partial p}\right)_{T,N} . \tag{3.91}$$

Substituting (3.87) into (3.31) and utilising (3.84) and (3.89), the following expressions are obtained:

$$\begin{aligned}C_y - C_p &= -Tv\alpha \left(\frac{\partial p}{\partial T}\right)_y ,\\ C_y - C_p &= \frac{T\alpha}{k_T}\left(\frac{\partial v}{\partial T}\right)_y .\end{aligned} \tag{3.92}$$

Dividing both expressions and using (3.85), a differential equation for the process

may be written as (Gel'man & Smolkin (1966)):

$$\boxed{\left(\frac{\partial p}{\partial v}\right)_y = -\frac{m}{v k_T}} \tag{3.93}$$

Equation (3.93) represents the relationship between state parameters p and v, for a general process in a simple closed system where the system variable y is held constant with no additional restrictions.

In a further step, we define a **polytropic system** as a simple closed system within a polytropic process, such that:

$$pv^n = const.\,, \tag{3.94}$$

where n is the *polytropic index*.

It is shown in (3.94) that the concept of polytropic system is attached to a given process in that system. An index n has to be specified, so that the product pv^n remains constant for any state in a polytropic process —but not other states—. Expressing (3.94) in differential form,

$$v^n dp + nv^{n-1} p dv = 0\,, \tag{3.95}$$

and differentiating v with respect to p for $y = const.$ gives

$$\left(\frac{\partial v}{\partial p}\right)_y = -\frac{v}{np}. \tag{3.96}$$

Comparing the general process equation (3.93) with the differential equation (3.96) for a polytropic system, the expression for the polytropic index may be written:

$$\boxed{n = \frac{m}{p k_T}} \tag{3.97}$$

3.1.7 Processes in ideal gas

The nature of the system hads yet to be specified. If the system consists of an ideal gas in an adiabatic process $y = s$, then $C_y = 0$ according to (3.84), and

$m = C_p/C_V = \gamma$. From (3.97), the polytropic index becomes

$$n = \frac{\gamma}{pk_T}. \tag{3.98}$$

Then,the isothermal compressibility coefficient for an ideal gas is:

$$k_T = -\frac{1}{V}\left(\frac{\partial V}{\partial p}\right)_{T,N} = \frac{1}{p}, \tag{3.99}$$

and $n = \gamma$. Hence, the ideal gas is polytropic in an adiabatic process, and the process equation,

$$pv^{\gamma} = const \tag{3.100}$$

is the same as deduced previously, equation(3.11), using a rationale based on the First Principle and Molecular Theory.

Applying Jacobian formalism to the process equation (3.93),

$$\left(\frac{\partial p}{\partial v}\right)_s = -\frac{m}{vk_T}. \tag{3.101}$$

For extensive variables:

$$\left(\frac{\partial p}{\partial V}\right)_{S,N} = \frac{\partial(p,S,N)}{\partial(V,S,N)} = \frac{\partial(p,S,N)}{\partial(T,p,N)}\frac{\partial(T,p,N)}{\partial(V,S,N)} = \frac{\{p,S,N\}}{\{V,S,N\}} \tag{3.102}$$

where:

$$\{p,S,N\} = \begin{vmatrix} \left(\frac{\partial p}{\partial T}\right)_{p,N} & \left(\frac{\partial p}{\partial p}\right)_{T,N} & \left(\frac{\partial p}{\partial N}\right)_{T,p} \\ \left(\frac{\partial S}{\partial T}\right)_{p,N} & \left(\frac{\partial S}{\partial p}\right)_{T,N} & \left(\frac{\partial S}{\partial N}\right)_{T,p} \\ \left(\frac{\partial N}{\partial T}\right)_{p,N} & \left(\frac{\partial N}{\partial p}\right)_{T,N} & \left(\frac{\partial N}{\partial N}\right)_{T,p} \end{vmatrix} \tag{3.103}$$

and:

$$\{V,S,N\} = \begin{vmatrix} \left(\frac{\partial V}{\partial T}\right)_{p,N} & \left(\frac{\partial V}{\partial p}\right)_{T,N} & \left(\frac{\partial V}{\partial N}\right)_{T,p} \\ \left(\frac{\partial S}{\partial T}\right)_{p,N} & \left(\frac{\partial S}{\partial p}\right)_{T,N} & \left(\frac{\partial S}{\partial N}\right)_{T,p} \\ \left(\frac{\partial N}{\partial T}\right)_{p,N} & \left(\frac{\partial N}{\partial p}\right)_{T,N} & \left(\frac{\partial N}{\partial N}\right)_{T,p} \end{vmatrix} \tag{3.104}$$

It may be shown that:

$$\left(\frac{\partial p}{\partial V}\right)_{S,N} = -\frac{C_p}{C_V}\frac{1}{vk_T}. \tag{3.105}$$

Hence, from (3.101) $m = C_p/C_V = \gamma$ and finally $n = \gamma$ in the case of an ideal gas.

If the process is adiabatic but no restrictions are made on the nature of the system, then $m = \gamma$ and $n = \gamma/(p \cdot k_T)$, but k_T remains unknown. To determine k_T, additional information on the system is required, such as a state equation relating the system variables and state parameters.

3.2 Real gas model for the OWC

The following hypotheses should be taken into account for a real gas:

- **A closed, thermally isolated system**. From the thermodynamic perspective, the OWC system is schematized as a chamber, nozzle and the external surrounding air. Assuming there is no heat exchange between the OWC and the atmosphere or the surrounding water, the system is thermally isolated, and equation (3.4) applies. In practice, this is not a hard restriction: exchange of mass and heat in the OWC takes place between chamber and nozzle, and between nozzle and surrounding air in the vicinity of the device. If the surrounding region is sufficiently large, then mass and heat exchange between the surrounding region and the rest of the atmosphere can be neglected without loss of generality.

- **Reversible process**. Regardless of whether the gas is treated as ideal or real, the reversibility hypothesis underpinning $L = -p\Delta V$ applies in the same form. The concept of a reversible process — step by step or globally — implies intrinsic complexity that might not be entirely applicable to the OWC process. However, if the OWC system is considered similar to a gas forced by a frictionless piston (*i.e.* the free surface inside the chamber), it is possible for any compression state inside the chamber that the system can be returned to its previous state by simply relaxing the compression force.

In consequence, the conditions required to deduce a real gas expression similar to the adiabatic law, are the same as those for the ideal model in terms of the hypothesis of a thermally isolated system and a reversible process. The only distinction lies in the fact that the real gas is described by a thermodynamic model such as the equation of state (3.42).

The foregoing rationale offers an alternative way by which to deduce the adiabatic process law, as has been shown in Section 3.1.7 regarding the polytropic equation.

We now derive the equation for a polytropic process in a real gas system. Figure 3.5 illustrates an OWC system from a thermodynamic perspective, comprising the chamber, turbine and external surrounding air. The control volume is independent of the nature of the gas inside the system. Figure 3.5 presents a general sketch of an OWC.

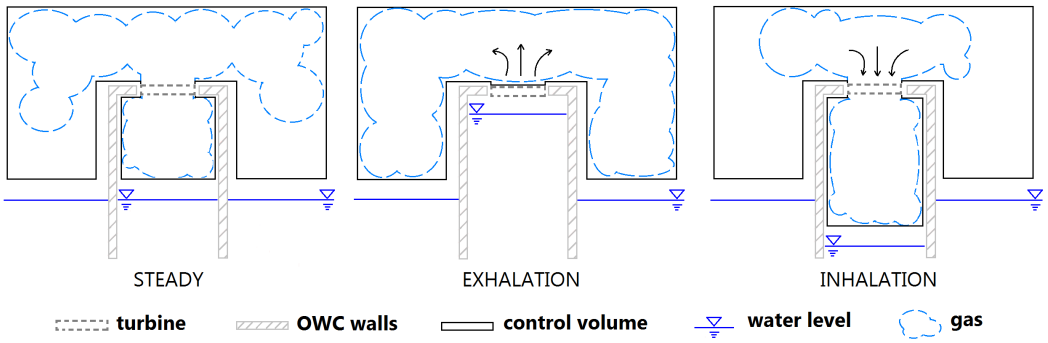

Figure 3.5: Definition sketch of OWC general scheme, showing control volume.

The starting conditions from which to deduce the equation of a polytropic process of a real gas are the same as those for an ideal gas. The only distinction lies in the equation of state for the real gas. Here, the real gas is described by either the Virial equation of state, or the Kammerling–Onnes expansion (Biel (1986) and Wisniak (2003)), which in its Leiden form is given by Prausnitz (1999):

$$\frac{pv}{R_0 T} = 1 + \frac{B}{v} + \dots \tag{3.106}$$

where p is pressure, $v = V/N$ is the molar volume, with V the volume and N representing the number of moles, $R_0 = 8.31\,\mathrm{J/mole{\cdot}K}$ is the universal gas constant, B is the second virial coefficient (to be determined later), and T is temperature. The real gas equation is defined by analogy to the ideal gas equation (Biel (1986)) as

$$pv = \mathbb{Z} R_0 T\,, \tag{3.107}$$

where $\mathbb{Z}$ is the compressibility factor, which models the difference between the real gas and equivalent ideal gas.

3.3 Polytropic system and adiabatic index n for a real gas

A thermodynamic process is a succession of different states, progressively altering from an initial equilibrium state to a final one. In this case, the process comprises a compression/exhaust cycle within a polytropic system.

3.3.1 General equation for a polytropic system in a process

The following derivations are based on the standard formulation (see e.g. Planck (1905), Biel (1986), or Cengel & Boles (2015)).

From (3.84), specific heats at constant pressure and constant volume are defined as:

$$C_p = T\left(\frac{\partial s}{\partial T}\right)_p , \tag{3.108}$$

and

$$C_v = T\left(\frac{\partial s}{\partial T}\right)_v . \tag{3.109}$$

By definition, the isothermal compressibility factor k_T is (Planck (1905)):

$$k_T = -\frac{1}{v}\left(\frac{\partial v}{\partial p}\right)_T . \tag{3.110}$$

The definitions of m given by equation (3.85) and the specific heats given by equations (3.84), (3.108) and (3.109) lead to

$$m = \left(\frac{\partial v}{\partial p}\right)_T \left(\frac{\partial p}{\partial v}\right)_y . \tag{3.111}$$

Inserting the isothermal compressibility factor given by equation (3.110) into (3.111) gives:

$$\left(\frac{\partial p}{\partial v}\right)_y = -\frac{m}{v k_T}, \tag{3.112}$$

which is commonly recalled as the *General Process Equation*. This expresses the relationship between p and v for a general process in a closed system, in which

the variable y is constant without additional restrictions. In differential form, the polytropic equation (3.94) may be written:

$$vdp + npdv = 0\,, \tag{3.113}$$

such that $(\partial p/\partial v)_y = -np/v$. Combining equations (3.112) and (3.113), the following relationship between the polytropic index n and index m is obtained:

$$n = \frac{m}{pk_T}\,. \tag{3.114}$$

Note that if the process is unknown, the form of n is undetermined with respect to the type of process.

3.3.2 General expression of n for a real gas

Next consider a real gas. Here the real gas equation is defined as a modification of the ideal gas equation (3.107). In differential form, equation (3.107) becomes

$$vdp + pdv = \mathbb{Z}R_0dT + RTd\mathbb{Z}\,. \tag{3.115}$$

The partial derivative $\left(\frac{\partial v}{\partial p}\right)_T$ is obtained from

$$\left(\frac{\partial p}{\partial p}\right)_T v + p\left(\frac{\partial v}{\partial p}\right)_T = \mathbb{Z}R_0\left(\frac{\partial T}{\partial p}\right)_T + R_0T\left(\frac{\partial \mathbb{Z}}{\partial p}\right)_T\,, \tag{3.116}$$

giving

$$\left(\frac{\partial v}{\partial p}\right)_T = -\frac{v}{p} + \frac{R_0T}{p}\left(\frac{\partial \mathbb{Z}}{\partial p}\right)_T\,. \tag{3.117}$$

Substituting equations (3.110) and (3.117) into equation (3.114), and noting the definitions of the specific heats given by equations (3.108) and (3.109), the resulting general expression for n is

$$n = \frac{m}{1 - \dfrac{p}{\mathbb{Z}}\left(\dfrac{\partial \mathbb{Z}}{\partial p}\right)_T}\,. \tag{3.118}$$

For an adiabatic process, no heat is transferred to the surrounding universe, so the magnitude y takes the form of entropy, and so $y = s$. Hence, from equation

(3.85):

$$m = \frac{C_p}{C_v}. \tag{3.119}$$

Equation (3.118) then becomes

$$\boxed{n = \frac{C_p/C_v}{1 - \dfrac{p}{\mathbb{Z}}\left(\dfrac{\partial \mathbb{Z}}{\partial p}\right)_T}} \tag{3.120}$$

The foregoing analytical form of n given by equation (3.120), given that $pv^n = const$, allows us to represent mathematically a real gas process in the continuity equation, applied to an OWC air chamber. Note that for the hypothetical case of an ideal gas, then $\mathbb{Z} = 1$ and equation (3.120) would reduce to $n = C_p/C_v$, the usual form.

The specific heats, C_p and C_v, refer to a real gas, with expressions that relate to the virial coefficients through thermodynamic formalism, as discussed in Section 3.3.3. Then, equation (3.120) represents the polytropic index for a general process in a real–gas system. Nevertheless, a simpler form of n than given by equation (3.120) would be of advantage. Taking into account the definition of the compressibility factor $\mathbb{Z}$ given by Tsonopoulos & Heidman (1990),

$$\mathbb{Z} = 1 + \frac{B' p_c p_r}{R_g T_c T_r} = 1 + \frac{B p_c p_r}{R_0 T_c T_r}\,, \tag{3.121}$$

where $B' = B/M$ with M the molar weight. Note that $p_r = \frac{p}{p_c}$ and $T_r = \frac{T}{T_c}$ are the reduced pressure and reduced temperature. For water vapour, $p_c = 220.89 \cdot 10^5$ Pa and $T_c = 647$ K. So, writing

$$\left(\frac{\partial \mathbb{Z}}{\partial p}\right)_T = \frac{B}{R_0 T} = \frac{B}{R_0 T_c}\frac{1}{T_r}\,, \tag{3.122}$$

or

$$\frac{p}{\mathbb{Z}}\left(\frac{\partial \mathbb{Z}}{\partial p}\right)_T = \frac{1}{\mathbb{Z}}\frac{B p_c}{R_0 T_c}\frac{p_r}{T_r}\,, \tag{3.123}$$

we have

$$1 - \frac{p}{\mathbb{Z}}\left(\frac{\partial \mathbb{Z}}{\partial p}\right)_T = \frac{1}{\mathbb{Z}}\,. \tag{3.124}$$

Inserting equation (3.124) in equation (3.120), a new expression is obtained for

the adiabatic index n for a real gas:

$$\boxed{n = \mathbb{Z}\frac{C_p}{C_v}} \tag{3.125}$$

The compressibility factor is deduced from the Tsonopoulos-Heidman innovation, and the specific heats for the real gas are expressed as functions of ideal gas values, as defined in the next section. This form of n is simple, compact and easy to work with.

3.3.3 The new adiabatic index in terms of pressure and temperature

We now analyse the dependence of n on pressure and temperature. Taking into account the formulation given by equation (3.125), figures 3.6 and 3.7 present a 3D surface plot and a 2D contour plot of the functional dependence of n on p and T. The temperature range occupies a range of $[10 - 25]°C$ and the pressure a range of $[0 - 2500]$ Pa. The plots are given in terms of the reduced temperature and pressure.

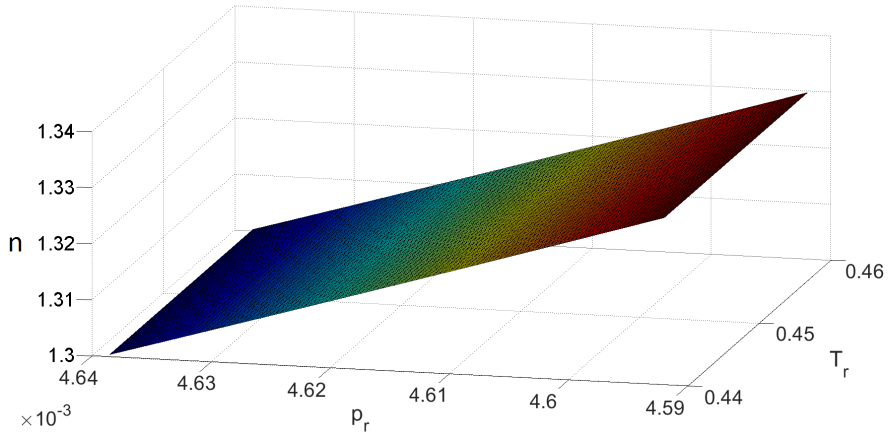

Figure 3.6: 3D plot for adiabatic index n for a real gas.

There is a discernible linear dependence of n on pressure over the parameter range considered. Taking a reduced pressure $p_r = 4.59 \times 10^{-3}$, equivalent to the atmospheric pressure, the adiabatic index n reaches a maximum at 1.33, decreasing linearly towards 1.3 as the relative pressure increases.

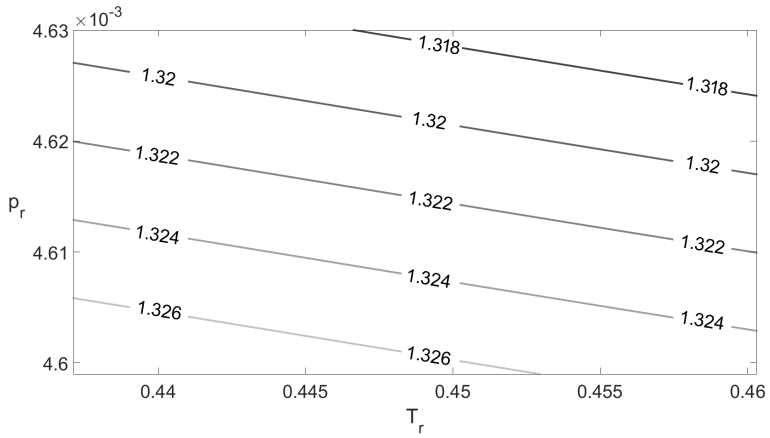

Figure 3.7: Contour plot of the variation in adiabatic index n with reduced temperature and reduced pressure for a real gas.

Next, consider the constant in equation (3.94), which is assumed independent of the modified values of v and p for a real gas. The constant remains stationary for varying n and v. Table 3.1 lists values of the constant for different combinations of relative temperature and pressure. This confirms the initial hypothesis that the adiabatic process remains adiabatic, independent of the value of n.

Constant value for $pv^n = constant$		
$(T_r,\ p_r)$	**Ideal**	**Real**
$(0.44\,,\ 4.605 \times 10^{-3})$	7.804×10^4	7.851×10^4
$(0.45\,,\ 4.620 \times 10^{-3})$	7.804×10^4	7.851×10^4
$(0.46\,,\ 4.635 \times 10^{-3})$	7.804×10^4	7.851×10^4

Table 3.1: Values of the process equation constant obtained using ideal and real gas model.

3.4 Experimental validation

To validate the proposed thermodynamic model, predictions are compared against experimental data obtained by Medina-Lopez *et al.* (2016), as presented in Chapter 2. The experiments investigated steady air-water vapour mixture flow through a

chamber and turbine, in order to provide a more complete understanding of the basic thermodynamics governing OWC performance.

Here, the real gas model is used to predict the change between inner and outer system variables, while preserving mass flow rate continuity through the turbine. It should be noted that conservation of mass was not ensured when applying the adiabatic equation for an ideal gas to calculate the temperature at the physical OWC outlet used in the laboratory tests. Experimental data were inserted in the formulation of enthalpy to calculate the theoretical outlet velocity, and then used to obtain the mass flow balance in the OWC chamber (Medina-Lopez *et al.* (2016)).

Figure 3.5 indicates the key stages involved in the experimental tests performed by Medina-Lopez *et al.* (2016). Experimental data were acquired on flow velocity, air temperature, and pressure at the turbine inlet (U_{in}, T_g, p_g), relative humidity in the chamber RH, and pressure at the turbine outlet p_{out}. During the experiments undertaken by Medina-Lopez *et al.* (2016), measurements were made of RH at the outlet and U_{out}, but due to non-correspondence between the ideal law applied to the theoretical control volume and the measured variables, a real gas calculation proved necessary in order to confirm the starting hypothesis (real gas under adiabatic process).

Commencing from the modified adiabatic index for a real gas, equation (3.125), values of $\mathbb{Z}$, C_p and C_v for a real gas are required, which are obtained from the experimental data. Using this approach, the adiabatic temperature at the outlet for a real gas can be calculated. Here, the adiabatic index for real gas is obtained from equation (3.125) as a function of $\mathbb{Z}$, C_p and C_v. Moreover, a real gas calculation for the outlet velocity is needed. Finally, the real gas density is calculated. Following Medina-Lopez *et al.* (2016), the validation procedure is summarised below:

1. Calculate the real gas density ρ_g from:

$$\rho_g = \rho_a \frac{1+r}{1+1.608r}\,, \tag{3.126}$$

where ρ_a is the dry air density and $r = \frac{\epsilon e}{p_g - e}$ is the absolute humidity. ϵ is the ratio between dry air and water vapour gas constants $\epsilon = R_a/R_v = 0.622$. p_g

is the gas pressure inside the chamber. The vapour pressure e is $e = RHe_s$. Relative humidity (RH) is measured experimentally, and saturated vapour pressure (e_s) can be evaluated from the Clapeyron-Clausius equation, which depends solely on temperature.

2. Calculate the compressibility factor $\mathbb{Z}$ using equation (3.121), where the second term is defined by equation (3.67) and the f coefficients are calculated through the Tsonopoulos-Heidman approximation, defined by equation (3.68).

3. Calculate real gas specific heats, C_p and C_v, from equations (3.57) and (3.66).

4. Calculate the adiabatic index for real gas n from equation (3.125).

5. Calculate the gas temperature at the outlet as

$$T_{out}^{ad} = T_g \left(\frac{p_{out}}{p_{in}} \right)^{\left(\frac{n-1}{n}\right)} , \tag{3.127}$$

where T_g is the temperature of air in the OWC chamber, and p_{out} and p_{in} are the outlet and inlet air pressures, respectively.

6. Calculate the enthalpy at the outlet for a real gas as

$$H = H^* + \delta H^* p_{out} , \tag{3.128}$$

where $H^* = C_p^* T + \frac{1}{2}U^2$ is the enthalpy of the ideal gas at the outlet. The deviation from the ideal enthalpy δH can be calculated as

$$\delta H^* = \frac{R_g T_c}{p_c} \left[(f_0 + \chi_m f_2) - T_r \frac{d}{dT_r} (f_0 + \chi_m f_2) \right] . \tag{3.129}$$

7. Calculate the outlet velocity from the enthalpy definition given by

$$U_{out} = \sqrt{2 \left(H_g - C_p T_{out} - \delta H^* p_{out} \right)} . \tag{3.130}$$

8. Finally, employ mass conservation between both sides of the turbine (assuming that inlet and outlet have the same cross-sectional area) to obtain

$$\rho_g^{in} U_{in} = \rho_g^{out} U_{out} . \tag{3.131}$$

Comparison between mass flows obtained applying the ideal and real gas models to the adiabatic process at the turbine outlet is now made, with respect to the inlet mass flow.

MASS FLOW RATE (kg/m^{2}s)		
IN	**OUT** Adiabatic **Ideal**	**OUT** Adiabatic **Real**
Dry tests		
2.077	6.198	2.054
5.667	13.296	5.605
9.174	20.303	9.074
12.559	27.109	12.423
15.738	33.397	15.567
Min. humidity tests		
2.242	4.848	2.218
3.426	9.790	3.390
7.989	16.654	7.905
11.146	23.469	11.030
14.296	30.920	14.148
Max. humidity tests		
2.502	5.488	2.475
5.437	10.825	5.381
7.683	16.432	7.607
9.926	22.672	9.828
12.543	29.614	12.421

Table 3.2: Mass flow conservation tests, comparing measured inflow rate against predicted outflow rates using ideal and real gas models.

Table 3.2 lists the measured inlet and theoretical outlet mass flow rates. There

is very good agreement between the predicted mass flow rate obtained using the real gas formulation and the measured mass flow rate. This is not the case for the ideal gas predictions. The present calculations, which use the new approximation for the adiabatic index n for real gas, ensure mass conservation holds within the system. It should of course be noted that at steady state equilibrium, the inflow and outflow mass flow rates are equal.

The ideal gas formulation does not fully guarantee conservation, and so should not be applied in cases where humidity is present. The modified definition leads to a revised adiabatic index that is below the classical value for dry air of 1.4. Moreover, the fact that mass conservation is achieved through the real gas formulation confirms the starting hypothesis. Here, the real gas hypothesis enables the theoretical model to represent properly actual conditions present in OWC wave energy converters.

3.5 Discussion on the use of the *Tsonopoulos-Heidman* formulation for the virial coefficient B

The value of B used herein has been determined from the definition given by Tsonopoulos & Heidman (1990), commonly known as the *Tsonopoluos-Heidamn innovation*. We now check the validity of this approach. The *Tsonopoulos* definition was first published in 1974, and comes from the *Pitzer-Curl correlation*, (Pitzer & Curl (1957)) which itself derives from the *Stockmayer & Beattie* (*S-B*) equations, presented by Stockmayer (1942). The *Lennard-Jones potential*, used as the starting point in solving the *S-B* equations, represents both the attractive and repulsive relations between atoms through statistical mechanics. The *S-B* equations convert the molecular potential constants to macroscopic critical constants. The equations were originally validated experimentally for methane, butane, and their mixtures. However, a problem arises with Methane and Butane in that their acentric factor is not zero ($\omega \neq 0$). This is the reason why *Pitzer-Curl* extended the results to argon, krypton and xenon, three gases with zero acentric factor, and found that the *S-B* equation remain valid for these gases. Noting that the acentric factor for water is also zero (the H_2O molecule is symmetric, with oxygen in the centre and the two hydrogen atoms at opposite sides), these results

are also applicable to water. Tsonopoulos & Heidman (1990) slightly modified the *Pitzer-Curl correlation* to improve the fit at low temperatures (up to 25°C for water vapour) by addition of a further T^{-8} term. The present formulation is therefore entirely based on statistical mechanics, except for slight empirical adjustment using experimental data. It can therefore be concluded that the chosen formulation fits the requirements of a system containing a water vapour-air mixture.

3.6 Conclusions

To date most analyses of the thermodynamic behaviour of an oscillating water column have been based on ideal gas theory. In this chapter, the author has extended the analysis to a real gas by deriving mathematical expressions for the adiabatic index which accounts for a water vapour-dry air mixture. The resulting index can be readily implemented in a numerical model, and is very straightforward to apply. Modified expressions have been developed for the specific heat coefficients, entropy, internal energy, enthalpy, chemical potential, and speed of sound, all of which apply to a real gas. Unlike ideal gas theory, the real gas theory is found to give excellent agreement with experimental data on mass flow conservation and energy balance through a laboratory-scale OWC. It is found that the adiabatic index depends linearly on temperature and pressure.

Chapter 4

Numerical model

This chapter presents details of a numerical model configuration using Fluent® for the simulation of a linear turbine. Here, dry air conditions are tested (model **NM1**, see table 1.1 for reference).

4.1 Fluent® characteristics

ANSYS Fluent® is used herein to simulate numerically waves in a flume. Fluent® is based on the finite volume method. The domain is discretized into a finite set of control volumes or cells. For each cell, ANSYS Fluent ® solves discretized conservation equations of mass, momentum and energy. Additional transport equations are also solved when the flow is turbulent. Laminar flow is assumed.

Next, the conservation equations for laminar flow in an inertial (non-accelerating) reference frame are presented, Fluent (2006).

4.1.1 Mass conservation equation

The mass conservation equation is given by:

$$\frac{\partial \rho}{\partial t} + \nabla \cdot (\rho \overrightarrow{v}) = S_m \,, \tag{4.1}$$

where ρ is density, t is time, $\overrightarrow{v}$ is a velocity vector, and S_m is a source term representing the mass added to the continuous phase from the dispersed second

phase. In this thesis the continuous phase is formed by water, and the dispersed second phase is air.

4.1.2 Momentum conservation equations

Conservation of momentum in an inertial (non–accelerating) reference frame is described by:

$$\frac{\partial}{\partial t}(\rho\overrightarrow{v}) + \nabla\cdot(\rho\overrightarrow{v}\overrightarrow{v}) = -\nabla p + \nabla\cdot(\overline{\tau}) + \rho\overrightarrow{g} + \overrightarrow{F}\,, \tag{4.2}$$

where p is the static pressure, $\overline{\tau}$ is the stress tensor, $\rho\overrightarrow{g}$ is the gravitational body force, and $\overrightarrow{F}$ are external body forces (such as those that arise from interaction with the disperse phase). $\overrightarrow{F}$ contains other source terms such as porous–media sources.

The stress tensor is given by:

$$\overline{\tau} = \mu\left[\left(\nabla\overrightarrow{v} + \nabla\overrightarrow{v}^{T}\right) - \frac{2}{3}\nabla\cdot\overrightarrow{v}I)\right]\,, \tag{4.3}$$

where μ is the molecular viscosity and I is the unit tensor. The second term on the right hand side is the effect of volume dilation.

4.1.3 Energy conservation equation

Conservation of energy is described by:

$$\frac{\partial}{\partial t}(\rho E) + \nabla\cdot(\overrightarrow{v}(\rho E + p)) = -\nabla\left(k\nabla T\right) + S_h\,, \tag{4.4}$$

where E is energy, k is the thermal conductivity, T represents temperature, and S_h includes any volumetric heat sources and radiation.

4.1.4 The finite volume method

All equations are solved in order to render the flow field. In general terms, for each unit volume or cell the following equation is applied:

$$\frac{\partial}{\partial t}\int_V \rho\phi dV + \int_A \rho\phi V dA = \int_A \Lambda\nabla\phi dA + \int_V S_\phi dV\,, \tag{4.5}$$

where the first part is the unsteady term, the second part is the convection term, the third part is the diffusion term, and the fourth part is the generation term. Note that the value of ϕ depends on the equation to be solved: for mass conservation $\phi = 1$, for momentum conservation $\phi = u\,, v$,or w (the velocity component depending on direction), and for energy conservation $\phi = h$ (enthalpy). Λ is the diffusion coefficient.

Each transport equation is discretized into algebraic form. For example, for cell "P", equation (4.5) becomes:

$$\frac{(\rho\phi_p)^{t+\Delta t} - (\rho\phi_p)^t}{\Delta t}\Delta V + \sum_{faces} \rho_f \phi_f V_f A_f = \sum_{faces} \Lambda_f \left(\Delta\phi\right)_{\perp,f} A_f + S_\phi \Delta V\,. \quad (4.6)$$

The discretized equations require information at both cell centres and faces. Field data, such as material properties, velocities, etc., are stored at cell centres. Face values are interpolated in terms of local and adjacent cell values. The sets of equations (mass, momentum and energy) are solved iteratively until convergence is reached. Convergence means that all discrete conservation equations are satisfied in all cells until a user–specified tolerance is reached, or the solution no longer changes with subsequent iterations. The iteration process ends when the overall mass, momentum and energy balances have been achieved.

4.1.5 Volume of fluid (VOF)

The VOF model simulates two or more immiscible fluids by solving a single set of momentum equations and tracking the volume fraction of each of the fluids throughout the domain. This method is used herein to locate accurately any liquid-gas interface, in particular, the water surface. The VOF method only works with pressure-based solvers, where the pressure equation is derived from the continuity and momentum equations in such a way that the velocity field, corrected by the pressure, satisfies continuity.

4.1.6 Boundary conditions

Boundary types available in Fluent® are classified as:

- Flow inlet and exit boundaries: pressure inlet, velocity inlet, mass flow inlet,

and inlet vent, intake fan, pressure outlet, pressure far-field, outflow, outlet vent, and exhaust fan.

- Wall, repeating, and pole boundaries: wall, symmetry, periodic, and axis.
- Internal cell zones: fluid, and solid (porous is a type of fluid zone).
- Internal face boundaries: fan, radiator, porous jump, wall, and interior.

The boundary conditions used in this thesis are:

- Wall. Wall boundary conditions are used to bound fluid and solid regions. In viscous flows, the no-slip boundary condition is enforced at walls by default.
- Pressure outlet. Pressure outlet boundary conditions require the specification of a static (gauge) pressure at the outlet boundary. In this case atmospheric pressure is used as a reference.
- Interior. Used for double–sided faces where fluid is going to be placed. Different characteristics can be attributed to interior zones (such as porosity, hydraulic conductivity, etc.).
- Fluid. Actual fluid cells where calculations are made. Different phases can be placed with different densities in the same zone of fluid.

This conditions are specified for OWC and flume in Section 4.3.

4.2 Wave generation. Model validation

Waves are generated in the flume by a piston–type paddle located at the left side of the flume. The paddle motion is enabled by a dynamic–mesh scheme assigned to the paddle boundary. Time–dependent variables determining the instantaneous paddle position and velocity are implemented in a compiled user–defined–function (UDF) in the model, following Biésel's theory for a piston–type paddle, Hughes (1993):

$$\begin{aligned} x_{paddle} &= \frac{S_0}{2}\cos\frac{2\pi t}{T}, \\ U_{paddle} &= -\frac{S_0\pi}{T}\sin\frac{2\pi t}{T}, \\ S_0 &= H\frac{2k_0h + \sinh 2k_0h}{4\sinh^2 k_0h}, \end{aligned} \tag{4.7}$$

where x_{paddle} is the paddle displacement along the horizontal axis, U_{paddle} is the paddle displacement velocity, S_0 is the paddle stroke, H is the wave height, k_0 is the wave number, h is the water depth at the paddle location, T is the wave period and t is the simulation time. The dynamic mesh ensures the harmonic oscillation of the free surface described by equations (4.7).

The numerical model for wave generation in Fluent® used in this thesis has been validated against experimental data. The experiments were carried out in a wave flume at the *Andalusian Institue for Earth System Research, Universidad de Granada* (Spain).

Figure 4.1 shows the experimental set up. A 23 m long wave flume is considered, with a dissipation beach at the right end, and a piston–type paddle located at the left end. The water depth is 0.4 m and the total lateral wall height of the flume is 0.8 m. Three wave gauges are located in the central section of the flume to collect data from which to analyse incident and reflected wave components. For this purpose, a 2D numerical flume, shown in figure 4.2, has been meshed in GAMBIT® and configured in Fluent® to check the validity of the numerical model. The mesh has a total of 43, 544 quadrilateral cells of side length 0.01m. Finer meshes have been checked in order to verify the accuracy of the results, but no significant differences have been observed in terms of wave propagation and surface elevation detection. Here, the Fluent® solver is configured to *laminar*

and *VOF* (Volume of Fluid) with air as phase 1 and water as phase 2. The pressure–velocity coupling is set to *PISO* (Pressure Implicit Split Operator) and the discretization scheme for pressure is set to *PRESTO* (Pressure Staggering Options), while for momentum equations are set to 1^{st} *order upwind*. The free surface reconstruction is set to *Geo-Reconstruct*.

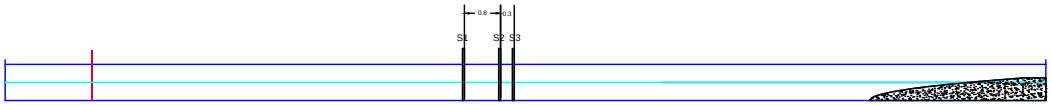

Figure 4.1: Experimental set up for numerical model validation.

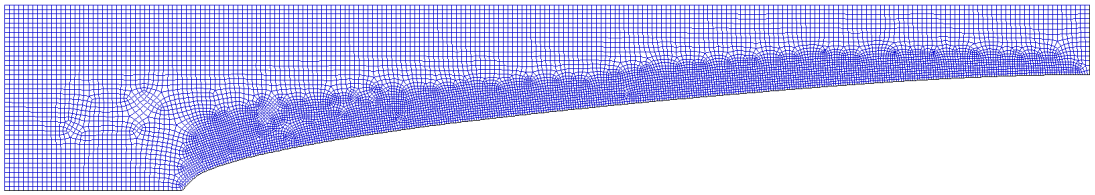

Figure 4.2: Detailed mesh in the dissipative beach region.

Table 4.1 summarizes the set of regular wave heights and wave periods configured for validation of the numerical model, following the experimental test cases.

H (m)	T (s)
0.113	1.5
0.052	3

Table 4.1: Model validation test parameters.

The results exhibit satisfactory agreement between the experimental and numerical free surface elevation series depicted in figures 4.3 and 4.4. At the beginning of the simulation there is a slight out-of-phase mismatch between the numerical and experimental waveforms (figure 4.3). The mismatch is caused by the ramping up of the experimental paddle, which is not replicated by the numerical paddle. Even so, the predicted and experimental free surface elevation time series evolve to match in phase and height as time advances (figure 4.4).

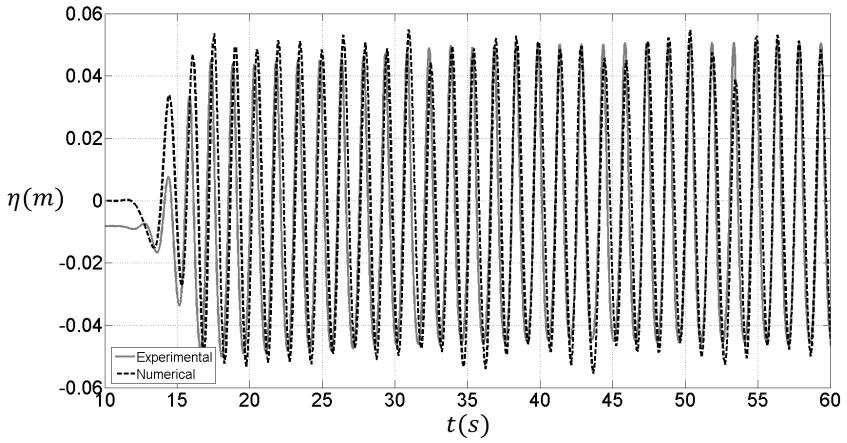

Figure 4.3: Measured and predicted free surface elevation time series for $H = 0.113\,\text{m}$, $T = 1.5\,\text{s}$: first part of the test.

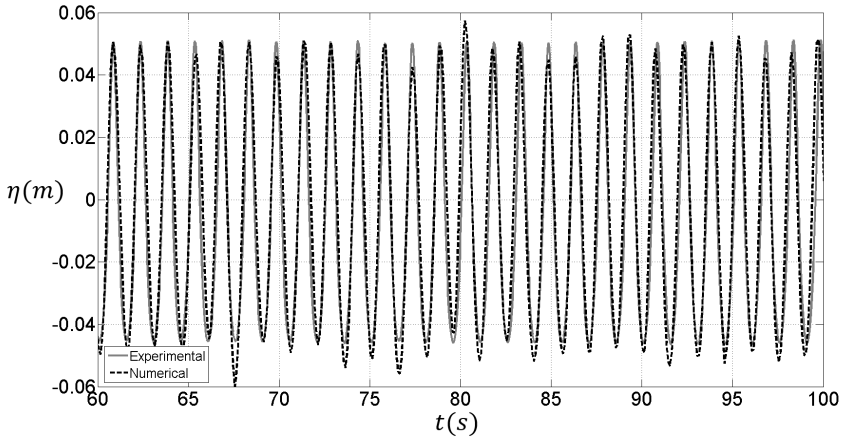

Figure 4.4: Measured and predicted free surface elevation time series for $H = 0.113\,\text{m}$, $T = 1.5\,\text{s}$: final part of the test.

Similar comments apply to the test where $H = 0.052\,\text{m}$, $T = 3\,\text{s}$, see figure 4.5. However, in the final part of the test, figure 4.6, peak enhancement is present every three wave crests. The magnitude of this enhancement is about $0.005\,\text{m}$. This phenomenon is present for very small wave heights; in tests where $H > 0.1\,\text{m}$ this is not observed. The author believes the mismatch occurs because of the size of the water–air inter–phase in the numerical model, which is close to the wave height in this case.

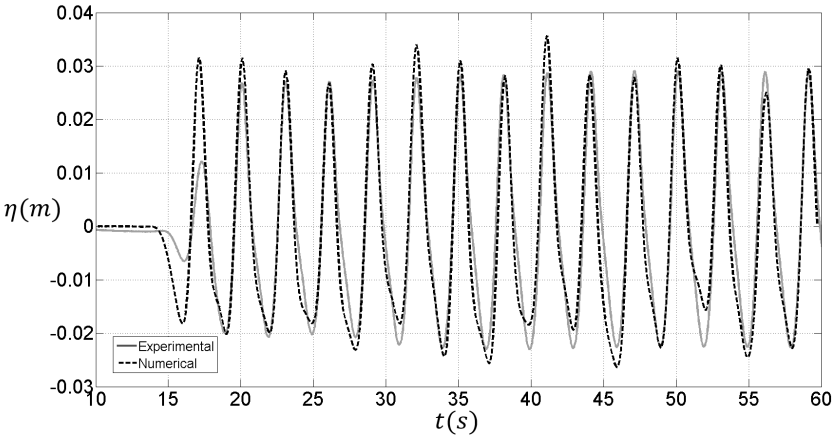

Figure 4.5: Measured and predicted free surface elevation time series for $H = 0.052\,\text{m}$, $T = 3\,\text{s}$: first part of the test.

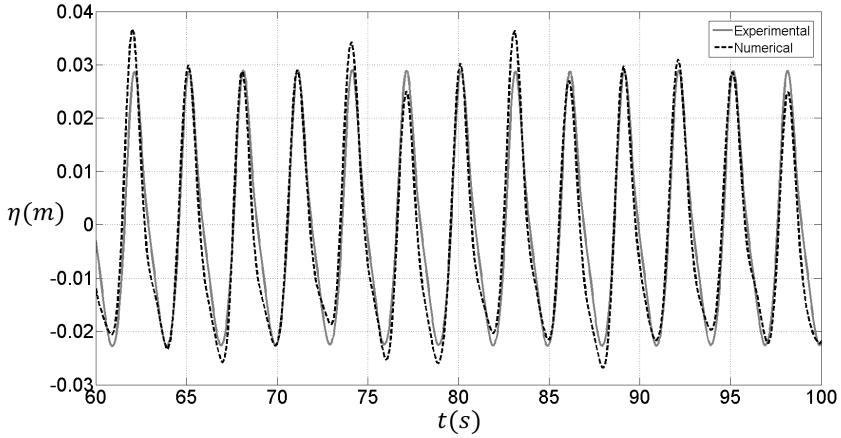

Figure 4.6: Measured and predicted free surface elevation time series for $H = 0.052\,\text{m}$, $T = 3\,\text{s}$: final part of the test.

4.3 Insertion of OWC in Fluent®

Without loss of generality, a simple OWC model has been established according to the configuration in figure 4.7, which relates to an OWC tested in a wind tunnel at the *Andalusian Institute for Earth System Research, Universidad de Granada* (Spain), from which pressure and velocity data are used to calibrate the OWC model. This is discussed in more detail in Section 4.4.2. The OWC consists of a chamber of diameter $0.29\,m$ and reference height $h_{ref} = 1.5\,m$ with respect to the mean reference level. The chamber is closed at its roof by a Wells turbine. The diameter of the turbine hub is $0.192\,m$ leaving an annular gap between hub and blade tips $0.049\,m$ wide.

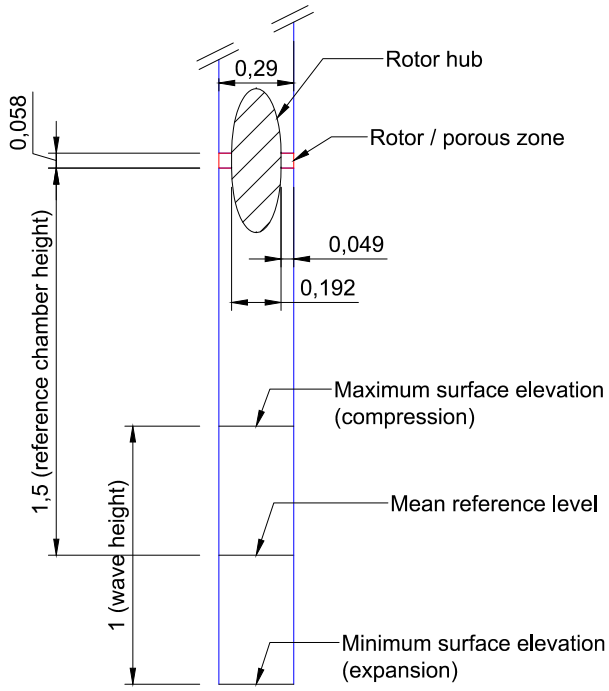

Figure 4.7: OWC model.

Tests were performed in a wind tunnel to confirm the linear performance in terms of pressure drop and air flow velocity, following Benslimane (2013). A Wells turbine with standard blades is used as the PTO device. The characteristics of the turbine, as well as details of the experiments and validation of the linear model are presented in Section 4.4.3.4.

The boundary conditions selected for the OWC and flume are presented in figure 4.8.

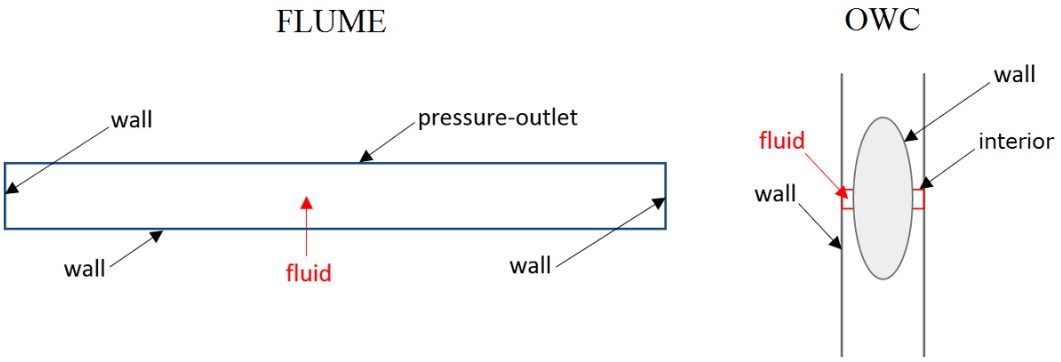

Figure 4.8: Boundary conditions

4.3.1 Fluent® simulation with porous zone

When simulating the OWC and Wells turbine performance in Fluent®, the main issue to overcome is the setting of an appropriate value for the hypothetical rotational velocity of the turbine that matches the actual value of the inlet flow and pressure drop. If the rotational velocity does not match the actual velocity for a given inlet, the pressure drop values will deviate from those expected according to the real turbine performance.

Various numerical models can be used to represent the dynamics of flow through a turbine, e.g. Single Rotating Reference Frame (SRF), Virtual Blade Model (VBM), and Actuator Disk Model (ADM), Javaherchi (2010). The first two models are very accurate, and provide very good results related to velocity field measurements, Javaherchi (2010). The third model is not straightforward to apply when studying the velocity field around blades. However, if the main goal is to identify control volume relations between inlet velocity and pressure drop instead of turbine dynamics and kinematics (such as drag and lift forces on blades, axial and radial velocity components through vanes, air tangential velocity between blade tip and external hub, etc.), then the ADM is an accurate option. In certain cases, the model can be configured with a boundary condition representing the turbine characteristic relation, defined as the ratio between pressure drop and air flow, which for the case of a linear turbine is constant (see Teixeira *et al.* (2013)).

In other cases, the solution can be provided by the ADM. For further details, see Raghunathan (1995) and Javaherchi (2010).

Here, the proportionality between flow discharge and pressure drop in the turbine response is achieved through the implementation of an ADM, where the aerodynamic effect of rotating blades is described by a pressure discontinuity over an infinitely thin disk with an area equal to the swept area of the rotor. The thin disk is modelled as a porous media that supports a pressure difference with continuous distribution of the velocity field. A more complete explanation can be found in Appendix IV.

The way Fluent® implements the ADM is by enabling a porous zone configuration with known porosity d, viscous resistance $1/\alpha$ (where α is the permeability) and inertial resistance coefficient C_2. Additional datasets with flow velocities and pressure drops or turbine performance characteristic relations are used for calibration purposes, Falcão & Justino (1999), Benslimane (2014). In the following discussion, the Fluent® configuration addresses the concepts of the ADM. The compression/expansion cycles in the OWC can be forced in two ways:

1. Simulation of the OWC chamber as an isolated element. Free surface oscillations inside the chamber as generated by a dynamic mesh and UDF scheme representing the water displacement.

2. Simulation of a wave flume in which the OWC is forced by the wave action. Waves are generated in the flume by a dynamic mesh and a UDF scheme representing the paddle motion. The free surface inside the chamber oscillates according to the external wave action.

The main issue with the first approach is the lack of visibility of the whole wave–structure interaction process, because the analysis is focused on the OWC chamber. The second approach is computationally less cost effective, but its results allow a more complete analysis.

4.3.1.1 Porous zone configuration

Porous media are modelled by the addition of a momentum source term to the standard fluid flow equations. The source term is composed of two parts: a viscous

loss term (Darcy, the first term on the right-hand side of equation (4.8)) , and an inertial loss term (the second term on the right-hand side of equation (4.8)), Fluent (2006):

$$S_i = -\left(\sum_{j=1}^{3} D_{ij}\mu v_j + \sum_{j=1}^{3} C_{ij}\frac{1}{2}\rho|v|v_j\right), \tag{4.8}$$

where S is the source term for the momentum equation, μ is the dynamic viscosity, v_j is the *j-th* velocity component, ρ is the fluid density, $|v|$ is the magnitude of the velocity and D and C are prescribed matrices. This momentum source contributes to the pressure gradient in the porous cell, creating a pressure drop that is proportional to the fluid velocity (or velocity squared) in the cell.

Equation (4.8) can be adapted for a simple homogeneous porous media:

$$S_i = -\left(\frac{\mu}{\alpha}v_i + C_2\frac{1}{2}\rho|v|v_i\right), \tag{4.9}$$

where α is the permeability and C_2 is the inertial resistance factor.

The porous zone configuration addresses the following scheme, Fluent (2006):

1. All the geometric characteristics for the turbine are known. Solidity, hub, and blade tip radii are the most relevant characteristics.

2. Net air gap section S_{ag} and air gap velocity U_{ag} are calculated from continuity. Turbine porosity is determined as the ratio between air gap and turbine sections:
$$d = \frac{S_{ag}}{S_{turbine}}. \tag{4.10}$$

3. The loss coeffcient K_L through the turbine gaps is calculated as:
$$K_L = \frac{2\Delta p}{\rho_{air}U_{ag}^2}, \tag{4.11}$$
where Δp is pressure drop, ρ_{air} is air density and U_{ag} is air velocity through the turbine gaps.

4. The porous zone viscous resistance is set such that $1/\alpha = 0$

5. The porous zone equivalent loss coefficient is calculated as:

$$K'_L = K_L \left(\frac{U_{ag}}{U_{ring}} \right)^2 , \tag{4.12}$$

where U_{ring} is the air velocity in the whole ring–shaped turbine disk. The equivalent loss coefficient represents the required loss for a full section with the central hub but without blades, *i.e.* a ring–like section, to provide the same pressure drop as over the section with blades. The porous zone replaces the rotating blades for simulation purposes. Therefore, if use is made of experimental values of pressure drop, the effect of rotation is implicit in the values of K_L and K'_L for a given turbine geometry.

6. The inertial coefficient C_2 for each velocity inlet and pressure drop is then calculated (Benslimane (2013)) from:

$$C_2 = \frac{K'_L}{\delta}, \tag{4.13}$$

where δ is the porous zone thickness, which is equal to the rotor thickness.

7. The viscous resistance coefficient is $1/\alpha$ in all directions.

The numerical model configuration is completed with a dynamic mesh and a UDF representing the harmonic oscillation of the free surface described by (4.7).

4.4 Case study: OWC with linear turbine in wave flume. Dry air conditions

A simple off–shore OWC converter is implemented in a numerical flume in Fluent®. The problem is simplified to represent an infinitely wide OWC slot subsequently represented by a 2D domain.

The 2D flume is 200 m long, 12 m high, and has 5 m depth, see figure 4.9. The OWC is placed at the centre of the domain and submerged 2.5 m below still water level. Figure 4.7 depicts a detailed scheme of the OWC . The flume is designed to be of length three times that of the target wavelength. Although the relative length is slightly smaller than that of other proposed models, such as that of Teixeira *et al.* (2013), the present relative length is sufficient to visualize the basic phenomena of interest without loss of generality.

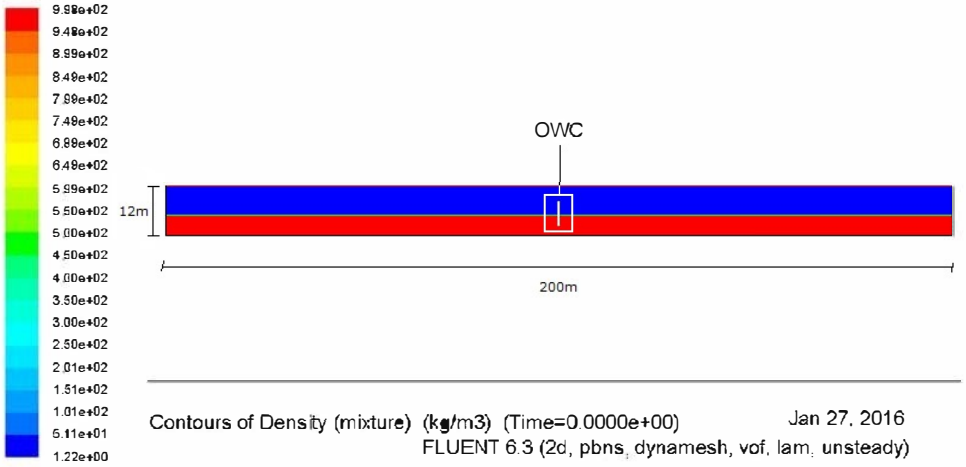

Figure 4.9: Numerical flume in Fluent®. Paddle to the left of OWC device.

4.4.1 Model set up

For the OWC simulation, the numerical domain is meshed in GAMBIT® under a *Tri/Pave* scheme with maximum spacing setting of $0.1\,m$ and a minimum element size of $0.001\,m$, see figure 4.10. To help obtain a smoother structure in the final mesh, a pre–meshing scheme is applied to the hub edges inside the chamber, with spacing of $0.01\,m$. As a result, a mesh with $221,578$ elements is generated. The Fluent® solver is configured to *laminar* and *VOF* (Volume of Fluid) with air as

phase 1 and water as phase 2. The pressure–velocity coupling is set to *PISO* (Pressure Implicit Split Operator) and the discretization scheme for pressure is set to *PRESTO* (Pressure Staggering Options), while that for the momentum equations is set to 1^{st} *order upwind*. The free surface reconstruction is set to *Geo-Reconstruct*.

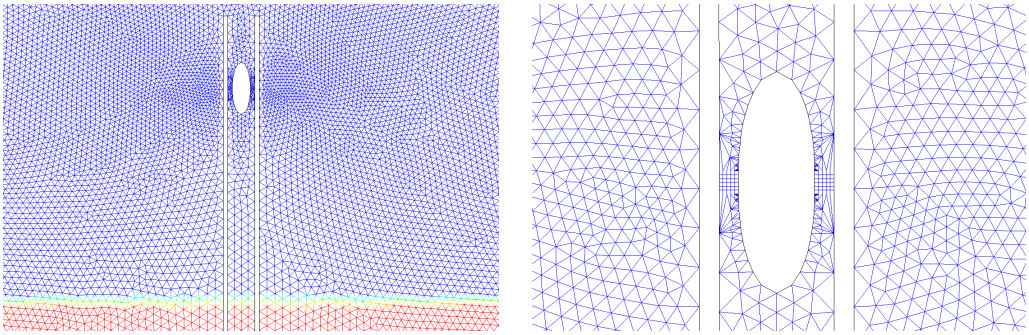

Figure 4.10: Detailed view of OWC device in the numerical flume (left) and mesh detail around porous layer (right).

For the purpose of the present thesis, regular waves are generated up to $2\,m$ height and $8\,s$ period according to low–average wave climate conditions, with intermediate water depth propagation conditions following previous reference cases, Teixeira *et al.* (2013). Irregular waves are not considered.

4.4.2 Porous zone configuration for linear turbine simulation

The porous zone settings are the same for air and water phases, accounting for the fact that water never reaches the porous zone for the generated waves. The inertial resistance coefficient is set to $C_2 = 0$ for both x (horizontal) and y (vertical) directions. The viscous resistance coefficient is set to $1/\alpha = 10^7\,m^{-2}$ in the y direction, whereas for the x direction the coefficient is set to $1/\alpha = 10^{10}\,m^{-2}$ in order to prevent undesirable radial flow effects. The viscous resistance coefficients are adjusted following measurements obtained for a Wells turbine in a wind tunnel, see figures 4.11 and 4.12, Benslimane (2013). The performance of the experimental turbine model shows a linear dependence between pressure drop and flow rate. For flow rates under $0.26\,m^3/s$, a stall effect seems to be present and the turbine is not self–starting, as will be discussed later.

The adjustment of coefficients ensures the same relationship results between pressure drop and flow velocity as in the experiments. The turbine geometry is the same as in the numerical model in terms of external diameter, hub design, and hub to tip radio. The experimental turbine characteristics are listed in table 4.2 and sketched in figure 4.13. The turbine has 8 right blades each with profiles of a *NACA0018* airfoil with constant chord length.

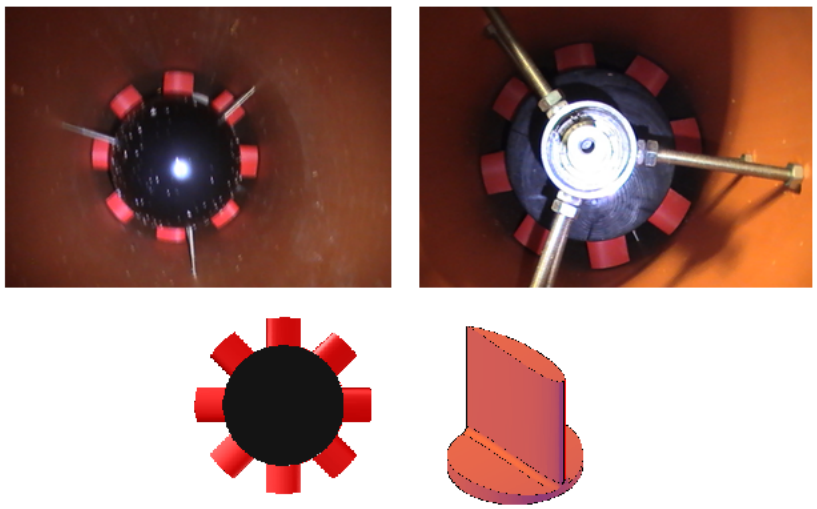

Figure 4.11: Photographs of the experimental turbine inlet (top left) and outlet (top right). 3D composition of turbine and blade (bottom). [Source: Benslimane (2013)]

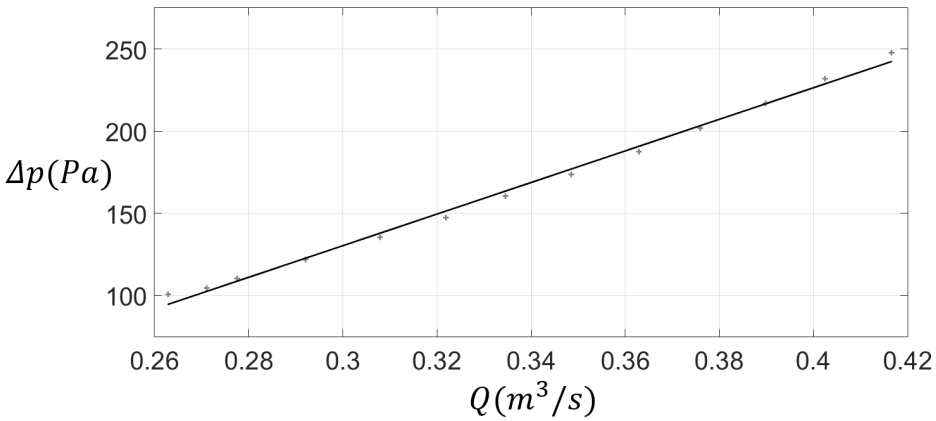

Figure 4.12: Pressure drop as a function of flow velocity for the experimental turbine. [Source: Benslimane (2013)]

Blade airfoil	*NACA0018*
D	$0.3\,m$
c	$52.2\,\text{mm}$ (constant)
N_b	8
R_h	$96\,\text{mm}$
R_t	$144\,\text{mm}$
$h = R_h/R_t$	0.67
σ	0.55

Table 4.2: Experimental turbine characteristics. [Source: Benslimane (2013)]

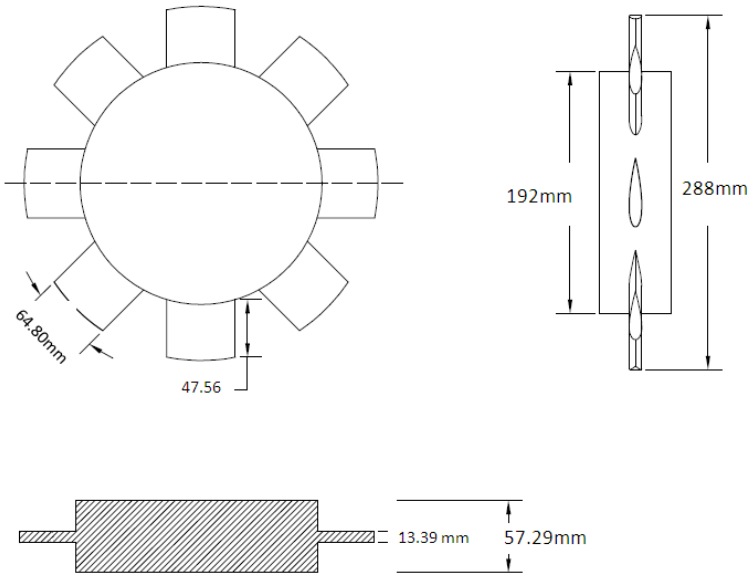

Figure 4.13: Experimental turbine geometry. [Source: Benslimane (2013)]

4.4.3 Results

4.4.3.1 Type of waves

Regular waves are run: (a) $H = 0.5\,m$, $T = 3.5\,s$; (b) $H = 1\,m$, $T = 6\,s$; (c) $H = 1.5\,m$, $T = 7\,s$ and (d) $H = 2\,m$, $T = 8\,s$. The *Lé Mehauté* approximation for the applicability region of the different wave theories, Le Méhauté (1976), has been applied to the wave conditions run in this thesis. The smaller wave conditions ($H = 0.5$, 1 m) are classified as Stokes 2^{nd} order waves. The bigger waves tested ($H = 1.5$, and 2 m) fall within the Stokes 3^{rd} order theory. A comparison with the validation tests presented in Section 4.2 is made in table 4.3 to check the validity of Fluent® for these types of waves.

H(m)	T (s)	h (m)	Type of wave
0.052	3	0.4	Stokes 2^{nd} order
0.113	1.5	0.4	Stokes 3^{rd} order
0.5	3.5	5	Stokes 2^{nd} order
1	6	5	Stokes 2^{nd} order
1.5	7	5	Stokes 3^{rd} order
2	8	5	Stokes 3^{rd} order

Table 4.3: Wave theories applicable for each type of wave conditions tested. Obtained from the *Lé Mehauté* diagram, Le Méhauté (1976).

The tests used to validate the numerical flume (see Section 4.2) are located in the region of Stokes 2^{nd} order, and Stokes 3^{rd} order waves. As the validation was satisfactory, it is concluded that Fluent® models accurately these types of waves.

4.4.3.2 Surface elevation, wave spectra, pressure drop and air velocity.

Figure 4.14 depicts the gauge distribution inside the flume. Figure 4.15 presents the surface elevation time series in the flume and inside the OWC for the different tests. Although data from at least 5 waves were recorded in each case, the results

are plotted for the first 25 s for comparison purposes. Here, data were recorded every 0.1 s. Figure 4.16 shows the surface elevation time series obtained at each sensor over the complete simulation time for the case $H = 1$m, $T = 6$s, in order to provide an overview of the differences between sensor measurements. The wave generator produces a regular pattern of waves and no second–order effects are discernible.

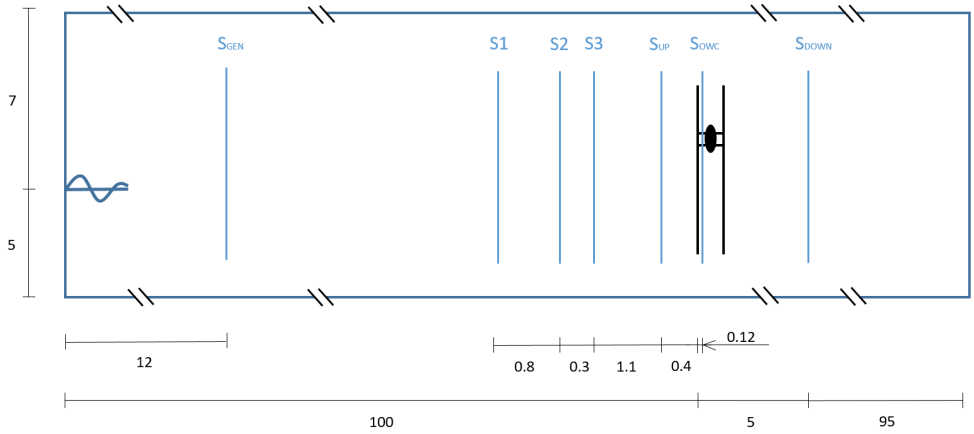

Figure 4.14: Numerical gauge scheme. Units in metres.

The water surface elevation time series measured at gauges $S1$, $S2$ and $S3$ are used for the calculation of the complex reflection coefficient modulus and phase, and the incident wave separation. Incident and reflected wave trains are separated by applying a method described by Baquerizo (1995), based on linear wave theory. The approach involves the three–gauge method proposed by Mansard & Funke (1987), which resolves the mathematical inconsistency of minimizing a complex variable. Accounting for the specific flume set–up, the modulus of the reflection coefficient (K_R) is calculated, see table 4.4. Values of K_R range from ~ 0.2 to 0.4 for the highest period. Moreover, the ratio between external OWC diameter and wavelength is $D/L = 0.02 << 0.2$, revealing that back–scattered waves could have a minor effect on higher kh, Paixão Conde *et al.* (2011), explaining the lower reflection values.

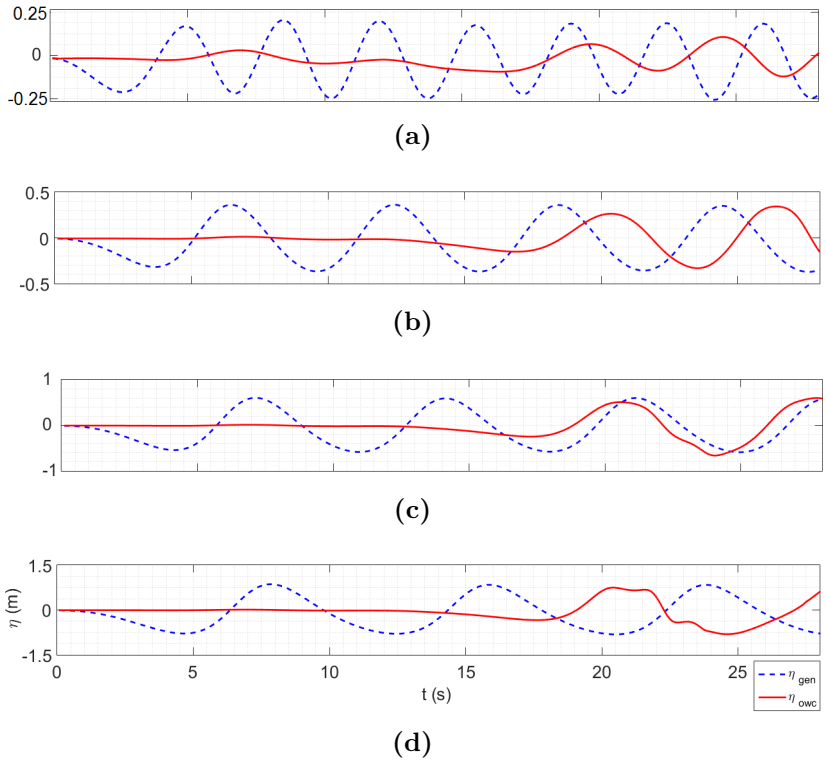

Figure 4.15: Surface elevation time series at locations (leeward of the paddle and inside the OWC): (a) $H = 0.5\,m$, $T = 3.5\,s$; (b) $H = 1\,m$, $T = 6\,s$; (c) $H = 1.5\,m$, $T = 7\,s$; and (d) $H = 2\,m$, $T = 8\,s$.

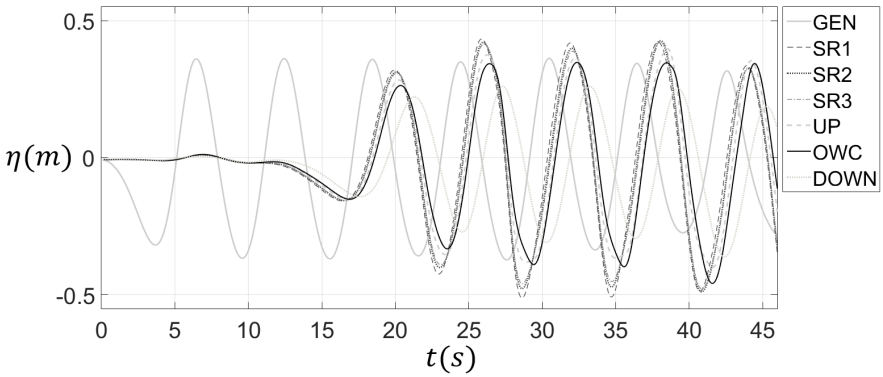

Figure 4.16: Surface elevation time series: $H = 1\,m$, $T = 6\,s$, all sensors.

The spectral density can be calculated for a given wave record as:

$$S_f = \frac{A^2/2}{\delta f} \tag{4.14}$$

where A_0 is the wave amplitude for each frequency interval δf. Figures 4.17 and 4.18 present the energy spectra obtained for incident waves on the seaward side of the OWC and inside the converter. The overall wave energy can be estimated from the area under the spectra as:

$$E = \rho_w g \int S_f(f) df \,. \tag{4.15}$$

Energy impinging on the OWC and the available energy inside the device due to the water column oscillation can be calculated in the same way. The results are summarized in table 4.4 in terms of kh, where k is the wave number and h is the water depth. E represents the energy of the impinging waves outside the OWC. Available wave energy inside the OWC (E_{OWC}) equals the energy on the seaward side of the device for the two highest periods, rendering a ratio of almost 100 %. This is in accordance with the higher water elevations reached inside the chamber for these cases, see figure 4.15.

$Test$	kh	K_R	$E(MJ/m^2)$	$E_{owc}(MJ/m^2)$	$E_{owc}/E(\%)$
$H = 0.5\,m; T = 3.5\,s$	1.74	0.30	0.41	0.2	48.2
$H = 1\,m; T = 6\,s$	0.83	0.20	2.44	1.93	79.2
$H = 1.5\,m; T = 7\,s$	0.69	0.16	3.74	3.57	95.5
$H = 2\,m; T = 8\,s$	0.59	0.40	3.21	3.21	100.0

Table 4.4: Wave energy impinging on the OWC and inside the converter.

It must be recalled that the ratio only represents the availability of the resource inside the OWC with reference to the resource outside for incoming waves during a time interval, *i.e.* the amount of energy to be seized by the OWC over that complete interval, which could be expected to be essentially 100 % for the highest period. Moreover, this value is only feasible because this is a 2D simulation. In a 3D case, without an infinite-width OWC a 100 % energy capture would never arise. Obviously, the expected OWC performance would be lower than the calculated ratio, due to the delay between the external oscillation and the water surface displacement inside the chamber, as can be observed in figure 4.15. In fact, the theoretical solutions of the radiation–diffraction problem for the OWC provide values of surface elevation, amplitude, and phase for a given configuration.

Therefore, the numerical simulations provide a first visualization of the wave interaction with the device in an appropriate way.

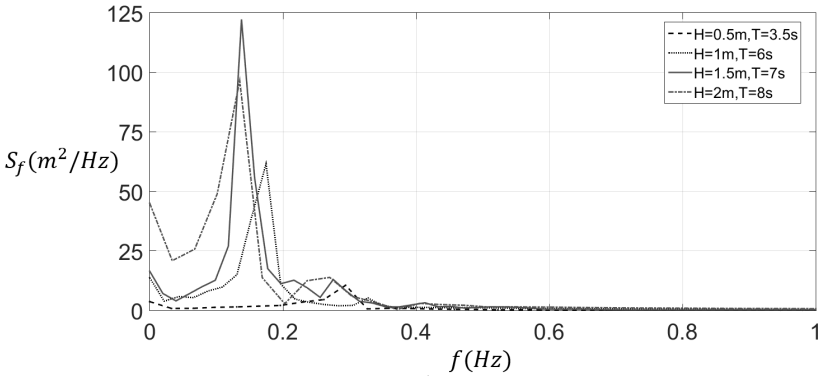

Figure 4.17: Wave spectra: (a) $H = 0.5\,m$, $T = 3.5\,s$; (b) $H = 1\,m$, $T = 6\,s$; (c) $H = 1.5\,m$, $T = 7\,s$, and (d) $H = 2\,m$, $T = 8\,s$.

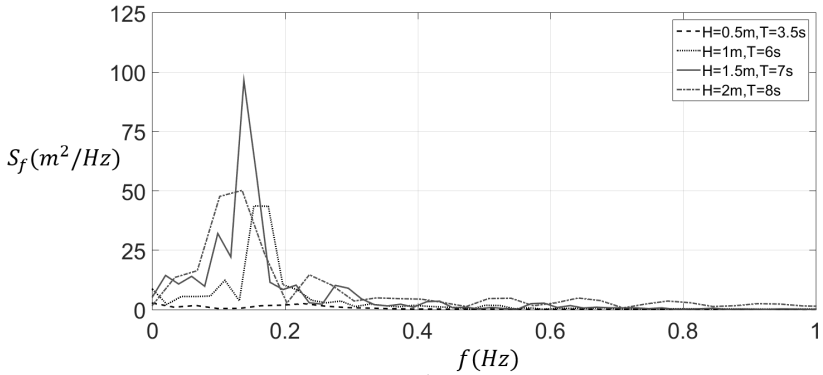

Figure 4.18: Wave spectra inside the OWC: (a) $H = 0.5\,m$, $T = 3.5\,s$; (b) $H = 1\,m$, $T = 6\,s$; (c) $H = 1.5\,m$, $T = 7\,s$, and (d) $H = 2\,m$, $T = 8\,s$.

Figure 4.19 depicts pressure drop and vertical velocity inside the OWC chamber, which can be seen to exhibit the same pattern. The pressure drop increases with wave height and period, corresponding to the increase in velocity of surface oscillation.

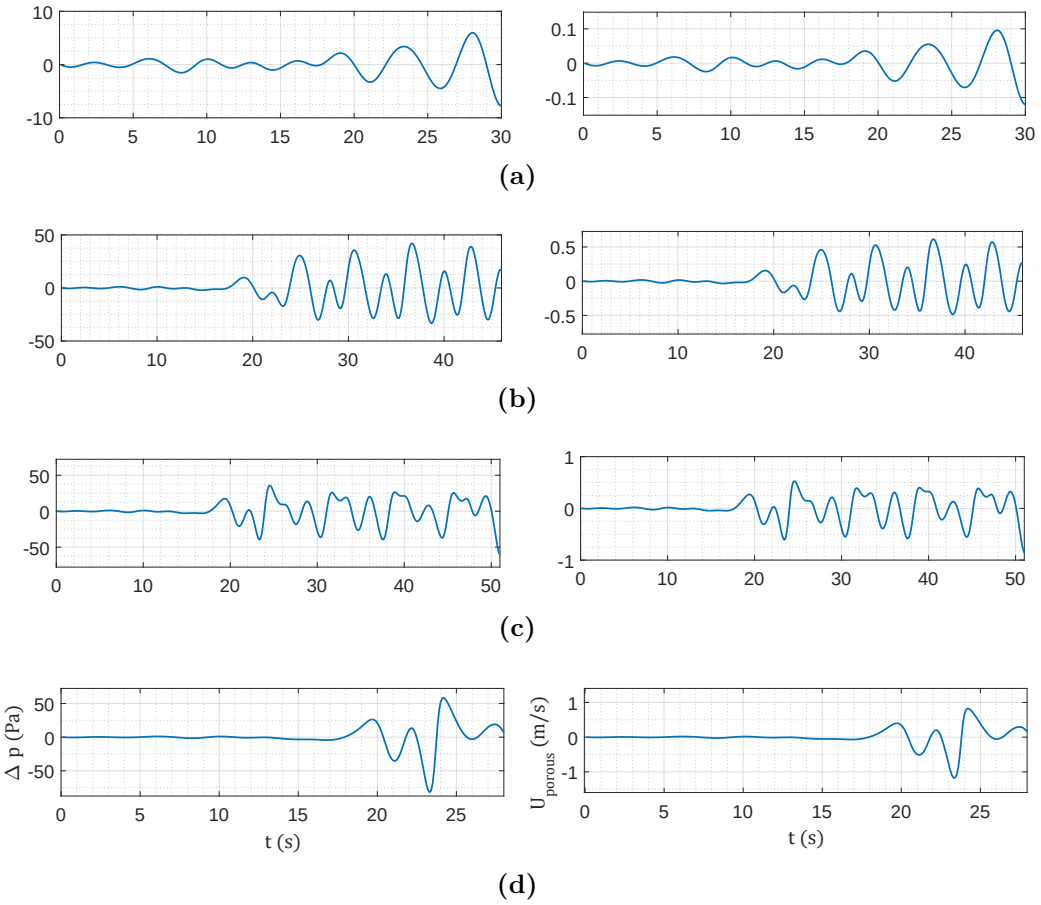

Figure 4.19: Pressure drop time series inside the OWC chamber (left) and flow velocity time series at the inlet of the porous region (right): (a) $H = 0.5\,m$, $T = 3.5\,s$; (b) $H = 1\,m$, $T = 6\,s$; (c) $H = 1.5\,m$, $T = 7\,s$, and (d) $H = 2\,m$, $T = 8\,s$.

4.4.3.3 Pressure drop vs. air flow through the converter

Figure 4.20 shows the pressure drop versus volumetric flow rate for the cases considered. The pressure drop is linear with the air flow through the porous zone. The pressure range is consistent with the expected values: higher values of pressure and flow rate correspond to longer wavelength and period of incoming waves. It is important to note that linearity is conserved even for the larger waves considered. The central point of the Δp - Q_{owc} graph is zero because there is no initial resistance imposed on the ADM. Moreover, friction is not considered in these tests, which could otherwise cause the central point of the plots to deviate.

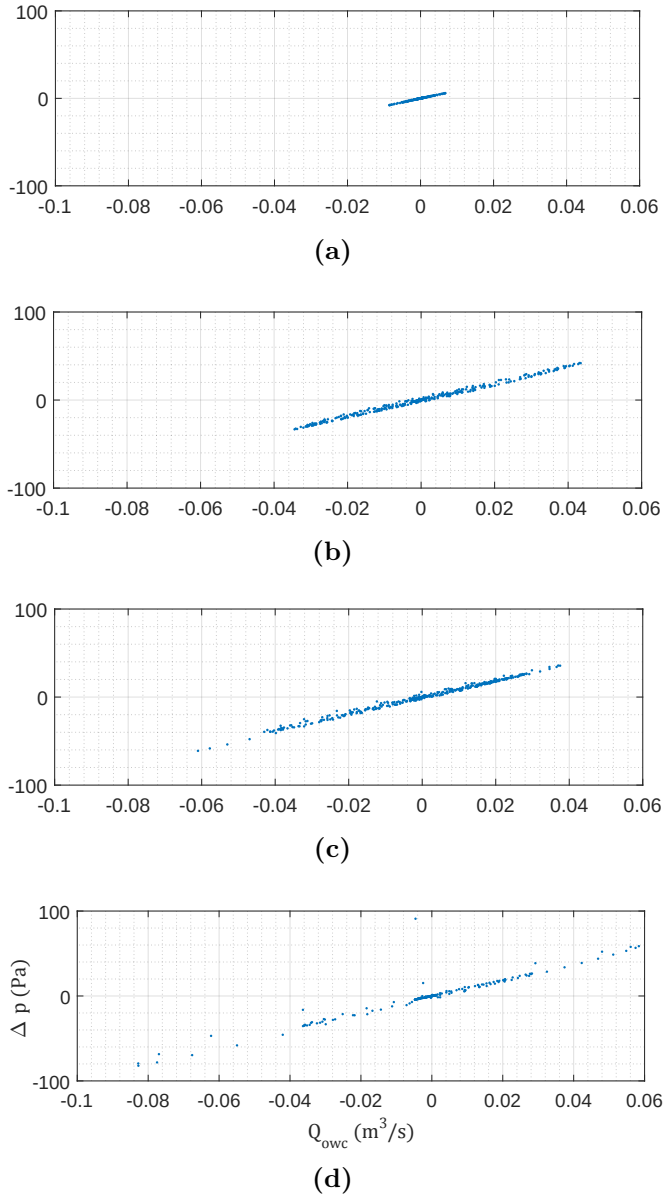

Figure 4.20: Pressure drop Δp as a function of volumetric flow rate Q_{owc}: (a) $H = 0.5\,m$, $T = 3.5\,s$; (b) $H = 1\,m$, $T = 6\,s$; (c) $H = 1.5\,m$, $T = 7\,s$, and (d) $H = 2\,m$, $T = 8\,s$.

4.4.3.4 Turbine performance simulation by the ADM

Figure 4.22 compares the pressure drop-air flow relationships obtained for the experimental Wells turbine and the ADM. To carry out the comparison between the experimental and ADM results, initial resistance effects are neglected, and the

initial experimental line is translated taking into account the minimum velocity necessary to allow for rotation of the Wells turbine. This velocity is set to zero ($v(p = 0) = 0$) to simulate the ADM zero-resistance performance, and the line is translated accordingly. The result is the superposition of the experimental and numerical results, and so the ADM operation in this case is validated, provided dynamic effects are neglected. Here, the numerical model reproduces the linear response of the turbine in terms of pressure and air flow according to the experimental data.

Reasons for the discrepancies observed between the experimental turbine and the ADM model results are most likely to be related to mechanical friction, dynamic drag, and start up characteristics, or the *crawling* phenomenon. From a general point of view, the air passing through the turbine has to overcome a mechanical and frictional resistance, and so an increment in air flow (or if preferred, in pressure) will occur, because a fraction of the flow energy has to be used to overcome the permanent resistance. This leads to the parallelism between the Δp-Q_{owc} plots in both experimental and numerical models. As the ADM is not designed to reproduce dynamic effects, this reaction cannot be taken into account in the numerical model, *i.e.* the ADM offers no resistance to air flow. In fact, this is why the ADM Δp-Q_{owc} plots are always centred in $(Q_{owc} = 0, \Delta p = 0)$, a condition that might not be applicable to actual Wells turbines.

In addition, turbine *crawling* is generally observed in Wells turbines, and occurs when the turbine is not able to achieve the operational velocity by itself starting from the idle state. Turbine *crawling* depends on two main factors:

- the turbine *solidity* σ.
- the relationship between the *hub-to-tip ratio* ($h = R_h/R_t$) and the solidity.

Following figure 4.21, and noting that the turbine hub-to-tip ratio is $h = 0.67$ and the the turbine solidity is $\sigma = 0.55$, the experimental turbine is on the threshold of not being self starting. Obviously, that effect is not represented in the porous zone performance.

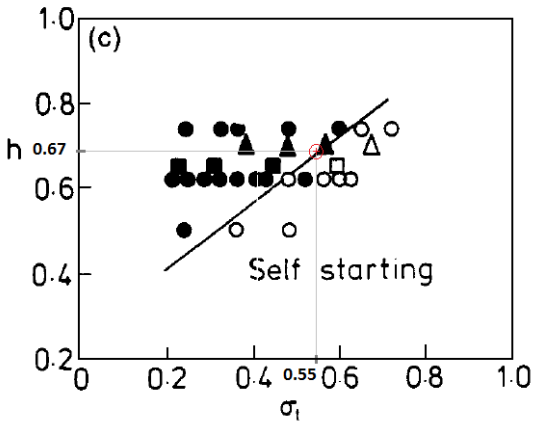

Figure 4.21: Relative effects of hub-to-tip ratio and solidity on the self–start condition of the turbine, Raghunathan (1995)

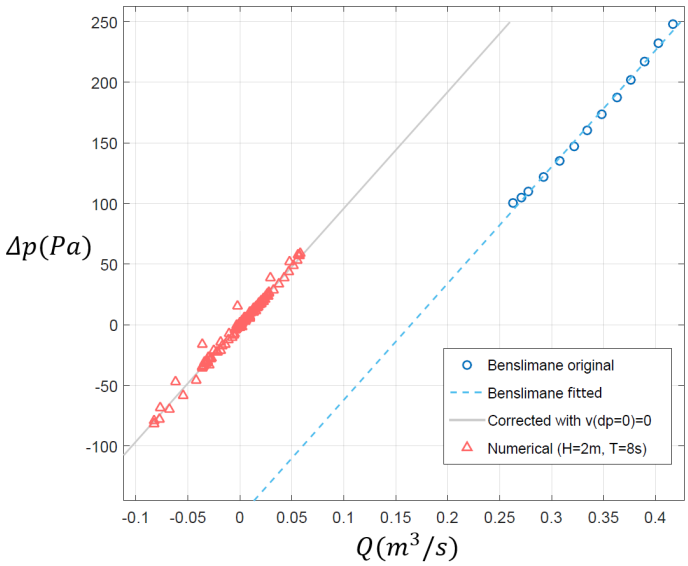

Figure 4.22: Comparison between physical tunnel experiments and numerical predictions of pressure drop versus volumetric flow rate. Note that the corrected line is the Benslimane fitted line translated to remove the offset.

4.4.4 Discussion of dimensions of flume: reflection effects

In order to check when reflection might be a problem in the numerical flume (remember that a dissipation zone was not located at the end of the flume in this case), a sensitivity analysis of the length of the flume is now undertaken. For that

purpose, a flume longer than the flume used throughout this thesis is tested (*e.g.* 400 m long). The other characteristics of the flume and run conditions are exactly the same as those presented in previous chapters.

Figure 4.23 presents the x–t plot for the 400 m–long flume. The slope of the plot shows the wave celerity at each point. In this case, a wave celerity of around 7 m/s is observed, which matches with the theoretical approximation. The first wave will take around 60 s to reach the end of the flume. A reflected wave is observed in the upper right corner of figure 4.23. The reflected wave presents a slightly lower velocity, around 6 m/s. The reflected wave will take around 70 s to reach the paddle in its way back. That means that the reflection would take a total of 95 s to reach the middle of the flume (where the OWC would hypothetically located). In a 200 m–long flume, if the OWC is located in the middle of it, the reflected wave would take around 50 s to reach the middle of the flume. Thus, any data recorded before $t = 50$ s can be considered as reflection–free for the wave conditions considered in this case. Figure 4.24 presents the same flume with an OWC structure located in the middle of the flume. This is done in order to check the effects of the location of a device in the flume and in possible reflection effects presented because of the device itself.

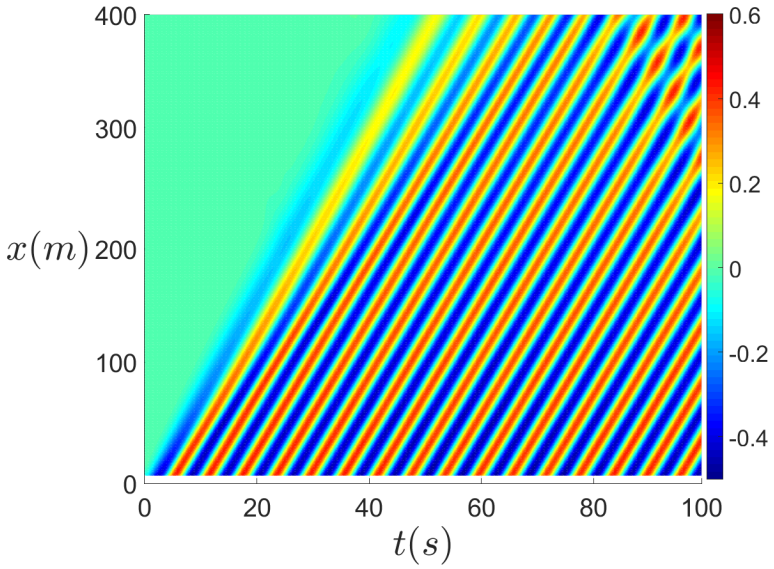

Figure 4.23: x–t water elevation plot for the 400 m–long flume. $H = 1$ m, $T = 6$ s.

The wave height after the OWC is clearly smaller that the surface elevation in the

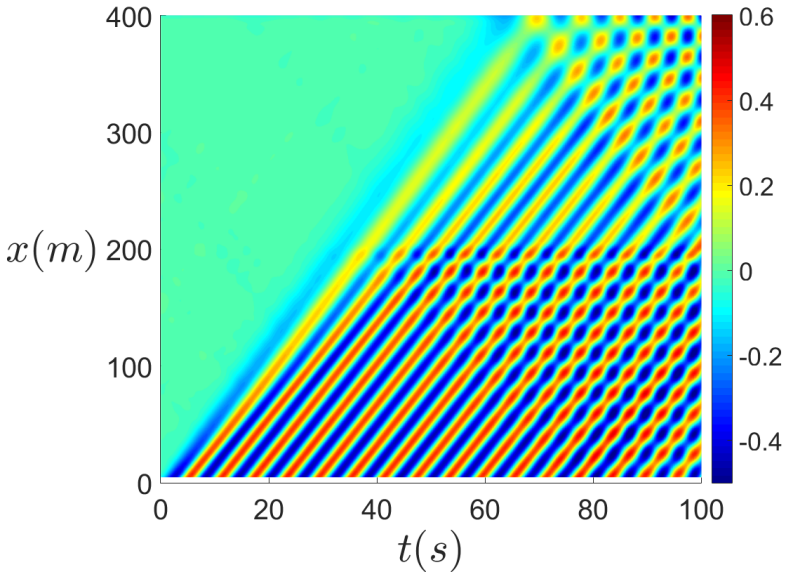

Figure 4.24: *x–t* water elevation plot for the 400 m–long flume. $H = 1$ m, $T = 6$ s. OWC located at $x = 200$ m.

empty flume, as shown in figure 4.23. Dissipative effects caused by the OWC are clearly visible in this comparison, presenting a reduction in the surface elevation after the device of around 3 times when there is not an OWC. A reflected wave is easily observed in figure 4.24, starting at $x = 200$ m, where the OWC is placed. The same reflected wave at the end of the flume is observed in both cases, but the magnitude of the reflected wave in the case where the OWC is present is around half of the surface elevation when the flume is empty. The velocity of the reflected wave caused by the OWC is around 5 m/s, slower that the celerity of the reflected wave at the end of the flume, which is similar to that in figure 4.23. This phenomenon is probably caused by the loss of kinetic energy in the wave when interacting with the OWC.

Figures 4.25 and 4.26 show the same results as figures 4.23 and 4.24 in 3D. In the former, time is represented in the x–axis, while the length of the flume is represented in the y–axis.

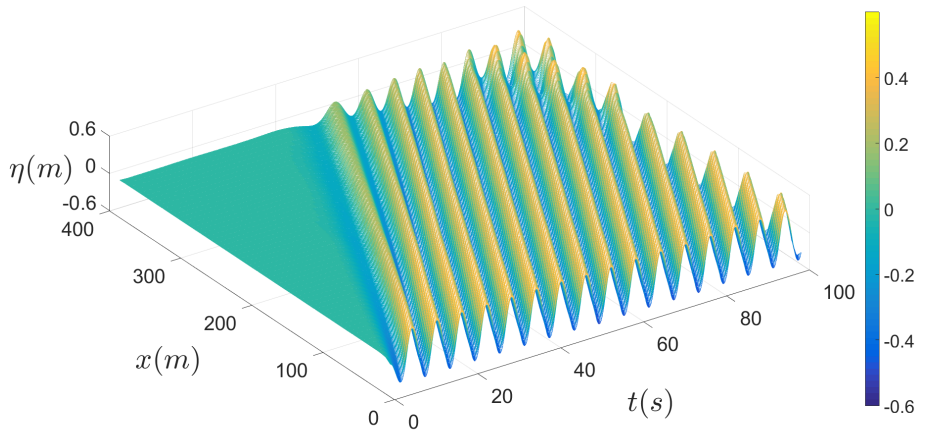

Figure 4.25: Surface elevation plot for the 400 m–long flume. $H = 1$ m, $T = 6$ s.

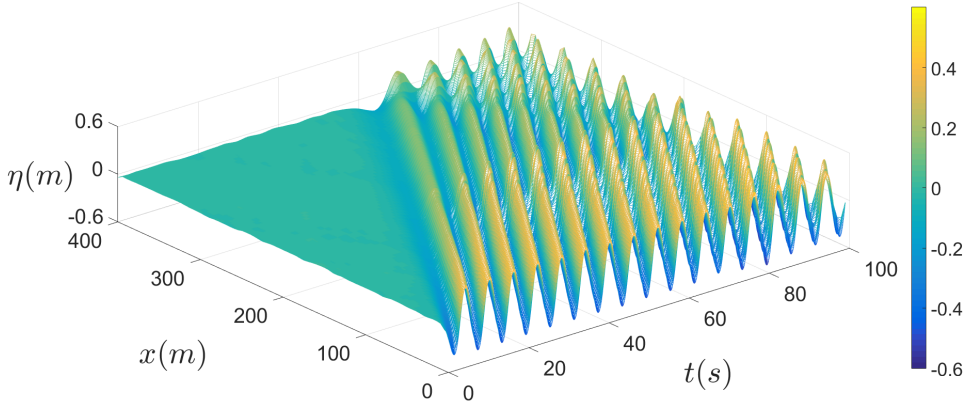

Figure 4.26: Surface elevation plot for the 400 m–long flume. $H = 1$ m, $T = 6$ s. OWC located at $x = 200$ m.

T (s)	L (m)	c (m/s)
3.5	17.9	5.1
6	38.1	6.4
7	45.6	6.5
8	53.1	6.6

Table 4.5: Test parameters: wave period (T), wave length (L), and wave celerity (c).

Table 4.5 presents the wave celerities for the set of waves analysed in the previous case study. The larger the period, the faster the wave speed. Then, for periods greater than $T = 6\,\text{s}$, the non–reflection window would be smaller, and so the data obtained at about $t = 59\,\text{s}$ should be studied carefully because it is the threshold at which reflection begins to contaminate the results.

By applying *Froude* scaling, the equivalence to a geometrically similar flume can be done. The period of the equivalent model can be defined as: $T_R = \sqrt{L_R}$, where T_R is the ratio between the initial wave period and that in the equivalent flume, and L_R is the ratio of characteristic lengths. Equivalence of the analysed tests can be achieved using the *Froude* relations. By fixing one parameter (for example, depth), the equivalent wave conditions, and device diameter can be obtained. Equivalent geometries to that of a flume 5 m depth, with an OWC 0.3 m diameter, and wave conditions $H = 1\,\text{m}$, $T = 6\,\text{s}$, are summarised in table 4.6.

h (m)	T (s)	H (m)	D (m)
2.5	4.24	0.5	0.15
5	6	1	0.3
10	8.48	2	0.6
15	10.4	3	0.9
50	18.9	10	3

Table 4.6: Equivalent water depth (h), wave conditions (T, H), and OWC diameter (D). *Froude* equivalence.

For those characteristics presented in table 4.6, the results should be equivalent to those shown in figures 4.23 to 4.26.

4.5 Case study: OWC with linear turbine in wave flume inserting seabed morphology. Dry air conditions.

The same model presented in the previous section is now tested for different seabed conditions. The bottom of the numerical flume has been modified according to the conditions at Playa Granada (Spain). The seabed forms are reproduced with the morphodynamic model XBeach–G® for a series of characteristic sea states. These bedforms are used as input bed geometries in Fluent® and the results compared with the flat seabed results presented in previous sections to analyse the effects of changes in bed level on the OWC performance. The results from this section are already published in the paper by Medina-Lopez *et al.* (2017–II). A summary is presented here.

4.5.1 Wave case selection

The wave conditions cases were selected based on a 58–year series of hourly data, corresponding to SIMAR point number 2041080 and provided by Puertos del Estado (2016). 11 values (one every 0.5 m) of significant wave height in deep–water (H_0) between the minimum and the maximum of the whole register were considered. For each H_0, three associated peak wave periods (T_p) were tested (Table 4.7): the minimum (T_{min}), the most frequent (T_{freq}), and the maximum (T_{max}).

4.5.2 Seabed evolution with XBeach–G®

The process-based model XBeach–G® is an extension of the XBeach® model that incorporates: (1) a non–hydrostatic pressure correction term that allows wave predictions using an explicit solver; (2) a groundwater model that allows infiltration and exfiltration; and (3) the computation of bed load transport, including the effects of groundwater ventilation and flow acceleration forces, for estimating bed level changes (McCall *et al.* , 2014, 2015).

A 120 m–long flat bottom with a vertical boundary at the landward side, was simulated as the initial profile for each case. The input wave conditions were

XBeach-G seabed profile	$H_0\,(m)$	$T_{min}\,(s)$ [A]	$T_{freq}\,(s)$ [B]	$T_{max}\,(s)$ [C]
P1	0.5	2	4	13.2
P2	1	2.6	4.8	13.3
P3	1.5	4.2	5.8	11.8
P4	2	5.2	6.9	11.9
P5	2.5	6.4	7.6	12.2
P6	3	7.1	7.7	10.7
P7	3.5	7.7	8.4	10.7
P8	4	8.4	8.7	9.6
P9	4.5	9.6	9.6	9.7
P10	5	9.6	9.6	9.6

Table 4.7: Sea states modelled with XBeach–G® to simulate morphological changes of the seabed in front of the reflective boundary.

obtained from the Delft3D-WAVE® model, which allowed propagation of the deep-water sea states (see table 4.7) towards the nearshore. In addition, the Delft3D®–model was calibrated through comparison with data collected by two Acoustic Doppler Current Profilers (Bergillos *et al.* , 2016–I). The value of sediment friction factor used for the simulations was 0.03°, which was found to be optimum during the calibration of the XBeach–G® for the study site (Bergillos *et al.* , 2016–II). The reflective boundary located at the landward limit of the computational domain was set as a non–erodible object. I each case, the final bed level obtained with XBeach–G® was used as input for the Fluent® model, as detailed in the following section.

4.5.3 Wave generation and OWC simulation in Fluent®

The bed morphology previously generated with XBeach–G® was upgraded into a finite element domain to be used in a 2D flume designed in Fluent®, including the OWC structure adjacent to the vertical breakwater. The flume has a length of 120 m and a height of 12 m, with an initial water depth of 5 m. The OWC was located at the right end of the mesh, with the Wells turbine represented by means of an ADM, according to Section 4.3. The mesh conditions are the same as those presented in Section 4.4. The gauge scheme in this case is as shown in figure 4.27.

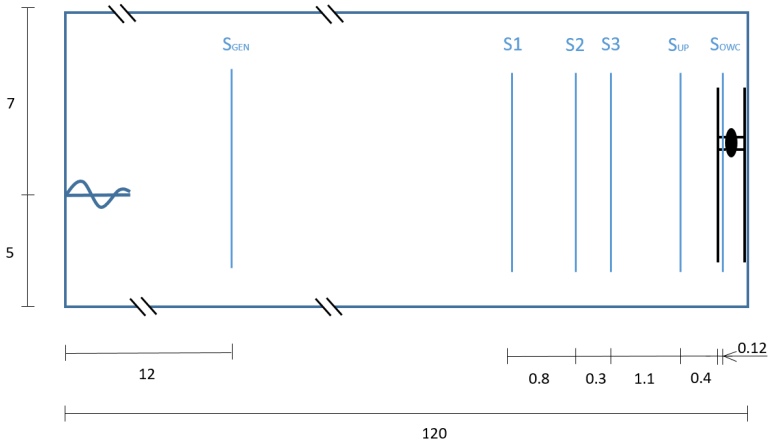

Figure 4.27: Schema of gauges located in the numerical flume. Units in metres.

4.5.4 Results

4.5.4.1 Seabed forms

Table 4.8 shows the mean amplitude ($\overline{\delta}$) and length ($\overline{\lambda}$) of the bedform with the highest unit volume (calculated by the trapezoidal rule) in each case. It is observed that the bedform dimensions are generally related to the combination of wave height and period (wavelength), so that greater values of wave height and period generate higher bed level changes. The mean amplitudes appear to be directly influenced by the wave height; whereas they increase with wave period (wavelength) up to values of around 9.6 s (145 m) and decrease for higher values. The bedform lengths are longer for higher wave heights and periods (wavelengths), but they seem to be more closely related to wave period (wavelength) since an almost linear trend is observed between bedform length and wave period (wavelength).

These patterns are presented in figure 4.28, which depicts the bed level in the proximity of the reflective boundary for eight representative cases selected to study the influence of seabed morphology on the OWC performance. The higher bedform amplitude (0.471 m) is generated by case 10B, which is the one with highest wave height (5 m), but not the highest wave period and wavelength (9.6 s and 143.9 m, respectively). On the other hand, longer bedform lengths are obtained for greater values of wave period and length in most of the cases, the only exception being case P2C. Values of lengths and amplitudes of the generated bedforms for these

Seabed profile	H (m)	T (s)	L (m)	$\overline{\delta}$ (m)	$\overline{\lambda}$ (m)
P1A	0.5	2	6.25	–	–
P1B	0.5	4	24.98	–	–
P1C	0.5	13.2	272.04	0.004	25
P2A	1	2.6	10.55	–	–
P2B	1	4.8	35.97	–	–
P2C	1	13.3	276.18	0.258	27.5
P3A	1.5	4.2	27.54	–	–
P3B	1.5	5.8	52.52	0.003	12.4
P3C	1.5	11.8	217.4	0.279	42.3
P4A	2	5.2	42.22	0.004	19.9
P4B	2	6.9	74.33	0.159	22.7
P4C	2	11.9	221.1	0.294	42.5
P5A	2.5	6.4	63.95	0.132	22.4
P5B	2.5	7.6	90.18	0.356	25.1
P5C	2.5	12.2	232.39	0.308	30.2
P6A	3	7.1	78.71	0.287	22.6
P6B	3	7.7	92.57	0.368	24.9
P6C	3	10.7	178.75	0.409	32.4
P7A	3.5	7.7	92.57	0.387	25.1
P7B	3.5	8.4	110.17	0.379	27.5
P7C	3.5	10.7	178.75	0.396	35
P8A	4	8.4	110.17	0.377	29.9
P8B	4	8.7	118.18	0.442	27.6
P8C	4	9.6	143.89	0.386	29.8
P9A	4.5	9.6	143.89	0.425	32.5
P9B	4.5	9.6	143.89	0.425	32.5
P9C	4.5	9.7	146.9	0.425	32.6
P10A	5	9.6	143.89	0.471	34.9
P10B	5	9.6	143.89	0.471	34.9
P10C	5	9.6	143.89	0.471	34.9

Table 4.8: Bedform mean amplitude ($\overline{\delta}$) and mean wavelength ($\overline{\lambda}$) for each case.

cases are in the ranges of [0.159 m, 0.471 m] and [22.7 m, 42.3 m], respectively. The influence of these forms on the OWC performance is detailed in the following sections.

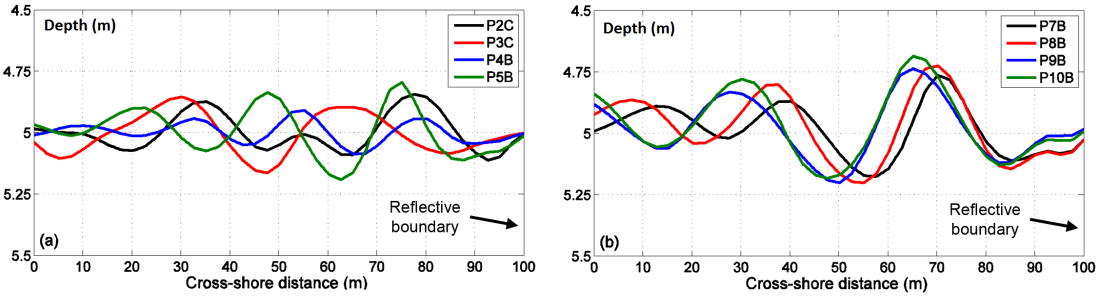

Figure 4.28: Final bed levels obtained with the XBeach–G® model: (a) Cases P2C, P3C, P4B and P5B, (b) P7B, P8B, P9B and P10B.

4.5.4.2 Water surface elevation

Figure 4.29 depicts the surface elevation inside the OWC and at the generation zone for eight test cases, both flat bottom and evolved seabed. There are similarities for the smaller wave heights, *i.e.* cases P2C to P5B, between the flat bottom and evolved seabed tests, both for generated waves and the waves inside the OWC. Conversely, for cases P7B to P10B, significant differences in the surface elevation inside the OWC are observed between the flat bottom and changed seabed scenarios. The amplitude of the free surface elevation is different in both cases, eventually showing a slight phase shift. This analysis shows that changes in bedforms affect the amplitude and the phase of the water surface inside the OWC. The larger the wave height, the more significant the effect on the free surface elevation.

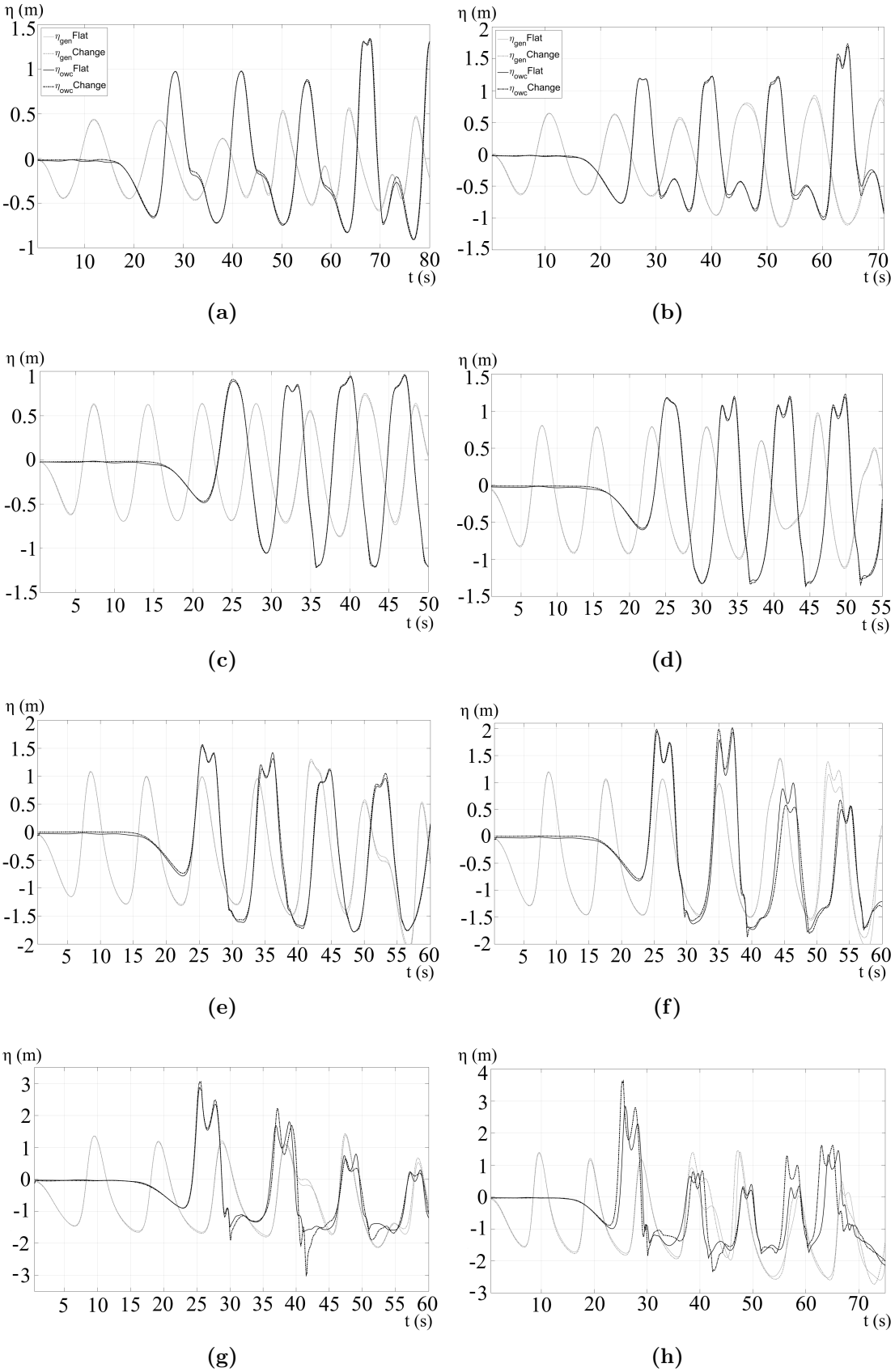

Figure 4.29: Surface elevation at the generation gauge and inside OWC for flat bed and changed seabed tests. (a) P2C; (b) P3C; (c) P4B; (d) P5B; (e) P7B; (f) P8B; (g) P9B; (h) P10B.

Moreover, figure 4.30 shows the hydrodynamic efficiency in energy extraction (ϵ) as defined by Sarmento *et al.* (1990). Efficiency is determined as the ratio between pneumatic power available to the turbine (P) and wave energy flux (f_E) averaged over a wave cycle (P/f_E). From the perspective of bed evolution, higher efficiency values are obtained for the smoothest bedforms, *i.e.* tests with intermediate kh values (where h is the initial wave depth), such as case P3C ($H = 1.5$ m, $T = 11.8$ s). It should be noted that the efficiency values are usually lower for the case with evolved seabed than for the flat seabed, with more noticeable differences occurring at the lower values of kh (below $kh = 0.5$), corresponding to wave periods in excess of 8 s. The mean efficiency in the flat bed cases is about 19%, whereas for the evolved seabed cases the mean efficiency is about 15%. These values match results presented by Sarmento *et al.* (1990), where the hydrodynamic efficiencies were close to 18% when optimal phase control was applied. The present results show that for a real bedform, OWC efficiency values decrease more than 4%.

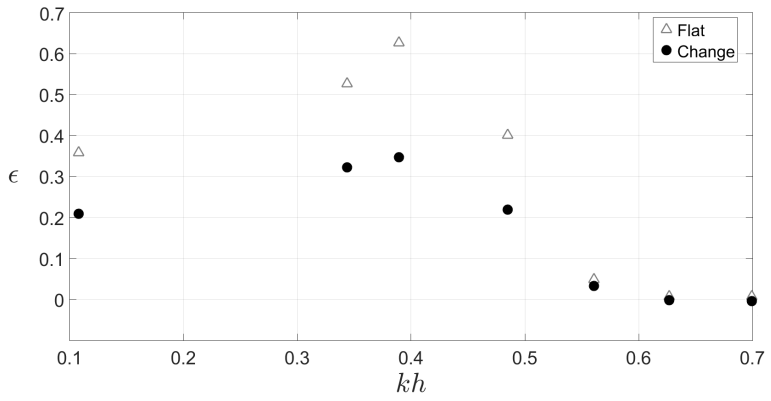

Figure 4.30: Efficiency of energy extraction vs kh.

The generated wave alters slightly for the last cases (P10B, P9B and P8B). This effect might be caused by the larger wave height values, along with possible reflection effects at the leeward end of the flume. High waves combined with moderate depths, are reduced by seabed forms, tend to shoal. This leads to an increase in crest height with respect to wave trough.

Figure 4.31a shows the velocity contours and velocity vectors (white dots) for case P7B. Although the velocity magnitude is quite similar for the flat bottom and evolved morphology tests, the near–bed velocity vectors are very different. In the

flat bed case, the velocity vectors are parallel to the bed. When bedforms are present, the near–bed velocity vectors are sinusoidal, following a pattern opposite to the shape of the bedform, *e.g.* when the bedform is concave, the streamline over it is convex. Figure 4.31b presents velocity vectors coloured by stream function. Despite the similitude in the velocity field between the flat and evolved seabed scenarios, the mass transport along the flume with bedforms present is nearly twice than over the flat bed. Moreover, the transport–related streamline patterns are different, indicative of the change in the energy distribution generated by the bedforms.

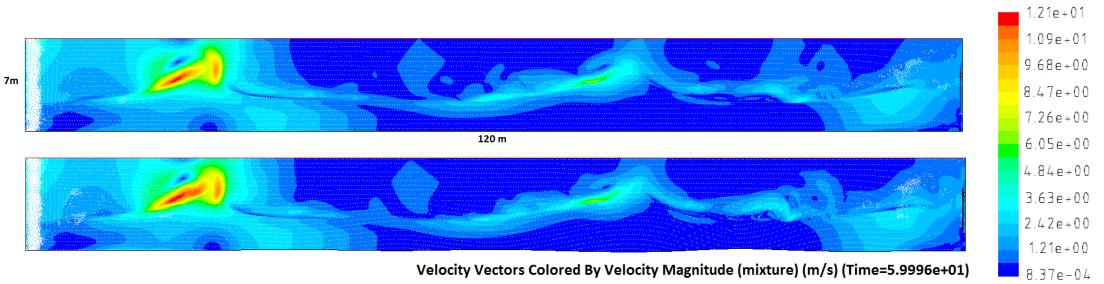

(a)

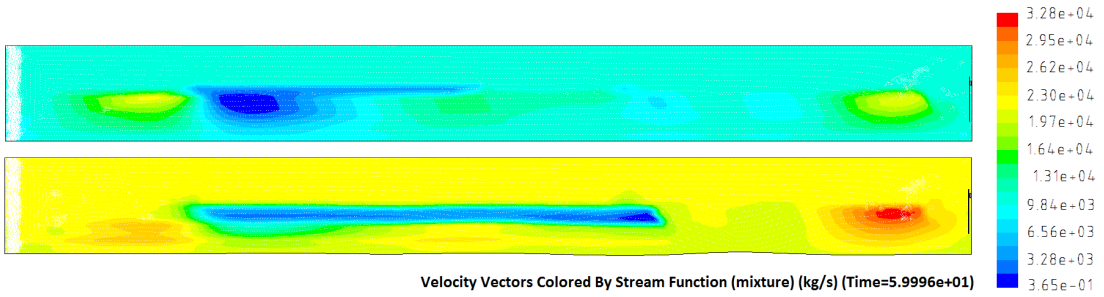

(b)

Figure 4.31: Velocity vectors coloured by velocity magnitude (m/s) (a) and stream function (kg/s) (b). Flat bottom (upper panel) and evolved seabed (bottom panel) for case P7B at the end of the simulation time ($t = 60\,s$).

4.5.4.3 Pressure drop inside OWC as a function of air flow

In figure 4.32, case P3C exhibits a very representative airflow amplitude in the OWC chamber in comparison with its wave height (1.5 m). This case corresponds to $kh = 0.39$, the largest bedform wavelength. The larger the bedform wavelength, the bigger the airflow inside the OWC. Cases P10B and P7B also have very

large airflows, which correspond to $kh = 0.49$ and $kh = 0.56$, respectively. The maximum in the bedform amplitude occurs in these cases too. The larger the bedform amplitude, the bigger the airflow inside the OWC. On the other hand, case P8B produces a bedform amplitude of 0.442 m, one of the highest considered, but a bedform wavelength of 27.6 m, which gives a moderate airflow amplitude. Finally, case P4B exhibits both moderate bedform amplitude and wavelength, and presents a limited pressure drop–airflow amplitude, very close to the value obtained for case P2C, even when the wave height is twice that of case P2C in case P4B. Then, the bedforms affect the pressure drop–airflow relationship inside the OWC, e.g., they change the slope of the $\Delta p - Q$ curve and the range. Moreover, the maximum change in the conditions inside the OWC depends on both the maximum bedform wavelength and maximum bedform amplitude, which implies that these changes depend on the bedform unit volume, which is an integrated parameter, instead of on single geometrical parameters.

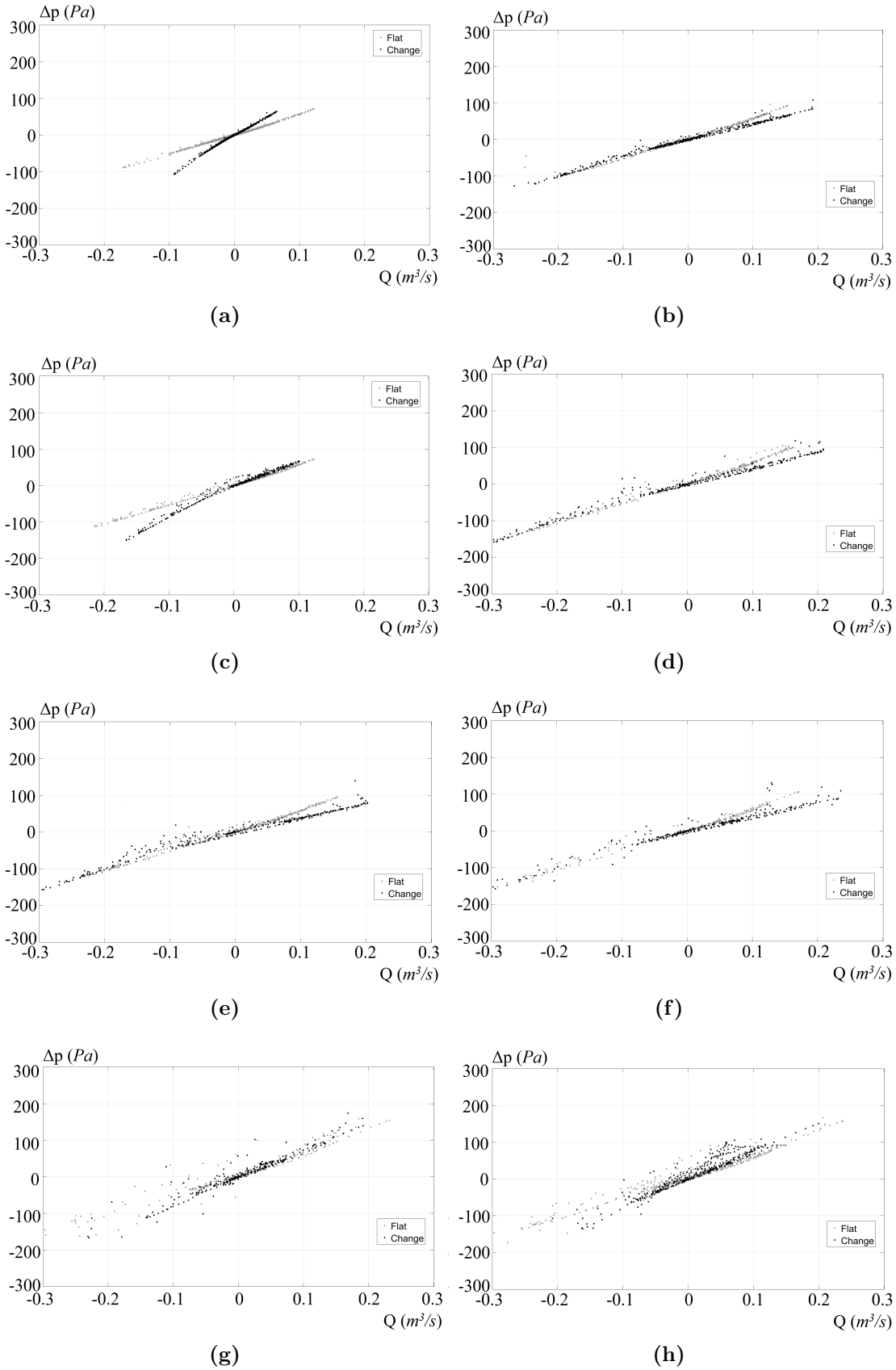

Figure 4.32: Pressure drop as a function of air flow inside OWC for flat bed and changed seabed. Cases: (a) P2C; (b) P3C; (c) P4B; (d) P5B; (e) P7B; (f) P8B; (g) P9; (h) P10B.

4.5.4.4 Main findings

The highest hydrodynamic efficiency, calculated according to Sarmento *et al.* (1990), is attained in tests with intermediate kh values, such as P3C ($H = 1.5$ m, $T = 11.8$ s). The efficiency values are invariably lower for the cases with evolved seabed than those with a flat bed, with more noticeable differences occurring for wave periods over 8 s. The flat cases present a mean efficiency (19%) similar to that presented by Sarmento *et al.* (1990) (18%), whereas the mean efficiency for the evolved bedform cases decreases to 15%.

Although the wave velocity magnitude is essentially the same for the flat and seabed forms, the streamline patterns do change. While the streamlines are flat and parallel to the surface over flat beds, a radial pattern centred in the troughs of bedforms occur over the evolved bed. Despite the lack of change in the velocity magnitude, the mass transport along the flume over the evolved seabed is nearly twice the mass transport over the correspondent flat bed. Also, the transport patterns change, indicating a more extended transport along the flume direction. These factors imply that a change in the energy distribution inside the flume is caused by the bedforms.

The unit volume of the bedofrms directly affects the OWC performance. The slope of the pressure drop–air flow curve for the OWC turbine changes depending on the unit volume. However, this result might not be conclusive: the pressure drop is smaller for higher bedform unit volume, but the air flow grows. Thus, the power output may not change in magnitude, but the way the power is absorbed is altered. This fact, linked to the residual energy in the wave spectra of the flat scenarios implies that energy dissipation is induced by the seabed which is reflected in a lack of absorption by the OWC.

Changes in the $\Delta p - Q$ curve slope influence the absorption patterns of the device depending on the location and wave conditions. Therefore, the power matrix of a device will change depending on the seabed morphology.

4.6 Conclusions

This chapter presents results from a study on the performance of an off–shore OWC converter in a 2D flume, when applied to the linear response of the PTO system (representing a Wells turbine). The chapter follows the research path commenced by Medina-Lopez *et al.* (2016), which attempts to advance our knowledge of the influence of moist air on OWC energy extraction efficiency. A series of regular wave tests have been carried out, and then compared with experimental data obtained by Benslimane (2013), in order to calibrate the model.

The linear response of the turbine has been achieved through application of ADM theory. The proposed methodology provides coherent results regarding pressure drop and air flow rates through the OWC.

The *actuator disk model* theory represents effectively a turbine with linear response in terms of pressure drop and air flow rate under dry air conditions, *i.e.* a Wells turbine. A series of regular wave tests have been run in a 2D numerical flume for this purpose, and demonstrate a satisfactory response of the ADM, independent of the wave heights and periods tested.

A simplified case study is proposed. The numerical set–up provides consistent results regarding the basic principles involved in the radiation–diffraction problem and the wave–OWC interaction. The linear response of the PTO as represented by the ADM is achieved in all test cases.

Accounting for the limitation of the ADM in terms of its feasibility to represent the turbine dynamics, the porous zone parameters can be adjusted to ensure correct performance in terms of pressure drop and flow rate.

The model has been tested for more realistic conditions by modifying the seabed morphology responding to changes in wave conditions at a particular location in the south of Spain (Playa Granada). The results show a decrease in expected efficiency and a relevant modification of the OWC working conditions depending on seabed forms.

Although Fluent® software has been used herein, the methodology can be implemented through similar CFD solvers, such as OpenFOAM, COMSOL Multiphysics, or simFlow.

Chapter 5

Application of analytical and numerical models to an OWC chamber with humidity

This chapter describes the application of the analytical model developed in Chapter 3 (model AM2, see table 5.1) to the classical formulation of OWC behaviour (model AM1). Humidity is introduced in the gaseous phase (model NM2) of the numerical model presented in Chapter 4 (model NM1), and a comparison is carried out between the theoretical real gas model for OWC (AM2) and numerical results (NM1 and NM2). The initial formulation proposed in Chapter 2 is used to solve numerically equations developed in Chapter 3.

	Dry air	Humid air
Analytical	AM1	AM2
Numerical	NM1	NM2

Table 5.1: Models used in the thesis.

5.1 Application of real gas analytical model to OWC formulation

Using a similar methodology to that of Sheng *et al.* (2013), who considered an ideal gas (model AM1), the thermodynamic theory developed in Chapter 3 for real gas is applied to the basic OWC chamber (model AM2). Assigning the subscript g to real gas variables, the manometric pressure inside the OWC is p_g. The temperature inside the OWC chamber is T_g. The pressure and temperature, p and T, will be ideal gas values. Please note that up to this point in the thesis, the pressure variable p has been cited generally. From now on, p_g is used to refer to the pressure calculated using the real gas formulation, noting that all relations where p was previously cited, are also applicable to p_g.

The First Law of Thermodynamics applied to the system, considering an ideal gas (Sheng *et al.* (2013)), gives

$$\frac{d\left(mC_vT\right)}{dt} = -p\frac{dV}{dt} + C_pT\dot{m} - \dot{\mathbb{Q}}\,. \tag{5.1}$$

where m is mass, C_v is specific heat at constant volume, t is time, T is temperature, p is pressure, V is volume, C_p is specific heat at constant pressure, and $\mathbb{Q}$ is heat. If real gas is considered and a considerable variation in pressure is present (for example, a sinusoidal variation of pressure with time would be expected in an OWC), the First Law of Thermodynamics becomes

$$\frac{dU}{dt} = -\left(p_g\frac{dV}{dt} + V\frac{dp_g}{dt}\right) + \dot{m}h - \dot{\mathbb{Q}}\,, \tag{5.2}$$

where U is the internal energy for a real gas, $\dot{\mathbb{Q}}$ is the transferred heat, and h is the enthalpy of the real gas. Taking into account that the process is adiabatic ($\dot{\mathbb{Q}} = 0$), the First Law reduces to

$$\frac{dU}{dt} = -p_g\frac{dV}{dt} - V\frac{dp_g}{dt} + \dot{m}h\,. \tag{5.3}$$

The mass of air inside the chamber is

$$m = \rho_g V\,, \tag{5.4}$$

where ρ_g is the density of a real gas. The volumetric flow rate driven by the

movement of water surface is defined as

$$Q_{owc} = -\frac{dV}{dt}\,. \tag{5.5}$$

Differentiating equation (5.4):

$$\frac{dm}{dt} = \rho_g \frac{dV}{dt} + V\frac{d\rho_g}{dt}\,. \tag{5.6}$$

Exhalation occurs when $dm/dt < 0$, and inhalation when $dm/dt > 0$.

Next, air density is taken into account. During exhalation, pressurized air is driven out through the PTO system, whereas during inhalation atmospheric air is sucked through the PTO. Hence, the air flow through the turbine (Q_T) is defined for each case as

$$\begin{cases} Q_T = -\frac{1}{\rho_0}\frac{dm}{dt}, & \text{inhalation,} \\ Q_T = -\frac{1}{\rho_g}\frac{dm}{dt}, & \text{exhalation.} \end{cases} \tag{5.7}$$

where ρ_0 is the external air density. In both cases, the power in the chamber, P_{owc}, is calculated from:

$$P_{owc} = pQ_{owc}\,, \tag{5.8}$$

where Q_{owc} is the volumetric air flow in the OWC chamber. Taking into account the difference between exhalation and inhalation, the power available to the PTO, P_{PTO}, is expressed as:

$$P_{PTO} = pQ_T\,. \tag{5.9}$$

For an adiabatic process involving a real gas, the relationship between density and pressure is given by

$$pv^n = constant \rightarrow \frac{p_g}{\rho_g^n} = constant\,, \tag{5.10}$$

or

$$\frac{p_0 + p_g}{\rho_g^n} = \frac{p_0}{\rho_0^n}\,, \tag{5.11}$$

between two consecutive states (where state "0" is the initial reference state). Then

$$\rho_g = \rho_0 \left(1 + \frac{p_g}{p_0}\right)^{\frac{1}{n}}\,, \tag{5.12}$$

and linearising,

$$\rho_g = \rho_0 \left(1 + \frac{p}{np_0}\right) . \tag{5.13}$$

In a similar way, temperature changes are determined using the adiabatic process equation for a real gas expressed as

$$T_g = T_0 \left(\frac{p_g}{p_0}\right)^{\left(\frac{n-1}{n}\right)} . \tag{5.14}$$

where T_g is the temperature of the real gas, and T_0 is the reference temperature. Note that n is the adiabatic index for a real gas. n depends on temperature and pressure changes, both of which can vary in time.

Differentiating equation (5.13):

$$\frac{d\rho_g}{dt} = \frac{d}{dt}\left(\rho_0 \frac{p_g}{np_0}\right) = \frac{\rho_0}{p_0}\left(\frac{1}{n}\frac{dp_g}{dt} + p_g \frac{d(1/n)}{dt}\right) . \tag{5.15}$$

Substituting equations (5.6), (5.13) and (5.15) into (5.7), the air flow through the turbine considering real gas is:

- Inhalation

$$\boxed{Q_T = \left(1 + \frac{p_g}{np_0}\right) Q_{owc} - \frac{V}{np_0}\frac{dp_g}{dt} - \frac{Vp_g}{p_0}\frac{d(1/n)}{dt}} \tag{5.16}$$

- Exhalation

$$\boxed{Q_T = Q_{owc} - \frac{V}{n(p_0 + p_g)}\frac{dp}{dt} - \frac{Vp_g}{p_0 + p_g}\frac{d(1/n)}{dt}} \tag{5.17}$$

It should be noted that equations (5.17) and (5.16) are essentially extended versions of the equations presented by Sheng *et al.* (2013), but take into account the effect on n of the real gas.

5.1.1 Application to a hypothetical pulse of pressure

For a general overview, efficiency is calculated over a hypothetical wave cycle. Please note that this enables an overall assessment of the expected differences between the ideal and real gas formulations for a given case. More accurate

results are given in Sections 5.1.2 (where this model is applied to a full range of wave conditions) and 5.3 (where the analytical model solutions are compared with numerical results). Efficiency can be calculated in general terms as

$$\eta = \frac{P_{PTO}}{P_{owc}}\,. \tag{5.18}$$

Figure 5.1 shows the efficiency calculated over a hypothetical pressure cycle, including inhalation and exhalation stages, for a sinusoidal pressure signal of 100 kPa amplitude that approximates the harmonic behaviour of gas within an OWC device. This is an idealisation of the process, as air flow and pressure are considered to be in phase, and a constant symmetric pressure value is given. Moreover, in a real process, radiation and diffraction phenomena will be affected by changes in pressure inside the OWC. This approach is now taken for verification purposes. An accurate pressure–power calculation taking into account all factors mentioned before is given in Section 5.1.2.

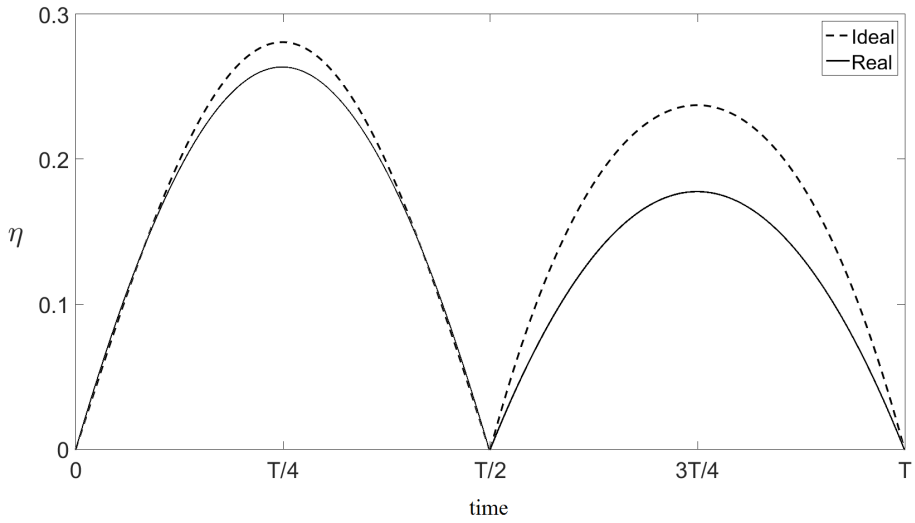

Figure 5.1: Temporal variations in efficiency of an OWC covering the exhalation (first half of the cycle) and inhalation (second half of the cycle) stages over one oscillation period T, for a sinusoidal pressure signal of amplitude 100kPa.

The efficiencies during both exhalation and inhalation stages are lower for a real gas than for a corresponding ideal gas. The discrepancy between the curves is less than 1.5% during exhalation, and reaches about 6% during inhalation.

During the first and third eighths of the cycle, the real gas efficiency curve slightly overlaps that of the ideal gas. This is related to the presence of real air. While the chamber is filling with fresh air (at the beginning of inhalation), the real gas model takes into account the change in density due to the mix of fresh and humid air. During exhalation, air inside the chamber leaves it, but density changes can be neglected. As long as the chamber is filled with fresh air (peak), the efficiency starts to vary as mixing occurs. During the second part of the inhalation process, the filling velocity starts to decrease, and the real and ideal gas power estimates converge according to equation (5.16).

Moreover, a rough calculation is presented to demonstrate the effect of the real gas formulation on the predicted phase of the airflow through the OWC turbine. Air flow in the OWC is calculated for exhalation and inhalation processes driven by the harmonic pressure change using equations (5.16) and (5.17) for real and ideal gas scenarios. The results are compared to predictions by Sheng *et al.* (2013) for an ideal gas flow. Figure 5.2 shows the time–dependent phase difference ($\Delta\psi$) obtained between the real and ideal air flow estimates over a complete pressure cycle.

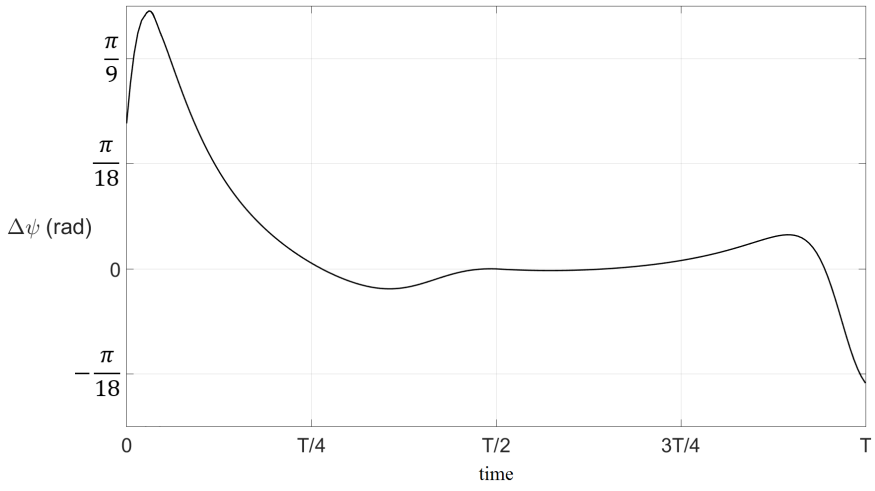

Figure 5.2: Temporal variation of phase difference between real and ideal air flows for exhalation (first half of the cycle) and inhalation (second half) over a pressure oscillation period (T) in an OWC chamber.

The curve exhibits almost no phase difference in the middle of the cycle because the pressure drop and associated water surface movement are both close to zero,

and the ideal and real air flow models give the same results. As the pressure drop increases, the phase difference also increases, exhibiting a peak soon after the start of the cycle. The peak and trough respectively represent the ends of the expansion and compression processes, and associated minimum and maximum water levels in the chamber. At $t = 0, T, 3T$, etc. the water surface is alternately located at either one of its opposite extremes, thus explaining the large difference between phases. Throughout the cycle, the phase gradually alters direction, with expansion and compression ending at opposite symmetric points. It should be noted that if the two processes immediately succeed each other, then the first will start at its maximum, ending at zero, after which the second process starts at zero and ends at its minimum.

5.1.2 Pressure inside OWC chamber considering real gas: coupling with radiation–diffraction model

The air flow equations summarised in Section 5.1 are now inserted in the classic OWC formulation, as developed by Martins–Rivas & Mei (2009–I). The goal is to obtain a new expression for power taking into account the properties of real gas. This procedure links the real gas formulation with the radiation–diffraction problem. In other words, a global model that takes into account thermodynamic and mechanical effects inside the OWC chamber is developed in this section.

The real gas model is expected to modify the radiation–diffraction problem, because the energy of the humid air inside the chamber is different from that of dry air. The wave–structure interaction problem for the OWC is divided into two separate problems: the radiation problem, and the diffraction problem. These two can be linked, Evans & Porter (1995), but in a first approach they are studied separately.

The radiation problem is defined by Martins–Rivas & Mei (2009–I) as the effect on the water surface elevation of the pulse of pressure produced inside the OWC chamber, assuming that the top of the device was closed. On the other hand, the diffraction problem is defined as the interaction between waves and structure, assuming there is not any kind of restriction for the air to travel up through the device to the open top (*e.g.* the turbine effect is not considered in the diffraction problem).

For the particular case of the real gas model coupled to the wave–structure interaction problem, the revised gas properties are expected to produce a different damping effect inside the chamber, modifying radiation. The effect on the diffraction part is not that obvious, as for that case the air properties are constant inside and outside the chamber. In any case, given that diffraction and radiation problems are linked, a complete approach taking into account both problems together is developed in this section.

To obtain a new value of power taking into account the real gas, the pressure equation is modified, taking into account the new airflow expressions obtained in (5.16) and (5.17). These expressions are linked to the turbine characteristic equation, presented by Martins–Rivas & Mei (2009–I), in order to link the airflow inside the OWC chamber (Q_T) and the water flow due to the water column displacement ($Q_{owc} = dV/dt$):

$$\frac{dm}{dt} = \rho_g \frac{dV}{dt} + V\frac{d\rho_g}{dt} = \frac{KD}{N} p_g \,, \tag{5.19}$$

where K is a coefficient depending on turbine geometry, D is the turbine diameter, and N is the revolutions per minute of the turbine. In this case, the same variables given by (Martins–Rivas & Mei , 2009–I) have been used: $K = 0.45$, $N = 2000\,\text{r.p.m.}$

The final expression for the volumetric water flow Q_{owc} is then related to the radiation and diffraction coefficients through the following equation:

$$Q_{owc} = Q^R + Q^D = -(\mathbb{B} - i\mathbb{C})p_g + \Gamma A_0 \tag{5.20}$$

where Q^R is the radiated flow, Q^D is the diffracted flow, $\mathbb{B}$ and $\mathbb{C}$ are the radiation coefficients, and Γ is the diffraction coefficient. A_0 is the incoming wave amplitude. The radiation and diffraction coefficients are obtained through the formulation in Martins–Rivas & Mei (2009–I) using a program implemented in Python (Jalón , 2016) [1]. This new pressure takes into account the properties of real gas and is a better approximation of the real working conditions. Power can then be calculated following Martins–Rivas & Mei (2009–I) (see Appendix I for the

[1]The author wants to thank Dr Lourdes Jalón, for permission to use the computer program developed for her thesis (Jalón , 2016) to calculate the radiation and diffraction coefficients.

developed expression) from:

$$P = \frac{KD}{N\rho_g}|p_g|^2\,. \tag{5.21}$$

5.1.2.1 Inhalation

For the case of inhalation, the new expression of pressure considering real gas is obtained by substituting (5.16) and (5.19) into (5.20). The equation to solve in this case is:

$$n\left(\frac{KD}{N\rho_0} - \frac{V}{p_0}\frac{d(1/n)}{dt} - i\frac{\omega V}{p_0 n}\right)\frac{p_0 p_g^{in}}{np_0 + p_g^{in}} = -\left(\mathbb{B} - i\mathbb{C}\right)p_g^{in} + \Gamma A_0 \tag{5.22}$$

where $i = \sqrt{-1}$, and p_g^{in} is the pressure for the real gas in the inhalation part of the cycle. By solving equation (5.22) taking into account the new formulation for n (see equation (3.125)), and iterating until the solution converges, the following expression for pressure is obtained for inhalation:

$$\boxed{p_g^{in} = \begin{cases} \dfrac{A_0\,N\,\Gamma\,\rho_0\;-\;\alpha\;-\;D\,K\,n\,p_0\;+\;\zeta\;-\;\kappa\;+\;\varepsilon\;+\;\vartheta}{\psi} \\ \dfrac{A_0\,N\,\Gamma\,\rho_0\;+\;\alpha\;-\;D\,K\,n\,p_0\;+\;\zeta\;-\;\kappa\;+\;\varepsilon\;+\;\vartheta}{\psi} \end{cases}} \tag{5.23}$$

where

$$\begin{aligned} \alpha = [&N^2\,V^2\,\rho_0^2\,\omega^2\;-\;D^2\,K^2\,n^2\,p_0^2\;-\;A_0^2\,N^2\,\Gamma^2\,\rho_0^2\;-\;\mathbb{B}^2\,N^2\,n^2\,p_0^2\,\rho_0^2 \\ &+\mathbb{C}^2\,N^2\,n^2\,p_0^2\,\rho_0^2 -\;N^2\,V^2\left(\frac{d(1/n)}{dt}\right)^2 n^2\,\rho_0^2\;+\;2\mathbb{B}\,N^2\,V\,\frac{d(1/n)}{dt}\,n^2\,p_0\,\rho_0^2 \\ &-2\mathbb{B}\,D\,K\,N\,n^2\,p_0^2\,\rho_0 -\;2A_0\,\mathbb{B}\,N^2\,\Gamma\,n\,p_0\,\rho_0^2\;-\;2A_0\,N^2\,V\,\frac{d(1/n)}{dt}\,\Gamma\,n\,\rho_0^2 \\ &+2\mathbb{C}\,N^2\,V\,n\,p_0\,\rho_0^2\,\omega +\;2A_0\,D\,K\,N\,\Gamma\,n\,p_0\,\rho_0\;+\;2D\,K\,N\,V\,\frac{d(1/n)}{dt}\,n^2\,p_0\,\rho_0 \\ &+(\mathbb{B}\,\mathbb{C}\,N^2\,n^2\,p_0^2\,\rho_0^2 -\;A_0\,N^2\,V\,\Gamma\,\rho_0^2\,\omega\;-\;N^2\,V^2\,\frac{d(1/n)}{dt}\,n\,\rho_0^2\,\omega \\ &-\mathbb{C}\,N^2\,V\,\frac{d(1/n)}{dt}\,n^2\,p_0\,\rho_0^2 +\;\mathbb{C}\,D\,K\,N\,n^2\,p_0^2\,\rho_0\;+\;A_0\,\mathbb{C}\,N^2\,\Gamma\,n\,p_0\,\rho_0^2 \\ &+\mathbb{B}\,N^2\,V\,n\,p_0\,\rho_0^2\,\omega\;+\;D\,K\,N\,V\,n\,p_0\,\rho_0\,\omega)\,2i]^{1/2}\,i\,, \end{aligned} \tag{5.24}$$

$$\psi = \left(\mathbb{B}N\rho_0 - \mathbb{C}N\rho_0\, i\right)^2 \,, \tag{5.25}$$

$$\varepsilon = \mathbb{C}Nnp_0\rho_0\, i \,, \tag{5.26}$$

$$\zeta = NV\rho_0\omega\, i \,, \tag{5.27}$$

$$\vartheta = NV\frac{d(1/n)}{dt}n\rho_0 \,, \tag{5.28}$$

and

$$\kappa = \mathbb{B}Nnp_0\rho_0 \,. \tag{5.29}$$

This set of equations were obtained using the Matlab® tool *solve*. The solution given by Matlab® is very easy to implement numerically. Later on, as the equation obtained is implicit, the complete problem (taking into account pressure variations linked to adiabatic index variations, and *vice versa*) has been solved numerically using the *Newton Method*. This method converges very rapidly given a suitable initial value for pressure, after about the 6^{th} or 7^{th} iteration, with a relative error lower than 1%.

The lower solution in equation (5.23) gives valid values of pressure, unlike the upper solution, which gives unphysical results. It should be noted that if the initial airflow equations (5.16) and (5.17) were to be linearised a second time in terms of pressure–density relationship (following equation (5.13)), the set of equations obtained for pressure would be exactly equivalent to those presented by Martins–Rivas & Mei (2009–I).

In the classical formulation, the derivative of pressure is linearised with the derivative of density in time by means of the speed of sound in air at the beginning of the theoretical analysis. The result obtained either by this simplification or using equation (5.13) are identical provided the adiabatic index is taken to be constant. However, the present thesis makes the main hypothesis that the adiabatic conditions change in time in the OWC chamber, and so the derivative of n in time has to be taken into account. Then, another simplification step is needed to achieve the same results as given by the classical formulation. This aspect is very important, because it highlights that the inclusion of certain simplifications

at the beginning of the theoretical analysis ignores future considerations in the formulation.

5.1.2.1.1 Application of coupled real gas–radiation–diffraction analytical model to a hypothetical pulse of pressure

In order to compare the differences between real and ideal gas models, the same hypothetical pulse of pressure analysed in Section 5.1.1 is now applied to the coupled real gas–radiation–diffraction model. The pulse of pressure is used to trigger the system formed by n and p_g^{in} (see equations (3.125) and (5.23), respectively).

Table 5.2 summarises the simulated wave conditions considered herein with the subsequent non–dimensional radiation coefficients ($\tilde{\mathbb{B}}$ and $\tilde{\mathbb{C}}$). Here the diffraction coefficient is calculated from (Evans & Porter (1995)),

$$\tilde{\Gamma} = \left| \sqrt{\frac{4\tilde{\mathbb{B}} C_g \omega}{kag}} \right| . \tag{5.30}$$

where C_g is the wave group celerity, ω is the wave frequency, k is the wave number, a is the OWC radius, and g is the gravitational acceleration. It should be noted that results for the real gas model were found to have a very weak dependence with the value of the diffraction coefficient Γ. The specific definition of the diffraction and radiation problems implies that phenomena inside the OWC chamber only cause variations in the radiation coefficients, and *vice versa*.

The wave height H is taken as a fixed parameter, because numerical tests showed that the choice of values for H had negligible effects on results. Submergence of the OWC device is fixed to 2 m, and water depth to $h = 10$ m. Three different OWC diameters are used to compare geometry scale effects: $D = 20\,, 10\,, 5$m (corresponding to $a/h = 1$, $a/h = 0.5$, and $a/h = 0.25$). The results were obtained using the numerical solver developed by Jalón (2016).

		$a/h = 1$		$a/h = 0.5$		$a/h = 0.25$	
$T(s)$	kh	$\tilde{\mathbb{B}}$	$\tilde{\mathbb{C}}$	$\tilde{\mathbb{B}}$	$\tilde{\mathbb{C}}$	$\tilde{\mathbb{B}}$	$\tilde{\mathbb{C}}$
12.56	0.5275	0.1796	0.9825	0.0235	0.4515	0.0029	0.2154
6	1.2980	3.6088	4.0993	0.6026	2.3516	0.0809	1.0548
4	2.5462	12.5630	2.0513	5.3191	5.7734	1.2891	3.8108
3	4.4726	0.6272	0.1511	16.6568	3.2331	6.3360	7.4048
2.5	6.4389	6.9515	12.9499	6.9136	12.3221	15.7919	7.9301

Table 5.2: Radiation coefficients for $a/h = 1$, $a/h = 0.5$ and $a/h = 0.25$.

The results shown in table 5.2 are plotted in figures 5.3 and 5.4. Values of the non–dimensional radiation damping coefficient, $\tilde{\mathbb{B}}$, see figure 5.3, are in the same range as those presented in Martins–Rivas & Mei (2009–I). The same growing crests are observed, although the values are slightly lower for $a/h = 0.25$. There are some values after $kh = 5$ that are not present in the plot from Martins–Rivas & Mei (2009–I). Those frequencies are analysed carefully. Figure 5.4 presents results obtained for the radiation added mass coefficient, $\tilde{\mathbb{C}}$, and the results given by Martins–Rivas & Mei (2009–I). As in the radiation damping case, the results are slightly lower than expected for the smaller radius, and some values appear after $kh = 4$ for $a/h = 0.5$ and $a/h = 1$ that are not present in the figure from Martins–Rivas & Mei (2009–I).

The non–dimensional radiation and diffraction coefficients are related to the dimensional counterparts by the following equations (Martins–Rivas & Mei , 2009–I):

$$(\tilde{\mathbb{B}}, \tilde{\mathbb{C}}) = \frac{(\mathbb{B}, \mathbb{C})}{\left(\dfrac{a}{\omega \rho_w}\right)}, \tag{5.31}$$

and

$$\tilde{\Gamma} = \frac{\Gamma}{\left(\dfrac{ag}{\omega}\right)}, \tag{5.32}$$

where a is the OWC radius, ω is the wave frequency, and ρ_w is the water density. A brief recap of the formulation presented by (Martins–Rivas & Mei , 2009–I) is given in Appendix I.

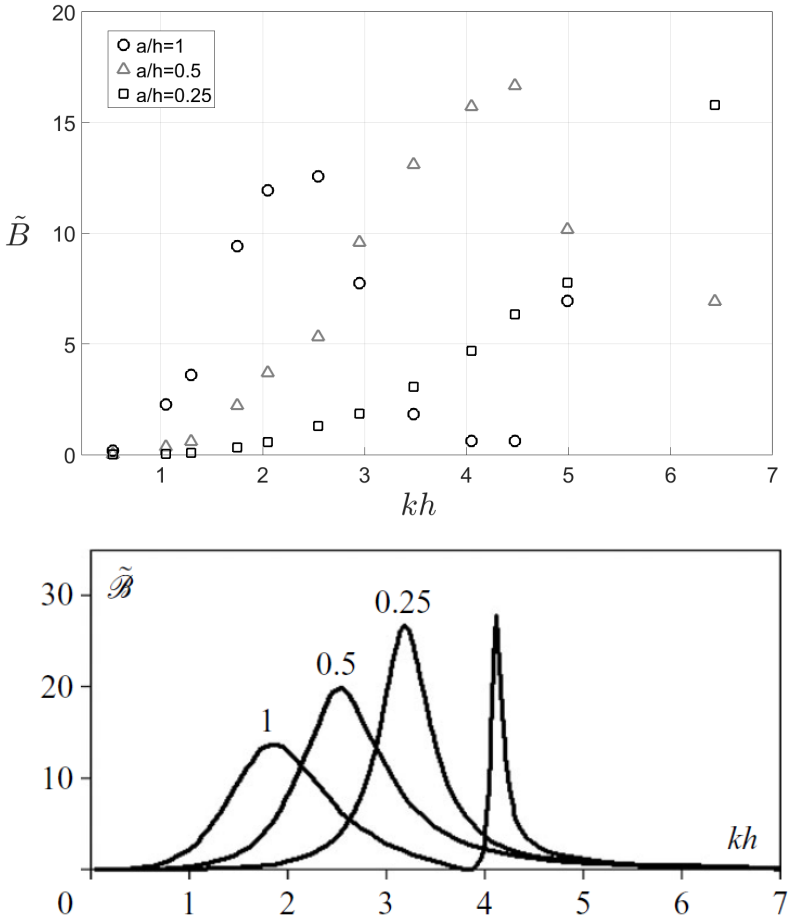

Figure 5.3: Top: non-dimensional radiation damping coefficient $\tilde{\mathbb{B}}$ as a function of kh for three different a/h values. Bottom: radiation damping coefficient obtained from Martins–Rivas & Mei (2009–I).

Now, the coupled real gas and radiation–diffraction OWC model is applied to the hypothetical pressure pulse that was analysed at the end of Section 5.1. This is undertaken to check for any discrepancies between the results from application of the real gas model, and those when insertion of the wave–structure interaction is linked to the real gas approach. Again, the following test results are for a symmetrical, simple pulse of pressure, which is not how an OWC behaves, but is nevertheless a useful exercise by which to analyse how the results may change with different wave conditions. Later, Section 5.3 describes the full application of the real gas model plus radiation–diffraction theory (model AM2, see table5.1) in a numerical flume, in order to check the influence of the new formulation under

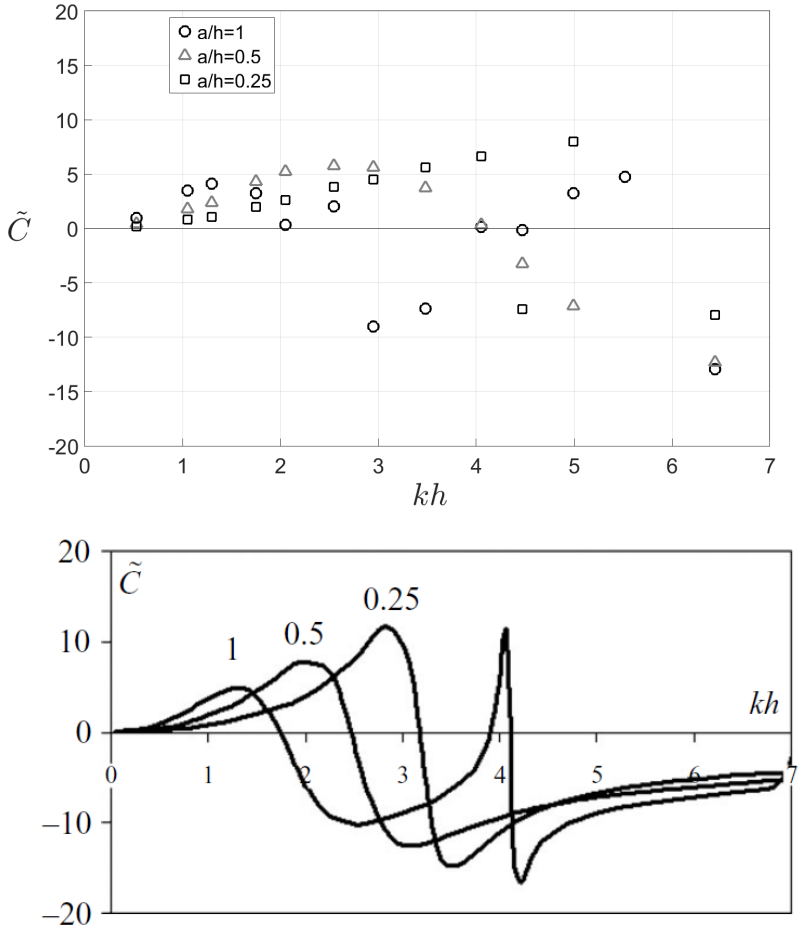

Figure 5.4: Top: non-dimensional radiation coefficient $\tilde{\mathbb{C}}$ as a function of kh for three different a/h values. Bottom: radiation added mass coefficient obtained from Martins–Rivas & Mei (2009–I).

more realistic wave–structure interactions. Results from the real gas model linked to radiation–diffraction theory are compared with numerical results for a 2D wave flume under two different air conditions: dry air (model NM1) and humid air (model NM2).

Figure 5.5 shows the ratio between real gas power output (P_r) obtained from equation (5.21) for the real value of pressure calculated from (5.23), and ideal gas power output (P_i) as presented in Martins–Rivas & Mei (2009–I).

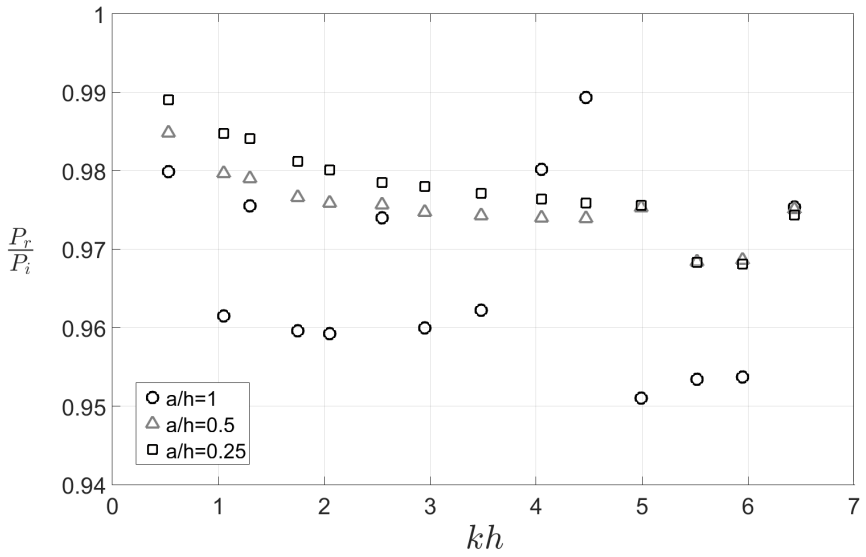

Figure 5.5: Power ratio for real and ideal gas approaches over kh values.

Figure 5.5 shows that at lower values of kh (equivalent to larger wave periods), the real and ideal gas estimates of power are almost the same. However, as the the wave number increases, there is a noticeable decrease in power ratio, up to a 5% difference between real and ideal gas estimates. However, for $kh = 4.7$, and $a/h = 1$, there is a peak that does not follow the pattern at $a/h = 0.5$ and $a/h = 0.25$. Figure 5.6 presents the relationship between capture length (kL) and normalised wave number kh obtained by Martins–Rivas & Mei (2009–I) for $a/h = 0.25\,, 0.5$ and 1.

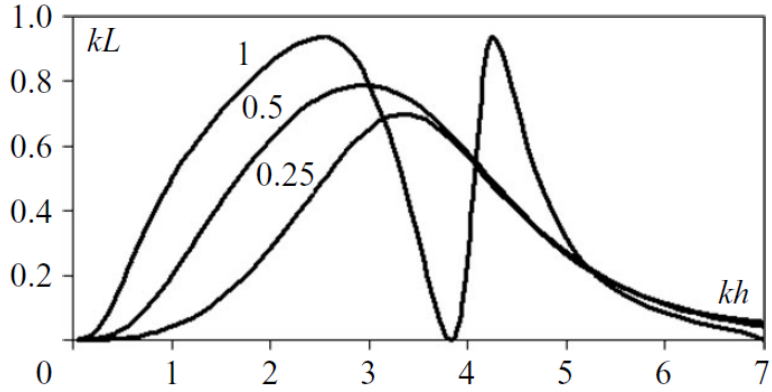

Figure 5.6: Capture length as function of the normalized wave number kh for different water column sizes a/h. [Source: Martins–Rivas & Mei (2009–I)]

The capture length of an OWC depends on the radiation and diffraction coefficients, OWC geometry, and wave parameters. However, kL is not independent of the choice between real and ideal gas model. The radiation coefficient depends on the nature of the gas, because the pulse of pressure produced inside the OWC chamber is linked to the process equation followed by the gas. The process equation ($pv^n = constant$) is modified with the real gas formulation, through changes in the adiabatic coefficient n, as presented in Chapter 3. Then, the relationship between volume and pressure when the real gas is considered is different to that of the ideal gas formulation. In other words, for a given volume, the pressure inside the chamber when the real gas is taken into account is different to that of the ideal gas. Thus, the radiation effect will be different when the real gas formulation is used.

Despite the difference between real and ideal gas approaches in terms of radiation, resonance is shown to be an important phenomena in both cases. In figure 5.5, a peak occurs at $kh = 4.7$ for the case of $a/h = 1$, which is not present for the other values considered. That form is also present in figure 5.6. Both peaks in figures 5.5 and 5.6 are due to the same phenomena at $kh = 4.7$ for $a/h = 1$, most likely related to device resonance, as presented by Medina-Lopez *et al.* (2017–II).

In conclusion, the OWC power outputs in waves of larger periods are less influenced by the choice of real or ideal gas model, and are therefore not considered further. On the other hand, for short waves it is recommended that the effect of the real gas is taken into account.

5.1.2.2 Exhalation

For the case of exhalation, an expression for pressure based on the real gas model is obtained by substituting (5.17) and (5.19) into (5.20). The resulting equation to solve is:

$$\frac{KD}{N\rho_g} - \frac{p_g^{ex} V \left(\dfrac{\partial(1/n)}{\partial t}\right)}{p_0 + p_g^{ex} e^{-i\omega t}} - i\frac{\omega V}{n\left(p_0 + p_g^{ex} e^{-i\omega t}\right)} = -\left(\mathbb{B} - i\mathbb{C}\right) p_g + \Gamma A_0 \qquad (5.33)$$

Taking into account real gas in the exhalation part of the cycle, the pressure is given by

$$\boxed{p_g^{ex} = \begin{cases} -\dfrac{D\,K\,n\,p_0 \;+\; \tau \;+\; \zeta_g \;+\; \varsigma \;-\; \kappa_g \;+\; \varepsilon_g \;-\; \vartheta_g}{\varrho} \\ -\dfrac{D\,K\,n\,p_0 \;-\; \tau \;+\; \zeta_g \;+\; \varsigma \;-\; \kappa_g \;+\; \varepsilon_g \;-\; \vartheta_g}{\varrho}\,, \end{cases}} \tag{5.34}$$

where

$$\begin{aligned} \tau = [&-N^2\,V^2\,\rho_g^2\,\omega^2 \;+\; D^2\,K^2\,n^2\,p_0^2 \;+\; A_0^2\,N^2\,\Gamma^2\,n^2\,\rho_g^2 \\ &+\mathbb{B}^2\,N^2\,n^2\,p_0^2\,\rho_g^2 - \;\mathbb{C}^2\,N^2\,n^2\,p_0^2\,\rho_g^2 \;+\; 2A_0\,\mathbb{B}\,N^2\,V\,\frac{d(1/n)}{dt}\,\Gamma\,n^2\,p_0\,\rho_g^2 \\ &+N^2\,V^2\,\left(\frac{d(1/n)}{dt}\right)^2\,n^2\,\rho_g^2 \;-2A_0\,N^2\,V\,\frac{d(1/n)}{dt}\,\Gamma\,n^2\,\rho_g^2 \\ &+2\mathbb{B}\,N^2\,V\,\frac{d(1/n)}{dt}\,n^2\,p_0\,\rho_g^2 \;-\; 2\mathbb{B}\,D\,K\,N\,n^2\,p_0^2\,\rho_g \;-\; 2\mathbb{C}\,N^2\,V\,n\,p_0\,\rho_g^2\,\omega \\ &-2A_0\,D\,K\,N\,\Gamma\,n^2\,p_0\,\rho_g \;-\; 2D\,K\,N\,V\,\frac{d(1/n)}{dt}\,n^2\,p_0\,\rho_g \;+\; (-\mathbb{B}\,\mathbb{C}\,N^2\,n^2\,p_0^2\,\rho_g^2 \\ &-N^2\,V^2\,\frac{d(1/n)}{dt}\,n\,\rho_g^2\,\omega \;-\; A_0\,\mathbb{C}\,N^2\,\Gamma\,n^2\,p_0\,\rho_g^2 \;-\; \mathbb{C}\,N^2\,V\,\frac{d(1/n)}{dt}\,n^2\,p_0\,\rho_g^2 \\ &+\mathbb{C}\,D\,K\,N\,n^2\,p_0^2\,\rho_g \;+\; A_0\,N^2\,V\,\Gamma\,n\,\rho_g^2\,\omega \;-\; \mathbb{B}\,N^2\,V\,n\,p_0\,\rho_g^2\,\omega \\ &+D\,K\,N\,V\,n\,p_0\,\rho_g\,\omega)\,2i]^{1/2}\,, \end{aligned} \tag{5.35}$$

$$\varrho = (DKn - \mathbb{B}Nn\rho_g + \mathbb{C}Nn\rho_g\,i)^2\;, \tag{5.36}$$

$$\varepsilon_g = \mathbb{C}Nnp_0\rho_g\,i\,, \tag{5.37}$$

$$\zeta_g = NV\rho_g\omega\,i\,, \tag{5.38}$$

$$\vartheta_g = NV\frac{d(1/n)}{dt}n\rho_g\,, \tag{5.39}$$

$$\kappa_g = \mathbb{B}Nnp_0\rho_g\,, \tag{5.40}$$

and

$$\varsigma = A_0N\Gamma n\rho_g\,. \tag{5.41}$$

As in the inhalation case, the upper solution in equation (5.34) does not give representative values of pressure. The lower solution gives physically meaningful results. Note that the groups called "$\varepsilon_g\,,\zeta_g\,,\vartheta_g$ and κ_g", are equivalent to the groups "$\varepsilon\,,\zeta\,,\vartheta$ and κ" presented for the Inhalation part of the process, but with the reference density ρ_0 substituted by the real gas density ρ_g.

In the case of the exhalation part of the cycle, equation (5.34) was tested for different wave conditions, there was a very close agreement between the real and ideal gas model estimate of power output.

In conclusion, ideal gas theory is a valid approach to simulate the exhalation part of the cycle. Any discrepancy is primarily due to the value of the specific heat (C_p). In the inhalation phase, C_p drops significantly compared to the ideal gas value. However, in the exhalation calculation, C_p remains almost the same as in the ideal case, producing very little change in the process equation, and thus the results are almost the same as in the ideal formulation.

5.2 Insertion of humidity in a 2D numerical model containing a linear turbine

Humid air is now implemented as the gaseous phase of the numerical model in Fluent® (model NM2). The flume and turbine model used here are the same as described in Section 4.4 (model NM1).

Although Fluent® presents the possibility to run simulations with real gases, such simulation presents some limitations: it can only be run for single phase problems (*e.g.* no multiple fluids involved), and the vapour involved has to be present in superheated state (*e.g.* in this case, water vapour over 100°C). To achieve this, a density–based solver is required, Fluent (2006). For the purpose of this thesis, a pressure–based solver is therefore utilised to simulate accurately the interface between water and air. Moreover, when the real gas model is used, all fluid zones must contain real gas, *i.e.* a real gas cannot be included with another fluid in the same problem. Finally, the gas considered herein is air at normal ambient conditions containing some degree of water vapour. In other words, the gas phase is humid air in equilibrium.

For these reasons, calculations for real gas inside an OWC cannot be undertaken using the real gas tool of Fluent®. Thus, a new gas with different density, specific heat at constant pressure and molar weight, following the results of the real gas model presented in previous chapters, is inserted as the gaseous phase of the numerical flume. This gas then behaves as a mixture of dry air and water vapour. It is not a real gas, but the approach offers a useful tool by which to compare the results of the theoretical model. Humid air characteristics are set following the theoretical model developed in Chapter 3, as shown in table 5.3.

	Dry air	Humid air
ρ	$1.225\,kg/m^3$	$1.19\,kg/m^3$
C_p	$1006.43\,J/kg \cdot K$	$1503.70\,J/kg \cdot K$
M	$28.966\,g/mol$	$21.4\,g/mol$

Table 5.3: Dry and humid air characteristics.

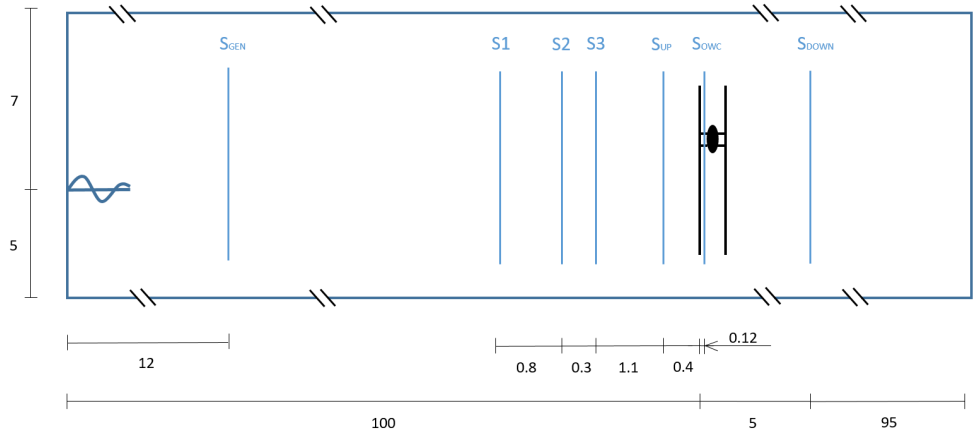

Figure 5.7: Numerical gauge scheme. Units in m.

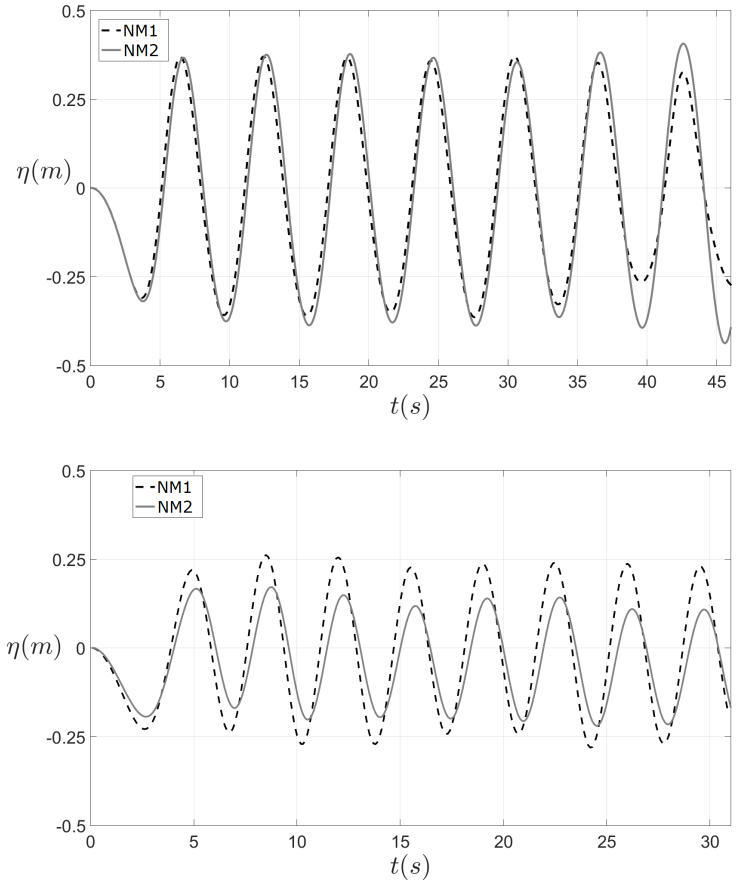

Figure 5.8: Free surface elevation time history at generation gauge ($x = 12\,\text{m}$) for humid and dry air conditions. $H = 1\,\text{m}$, $T = 6\,\text{s}$ (top); $H = 0.5\,\text{m}$, $T = 3.5\,\text{s}$ (bottom).

Figure 5.7 provides a reminder as to the gauge locations. Figure 5.8 shows the free surface elevation time history obtained for both dry and humid tests at the generation gauge ($x = 12\,\mathrm{m}$) for two sets of wave conditions. Figure 5.9 presents the free surface elevation time history inside the OWC chamber ($x = 100\,\mathrm{m}$).

The free surface elevation time series predicted using the humid air model (NM2), and dry air model (NM1) are nearly the same at the generation gauge for the first case ($H = 1\,\mathrm{m}$, $T = 6\,\mathrm{s}$). Some differences start to appear near $t = 40\,\mathrm{s}$. Given that the OWC is located in the middle of the flume, at $x = 100\,\mathrm{m}$, and noting that the wave speed would be about $6\,\mathrm{m/s}$, the initial wave crest would take $17\,\mathrm{s}$ to arrive at the OWC, and $15\,\mathrm{s}$ to return back to the generation gauge, located at $x = 12\,\mathrm{m}$, after reflection. Hence, reflection effects are experienced by the OWC after $32\,\mathrm{s}$.

In the second case considered ($H = 0.5\,\mathrm{m}$, $T = 3.5\,\mathrm{s}$), there are substantial differences between the waveform generated for dry and humid conditions. These discrepancies are caused by viscous effects: the value of viscosity was not altered in this case, although it should have been modified to be consistent with the variations in specific heat, molar weight and density. Moreover, as the wave height is relatively small, viscous effects become more relevant. Despite this discrepancy, viscosity was not changed in the analytical real gas model (model AM2) in order to be consistent. This provides a useful check to verify the accuracy of model AM2 in later sections.

It is clear from figure 5.9 that a phase difference occurs in the free surface motion inside the OWC chamber when humidity is taken into account. The phase difference affects the radiated and reflected waves. This is as expected (see Section 5.1). However, the variation is likely to be larger than would actually occur because of the inviscid fluid assumptions in the present Fluent® model. This configuration does not account for the effect of viscosity on the flow, which is affected by the new air conditions, Fluent (2006). The assumption of inviscid flow is valid if the inertial forces dominate over the fluid viscous forces. This may incorporate some level of error, but for a first approach it is considered to be valid.

Turning to the free surface elevation time history inside the OWC for $H = 0.5\,\mathrm{m}$, $T = 3.5\,\mathrm{s}$, the results show a similar phase difference as observed for the $H = 1\,\mathrm{m}$, $T = 6\,\mathrm{s}$ case.

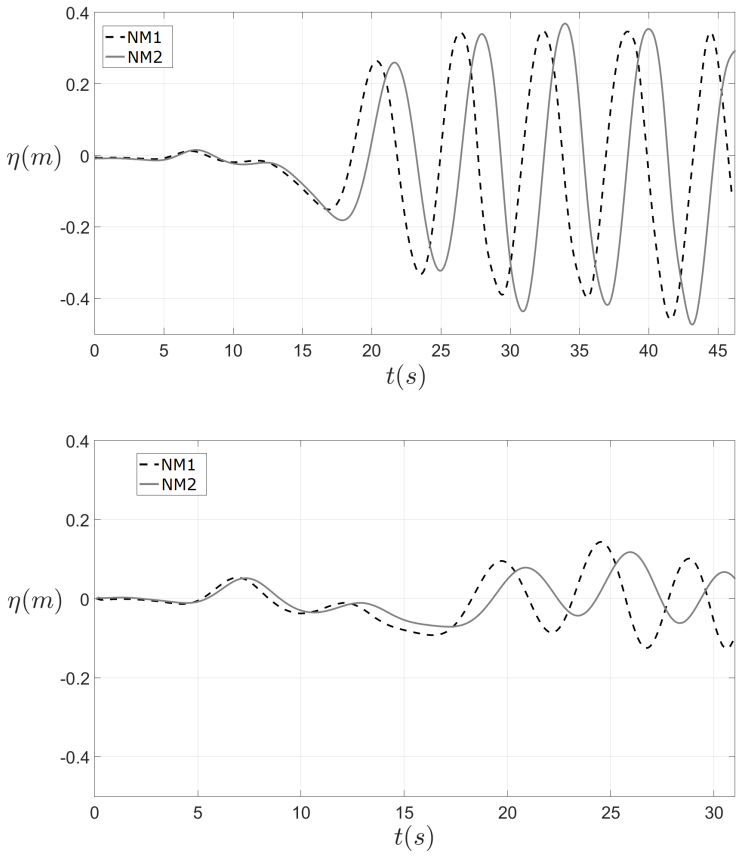

Figure 5.9: Free surface elevation time history inside the OWC for humid and dry air conditions. $H = 1\,\text{m}$, $T = 6\,\text{s}$ (top); $H = 0.5\,\text{m}$, $T = 3.5\,\text{s}$ (bottom).

The scatter of pressure–air flow value about the trend line is very small for humid conditions, see figure 5.10). Whereas the $\Delta p - Q$ curve slope is the same for both dry and humid conditions, the extent of the humid case is lower than for the dry case. This affects power output, which is calculated as a function of pressure drop and air flow, meaning that power is lower in humid conditions, because both pressure and air flow are reduced.

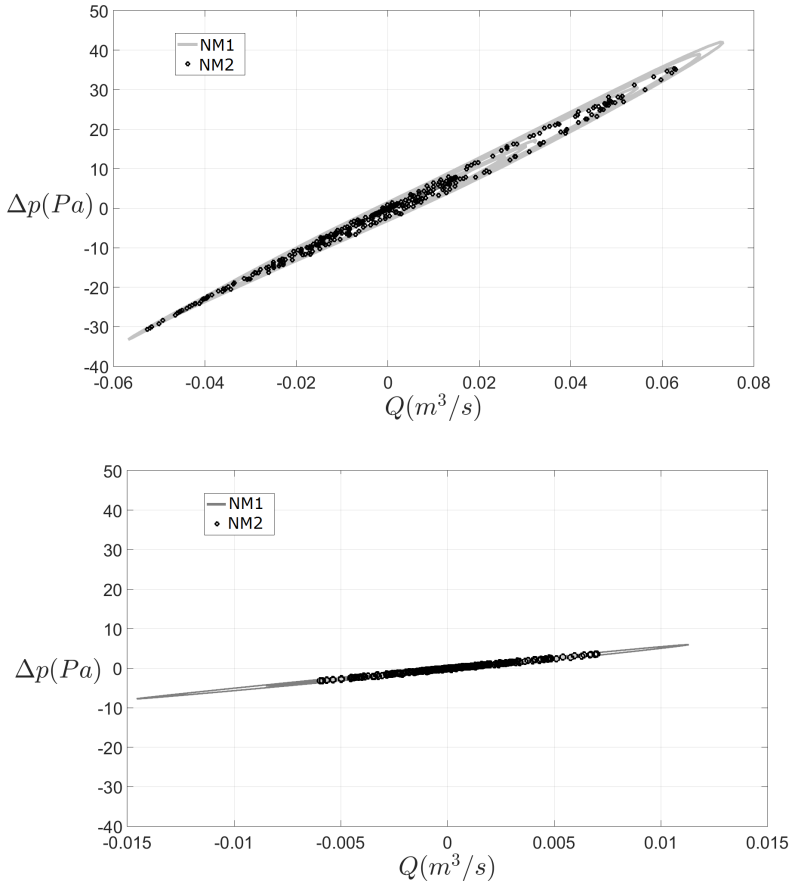

Figure 5.10: Pressure drop dependence on air flow inside OWC for humid and dry air conditions. $H = 1\,\text{m}$, $T = 6\,\text{s}$ (top); $H = 0.5\,\text{m}$, $T = 3.5\,\text{s}$ (bottom).

The difference between ideal and real gas models can be observed in figure 5.11, where it is evident that slight differences in pressure drop make a big difference in power output. For the $H = 0.5\,\text{m}$, $T = 3.5\,\text{s}$ case, the same comments are applicable, but an even bigger difference is observed between dry and humid conditions. It should be noted that, although viscosity–induced differences lead to a notable variation in power output, this variation would have been much smaller if an accurate air viscosity value had been available.

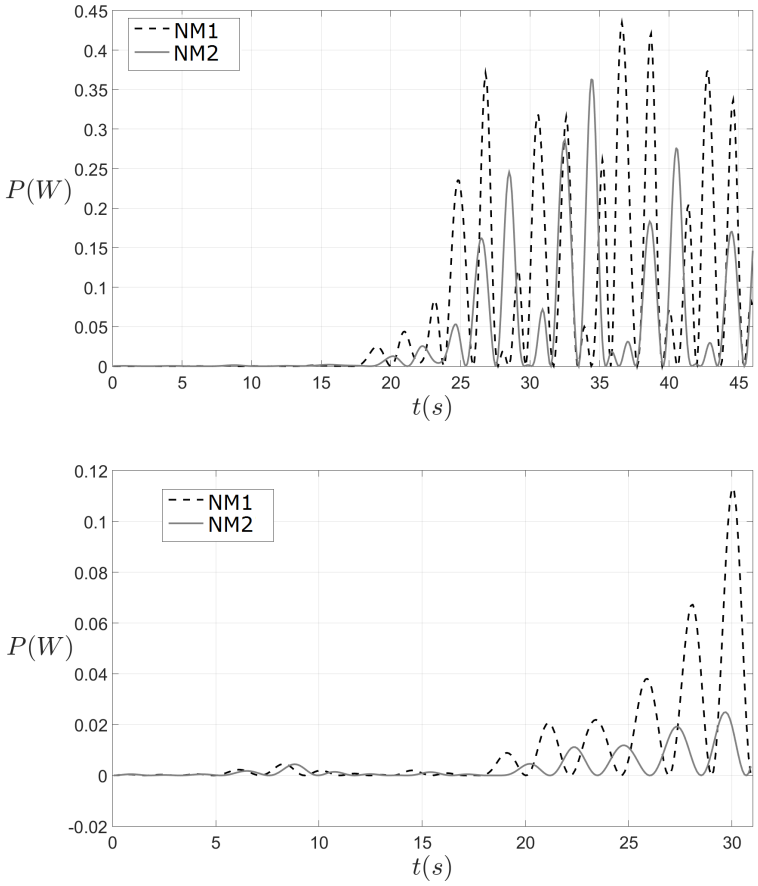

Figure 5.11: Available power at turbine for humid and dry air conditions. $H = 1\,\text{m}$, $T = 6\,\text{s}$ (top); $H = 0.5\,\text{m}$, $T = 3.5\,\text{s}$ (bottom).

5.3 Comparison of real gas analytical model and numerical models for OWC performance

In this section, comparison is made between the numerical predictions from models NM1 (dry conditions) and NM2 (humid conditions), and the analytical real gas model (AM2) developed in Chapter 3. As the pressure and adiabatic coefficient equations (see equations (3.118) and (5.23)) form a set of implicit equations, an initial value is needed to solve the system. Pressure results obtained from model NM1 in Fluent® are inserted into model AM2. This way, we can see how the real gas analytical model (AM2) modifies ideal results from model NM1, and then compare them with the results from model NM2. The proposed methodology is summarised in figure 5.12.

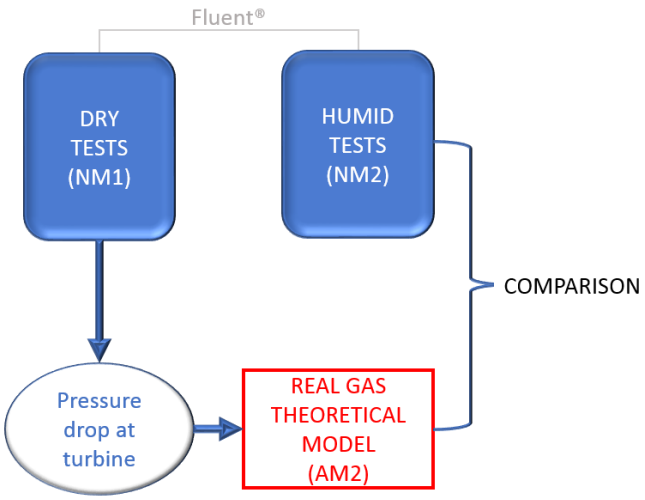

Figure 5.12: Proposed working procedure to obtain real gas pressures using the analytical model.

As tests presented in this section are run for several waves (a sea state), the results are inherently different to those obtained in Chapter 3 for an ideal single wave cycle. This is primarily due to the application of a dynamic model instead of a standing wave model where the free surface elevation is in phase with the theoretical pressure. For an ideal sinusoidal signal, the power ratio between ideal and real gas model is about 95 % (see Section 5.1.2.1). However, with the 2D numerical simulations more realistic wave conditions are analysed, taking into account changing radiation and diffraction phenomena, considered constant throughout the analysis in previous

chapters. Moreover, the energy calculations carried out in the numerical solver take into account heat exchange. The real gas model through the virial formulation is specified to take into account inter-molecular interactions which are ignored in the ideal gas model. That said, a much bigger difference between real and ideal formulation is expected for long term or life cycle analysis.

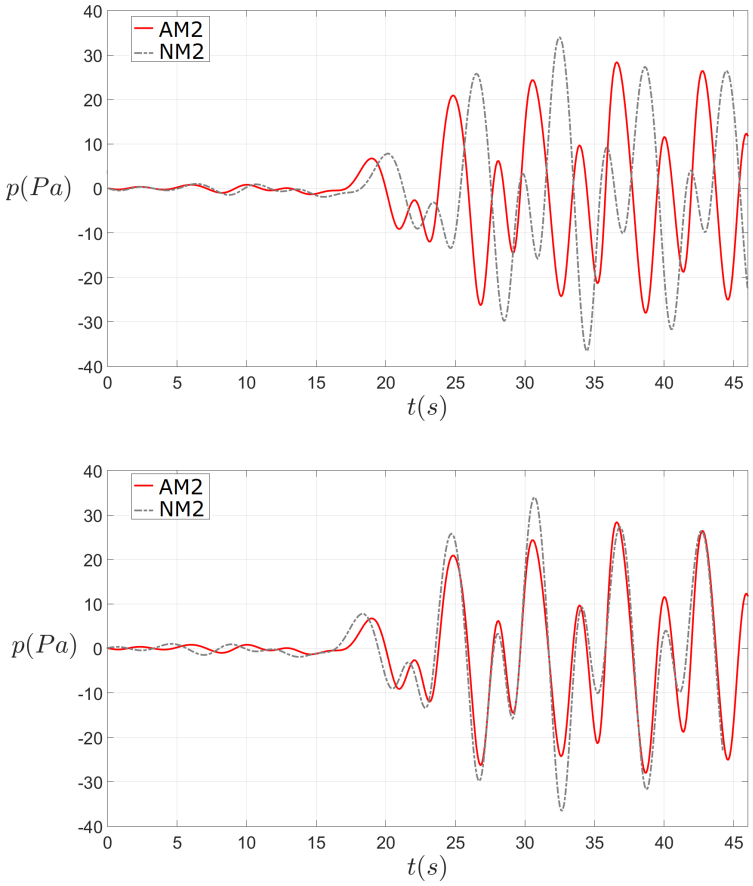

Figure 5.13: Pressure time series inside OWC chamber for numerical tests using the humid air model (NM2), and the analytical real gas model (AM2). $H = 1\,\text{m}$, $T = 6\,\text{s}$. Raw time series (top), shifted time series (bottom).

Figure 5.13 shows the pressure variations in time obtained using the model NM2, and model AM2. The upper figure presents the raw data which exhibit a phase difference. It should be noted that model AM2 is in phase with the ideal dry air numerical model (NM1). The pressure–adiabatic index system strongly depends on the specified initial values. Although the variations in pressure magnitude are accounted for, the phase does not match the expected results. To compare

values more effectively the numerical results are translated 2 s in the lower figure where the two curves are almost overlapping. The same procedure is followed for the second wave conditions ($H = 0.5\,\text{m}$, $T = 3.5\,\text{s}$) as shown in figure 5.14. In this case, slightly better agreement is obtained. Although the surface elevation time series differ for dry and humid numerical cases, viscosity effects are more relevant for smaller waves, making inhalation and exhalation phenomena nearly symmetrical. As the present formulation only simulates the inhalation phase, the theoretical real gas simulation will be closer to the actual phenomena for smaller waves.

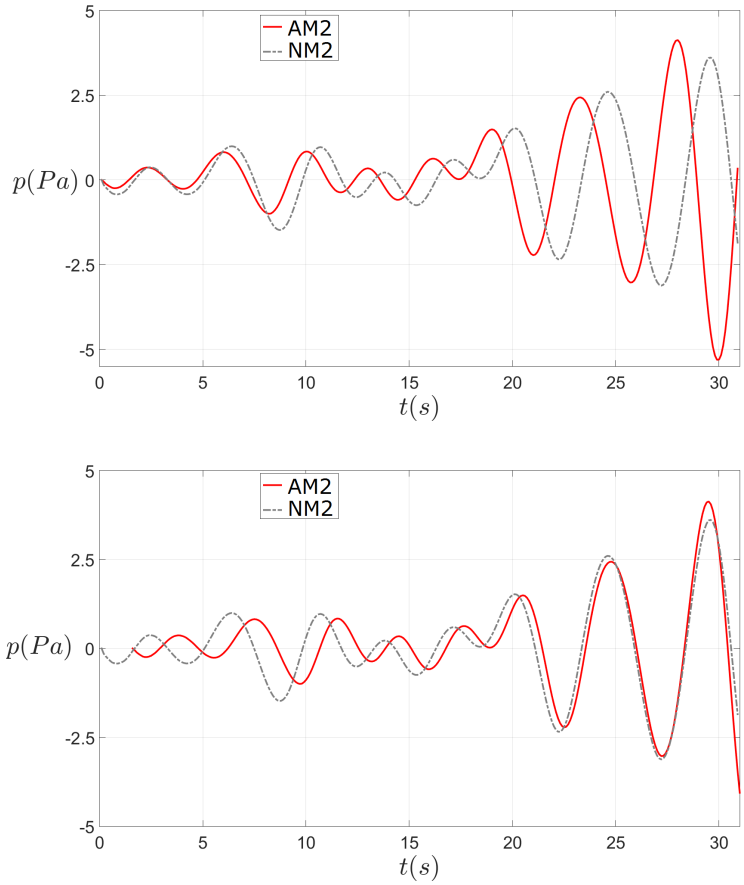

Figure 5.14: Pressure time series inside OWC chamber for numerical test using the humid air model (NM2), and the analytical real gas model (AM2). $H = 0.5\,\text{m}$, $T = 3.5\,\text{s}$. Raw time series (top), shifted time series (bottom).

Figure 5.15 shows the predicted available power time series at the OWC turbine using models NM1 (dry air, numerical), NM2 (humid air, numerical), and AM2

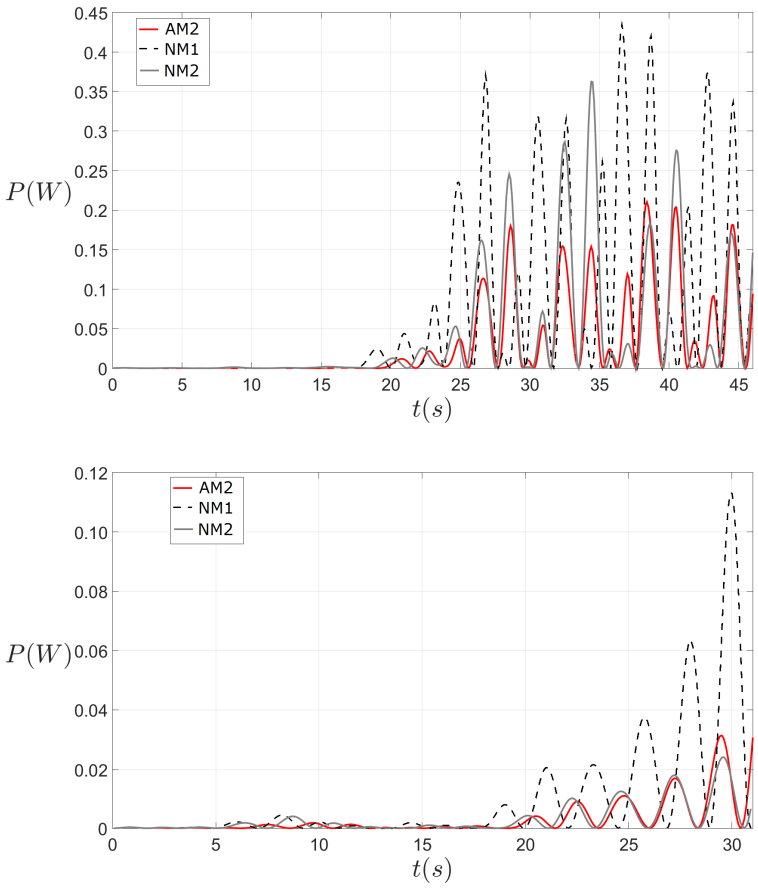

Figure 5.15: Available power time series at OWC turbine obtained using the numerical dry air model (NM1), numerical humid air model (NM2), and analytical real gas model (AM2): $H = 1\,\text{m}$, $T = 6\,\text{s}$ (a); $H = 0.5\,\text{m}$, $T = 3.5\,\text{s}$ (b).

(analytical real gas model). The power peaks are higher for model NM1. The average behaviour of model NM2 and model AM2 power series is similar, although model NM2 presents some higher peaks that are not present in the analytical approach. Model AM2 merely represents the inhalation phase, and so the higher peaks are not obtained. The lower figure supports the hypothesis that model AM2 fits better smaller waves, where the inhalation and exhalation phases are symmetric. Moreover, the analytical model depends more on changes in specific heat and density when the waves are smaller. For larger scale waves, dynamic phenomena rule the wave behaviour, increasing the difference between the real gas analytical model and numerical simulations. Power values are smaller than expected due to the effects of viscosity. However, the analytical model gives results

in very good agreement with its numerical counterpart. As long as the values are consistent, it is reasonable to conclude that both models, NM2 and AM2, can be used to simulate OWC real working conditions.

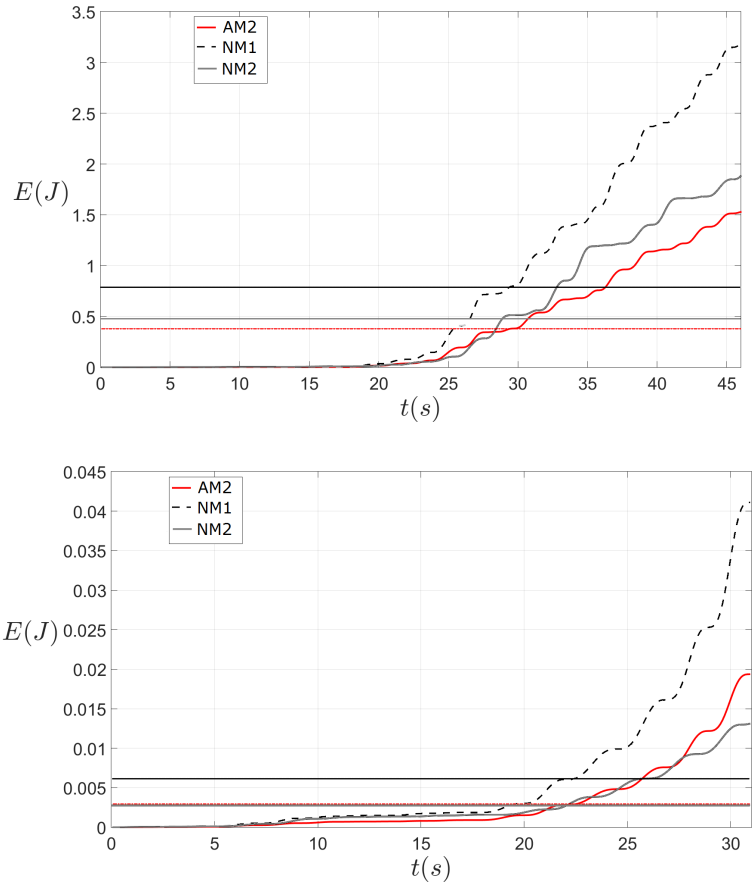

Figure 5.16: Cumulative energy time series, and mean energy at OWC turbine obtained using the numerical dry air model (NM1), numerical humid air model (NM2), and analytical real gas model (AM2): $H = 1\,\text{m}$, $T = 6\,\text{s}$ (a); $H = 0.5\,\text{m}$, $T = 3.5\,\text{s}$ (b).

In terms of energy, figure 5.16 presents cumulative available energy at the turbine for the three cases, together with the average values. It is easily observed that the predictions by model NM1 are far from those of models NM2 and AM2. The NM2 and AM2 predictions are similar, although differences might grow in time. For smaller waves, the average energy values obtained using models NM2 and AM2

are nearly overlapping. Table 5.4 shows the energy ratio obtained for the different tests presented in Chapter 4.

Although an energy ratio of about 50% is observed between model AM2 and model NM1, slightly different values are obtained for model NM2. For frequencies different than 0.9 Hz (*i.e.* $T = 7\,\mathrm{s}$), differences are observed between both numerical cases (NM1 and NM2). At that particular frequency, the difference between the NM2 and AM2 is a maximum, but NM1 and NM2 are almost equal. This might be due to resonance in the device.

Test	E_{NM2}/E_{NM1}	E_{AM2}/E_{NM1}	E_{AM2}/E_{NM2}
$H = 0.5\,\mathrm{m}$, $T = 3.5\,\mathrm{s}$	0.3879	0.4763	1.1902
$H = 1\,\mathrm{m}$, $T = 6\,\mathrm{s}$	0.6146	0.4803	0.7748
$H = 1.5\,\mathrm{m}$, $T = 7\,\mathrm{s}$	1.0522	0.4821	0.4462
$H = 2\,\mathrm{m}$, $T = 8\,\mathrm{s}$	0.8204	0.4716	0.5748

Table 5.4: Ratio between estimated energy output obtained using dry numerical, humid numerical, and real analytical models.

Energy extraction by the device reaches a maximum at a frequency of about 0.9 Hz, as observed by Medina-Lopez *et al.* (2017–II). Maximum energy extraction for the device analysed (same geometrical and sea conditions as presented in previous chapters) is observed at about $kh = 0.4$, which corresponds to a period of $T \simeq 7\,\mathrm{s}$. In the resonance case, other phenomena can probably be ignored. However, at frequencies away from resonance the real gas model is more relevant.

The energy ratio between the analytical model and model NM1 (dry case) is very stable, and is independent of wave conditions. The radiation–diffraction coefficients and the pressure drop change for every test, and so it is very likely that the underestimation of the real gas analytical model of about 50% of model NM1 can be taken as a valid approach for the behaviour of the device under saturation conditions.

This matches findings from the preliminary experiments, where the power for the turbine tested under humid air conditions fell to an asymptotic value of about 40% (see figure 2.12. Note that figure 2.12 is repeated as figure 5.17 here for easier

observation). It should be noted that tests in Fluent® were run for saturated conditions, $RH = 1$). In figure 2.12, the ratio between power under humid conditions and power in dry air conditions is plotted as a function of the relative humidity. Results from the experimental work apply to the specific laboratory conditions, but the similarity with the real gas model results gives confidence in the method.

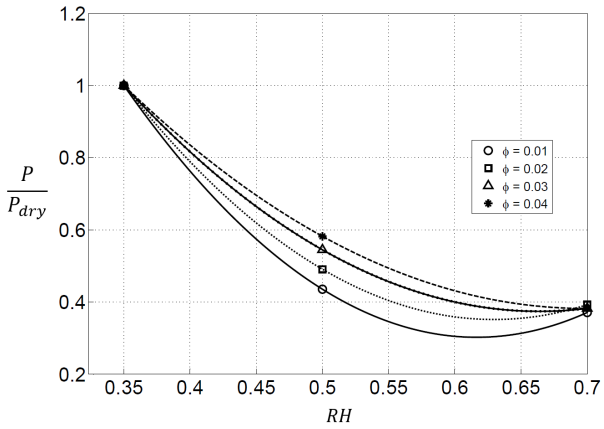

Figure 5.17: Power input ratio (humid air power over dry air power) as a function of relative humidity. [Source: Medina-Lopez *et al.* (2016)]

5.4 Discussion and conclusions

Real gas theory has been applied to the OWC formulation proposed by Sheng *et al.* (2013), and modified expressions derived for inhalation and exhalation of the air flow. It is shown that differences between the ideal and real gas models can reach 6% without any considerations in wave–structure interaction. The present analysis should be particularly useful to engineering practitioners involved in the design of oscillating water columns, and may have more general application to turbines through which water vapour–dry air mixtures pass.

A new equation has been derived for pressure inside the OWC that takes into account radiation and diffraction phenomena, following the methodology proposed by Martins–Rivas & Mei (2009–I). The equation is implicit, as it depends on the adiabatic index, which depends on pressure values. The system was solved numerically, and different OWC geometries were tested. For the inhalation part

of the cycle, the results are practically relevant, and a discrepancy is obtained in efficiency between this and the ideal gas formulation. However, for the exhalation part of the cycle, the efficiency values are the same using ideal gas. In other words, the exhalation phase can be simplified as in the ideal gas theory, but in the inhalation phase noticeable differences are expected between ideal and real gas theory. Moreover, it was observed that when a double linearisation is undertaken in terms of density and pressure, the new equations obtained for pressure during the inhalation phase are identical to those from ideal gas theory. This is because of the changing nature of the real gas adiabatic coefficient. Variations in time of the adiabatic index disappear when linearisation is done twice. In the ideal gas model, this is a result of linearising density with pressure from the very beginning.

A set of tests with different molar weights (MW) was run to analyse the sensitivity to changes in this parameter. Results showed that both surface elevation and pressure behaviour inside the OWC, as well as surface elevation motion along the flume were identical for the three molar weights tested (MW = 33, 21.4, and 18 g/mol). A sensitivity analysis in terms of specific heat at constant pressure was also performed, testing $C_p = 1500\,J/K \cdot kg$, $C_p = 1000\,J/K \cdot kg$, and $C_p = 900\,J/K \cdot kg$, and maintaining the other characteristics unchanged. Variations in surface elevation were lower than 1% in all cases. The same procedure was applied to density, *i.e.* $\rho = 1.2\,kg/m^3$, and $\rho = 1\,kg/m^3$. Variations were negligible.

However, the tests are very sensitive to combined variations of the three properties (density, molar weight, and specific heat at constant pressure). This fact is relevant because when the virial model is applied, both compressibility factor Z and density ρ remained very close to the ideal gas values. However, the specific heat at constant pressure, C_p, presented big variations with small changes in relative humidity and temperature. This altered the adiabatic index n because it is directly related to C_p. But the most important finding here is that these variations in C_p and consequently in n make the polytropic process equation, $pv^n = constant$, change. A lower value of C_p makes the initially assumed adiabatic process equation behave in a state in between adiabatic ($n = 1.4$) and isothermal ($n = 1$).

This result is very interesting, because in literature related to the filling process of vessels with gas products, Beater (2007) describes the behaviour of air inside the

chamber of the different systems analysed as somewhere between adiabatic and isothermal. This fact is also supported by the final results, where more adiabatic behaviour is observed for lower wave heights, whereas for higher waves the OWC behaviour falls farther from the adiabatic hypothesis. Specific heat changes are directly related to inter–molecular interaction and are represented in this case, through the virial model. The sensitivity analysis performed by changing each of the gas properties separately and obtaining very small discrepancies, shows that it is very important to be consistent when modifying the properties of the gas in order to obtain accurate results. Humidity considerations modify the gas in terms of mass (by modifying the gas density and molar weight), but also in terms of energy (by modifying the specific heat, and the process equation).

The changing nature of the adiabatic coefficient n implies that the system presents some type of hysteresis related to the process with compression following an adiabatic curve, and expansion following a different one. As adiabatic curves within the same p–V diagram do not intersect, the system is then moving in the third dimension: temperature. The hysteresis is related to the system changing to a different temperature than that at the end of the adiabatic process. During a period of time between two adiabatic processes, heat exchange with the ambient might be allowed, changing the overall temperature of the system. Then, the p–V–T conditions of the plane where the adiabatic belonged initially would have changed. The concept can be observed in figure 5.18. The different adiabatic curves available are plotted in green in the left figure. In defining the cycle within the OWC, it is assumed there is a compression process and an expansion process, probably linked by two processes at constant temperature: condensation and evaporation. The hysteresis of the processes makes consecutive cycles inside the chamber move in the p–V–T space. This hysteresis might be caused by differences between consecutive adiabatic processes within a compression–expansion cycle.

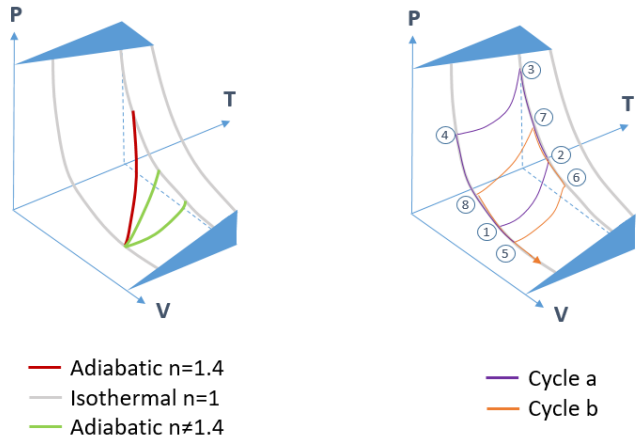

Figure 5.18: Pressure–volume–temperature (p–V–T) diagrams showing different types of curves analysed in this thesis (left), and different cycle paths inside the OWC chamber (right).

When comparing the numerical results with those from the analytical real gas model, several differences are present. Firstly, the analytical real gas model does not produce the expected phase discrepancies. This phase difference might be caused by the initial pressure values taken for iteration, and is worth further investigation. From the point of view of the discrepancies expected from the numerical tool, Fluent® applies an ideal gas model for a mix of dry air and water vapour. The analytical model developed in this thesis applies a real gas model for a gas between dry air and water vapour. The behaviour of the real gas model is expected to be more accurate than a mix of two ideal gases, as it is representing inter–molecular forces and heat exchange. Then, the differences between the humid numerical model and the real gas model are to be expected.

The ratio between energy extraction for different cases, calculated as the ratio between areas under the power curves in figure 5.15, is about 70 % between humid air (NM2) and dry air (NM1) numerical models, and about 50 % between analytical real gas model (AM2) and dry air numerical model (NM1), on average. In other words, the ratio between the energy between model AM2 and the energy in model NM2 is about 80 %. This can be applied at frequencies different from that of resonance of the device, where both numerical models are almost equivalent. However, the ratio between the analytical real gas model and the dry air numerical

model is almost constant and about 50 % for every case studied. At the resonance frequency, the differences between real and ideal gas approaches should be analysed further.

Chapter 6

Conclusions and recommendations

The goal of this thesis is to develop a formulation to include the effects of humidity on the performance of an OWC. To this end, an analytical model has been developed for a real gas inside the OWC chamber. This model has been validated using experimental data from a linear turbine situated in a wind tunnel, under different degrees of humidity in air. Moreover, a numerical 2D flume has been set up to simulate the OWC behaviour. The wave generator has been validated using experimental data from a wave flume, and the numerical model of the turbine has been validated with experiments of a Wells turbine developed in a wind tunnel. This flume has been tested under dry air and humid air conditions, both ideal gases. Finally, the analytical real gas model has been coupled with the radiation–diffraction theory, and compared with the numerical tests under different humidity conditions. This methodology presented an overall reduction of about 50 % of the estimated power for ideal gas when real gas and wave–structure interactions are taken into account. This thesis was motivated by work developed by the author during her Masters thesis, Medina-Lopez *et al.* (2016), where a considerable reduction in power occurred when humidity was inserted in the air flow inside a linear turbine. The main findings of the present thesis are summarised below.

6.1 Conclusions

6.1.1 Analytical model

- A new expression is developed for the adiabatic index n of a real gas. The resulting index changes linearly with temperature and pressure variations. For water vapour, the range of n values is close to but below 1.4.
- Modified expressions have been derived for the specific heat coefficients, entropy, internal energy, enthalpy, chemical potential, and speed of sound, all of which apply to a real gas. The real gas is less energetic than the ideal gas.
- Further analysis has shown that specific heat at constant pressure is very sensitive to the value of pressure in each step of the process.
- Although the derived adiabatic index is variable, the polytropic equation remains constant, as volume also changes with the real gas formulation.
- The initial hypothesis of reversibility is shown not to be entirely valid because of entropy changes in the OWC system. However, this might be caused by two phenomena: by a succession of adiabatic reversible processes with different adiabatic index n, making the entropy of the overall system grow; or by the irreversibility of the processes themselves.
- The real gas formulation exhibits improved agreement with laboratory measurements of turbine performance with humid air than the ideal gas formulation.
- For a hypothetical sinusoidal single pulse of pressure, where air flow and pressure are in phase, differences between the real gas model and ideal gas model results reach 6%.
- An equation has been derived for pressure inside the OWC taking into account radiation and diffraction phenomena. This equation is equivalent to that presented by Martins–Rivas & Mei (2009–I), but considering a real gas instead of an ideal gas. The behaviour of the OWC chamber changes because of the real gas nature, inducing a different response to the compression–expansion cycle produced by the water movement. That difference in the

response of the chamber changes the radiation pattern, modifying the OWC performance.

- The real gas model has been tested with different OWC geometries. During the inhalation part of the cycle, a difference in efficiency between the real gas approach and the ideal gas formulation is observed. For the exhalation part of the cycle, power extraction values are the same as in the ideal case.

- It is observed that when a double linearisation in terms of density and pressure is implemented, the resulting equations obtained for pressure during the inhalation phase are identical to those from the ideal gas theory. This double linearisation neglects changes in the type of process and nature of the gas (such as those induced by the real gas model).

- When the hypothetical sinusoidal pulse approach is analysed together with the radiation–diffraction problem (Martins–Rivas & Mei (2009–I)), it is confirmed that a 6% drop occurs between ideal and real power.

- This 6% drop value is expected to increase when an actual set of waves is simulated, because the real gas modifies the damping coefficient inside the OWC chamber and subsequently, the radiation phenomenon. This changes the wave–structure interaction pattern, causing the OWC efficiency to drop.

- Results depend on changes in the radiation coefficients, but are independent on the value of the diffraction coefficient. This is induced by the definition of these phenomena: radiation is affected by changes inside the OWC chamber, while diffraction studies the interaction wave–structure.

6.1.2 Numerical model

- The behaviour of a Wells turbine has been simulated numerically with an Actuator Disk Model (ADM). A set of tests in a 2D numerical flume is developed in Fluent®.

- The linear response of the turbine has been calibrated using experimental data, noting that the initial resistance of the physical turbine could not be modelled by means of an ADM.

- The numerical model has been tested with different sets of regular waves, and the linear response has shown to be independent of the wave conditions.

- Numerical tests considering ideal air with characteristics equivalent to those of humid air were performed. This way, the theoretical real gas model linked to the radiation–diffraction problem can be compared with a numerical approximation to the behaviour of humid air inside an OWC working under wave variations.

- For different sets of regular waves, the pressure drop and air flow inside the OWC chamber are smaller for the humid cases than for the dry air cases. This implies lower power available to the turbine.

- Density, specific heat at constant pressure, and molar weight were modified in the numerical model in Fluent® in order to account for humidity. However, viscosity was not changed. At the lower wave height ($H = 0.5\,\mathrm{m}$), values of water surface elevation near the generation paddle are found to be different for the humid air model and dry air model. In all other cases, values of surface elevation near the generation paddle are the same. For waves of low height, a rigorous calculation of viscosity should be made in the future, because viscosity effects become more pronounced in low amplitude waves.

- Results were found to be independent of changes in specific heat at constant pressure, density, or molar weight, when these are modified separately. However, when the three parameters are modified in tandem to represent a certain humidity content, results in surface elevation, pressure, and air flow inside the OWC changed consequently. Humidity modifies the gas in terms of mass (by changing density and molar weight), but also in energetic terms (by modifying specific heat and process equation).

- Large discrepancies in power at the OWC turbine are obtained between humid numerical model and dry numerical model, with the humid results of lower magnitude. For the most extreme peaks, differences up to 60% are obtained, whereas for the close peaks, differences around 90% are observed.

- The numerical model was tested for different seabed morphology patterns following the wave conditions from Playa Granada (Spain), presenting lower efficiencies when the modified seabed is taken into account. Bedform

dimensions have a strong influence in water flow circulation patterns. These directly influence OWC performance by modifying the incoming flow, and thus changing the pressure–air flow behaviour in the turbine. Local seabed conditions around devices should be studied in future plans for OWC potential locations in order to estimate accurately the device performance and efficiency.

6.1.3 Comparison between analytical and numerical models

- By comparing numerical test results with those from the analytical real gas model, it is found that the analytical model underestimates power values by about 20% on average with respect to the numerical humid air model. It should be noted that the numerical model represents an ideal gas.
- Despite discrepancies in generation patterns for small wave heights (due to viscous effects, as explained earlier), the real gas model provides a better agreement for small amplitude wave conditions. The real gas nature is more relevant to small waves, because pressure differences are less representative in such cases. The nature of the gas and viscous effects are more relevant when the wave height decreases.
- In terms of cumulative energy, the results from the numerical humid air model and analytical model are in very good agreement for the smaller waves, whereas discrepancies become evident for larger waves.
- Fluent® applies an ideal gas model for a mixture of dry air and water vapour. The analytical model developed in this thesis applies a real gas model for the so called "humid air". Note that, as discussed previously, Fluent® has tools to simulate real gas models, but these cannot be used when another fluid is present in the same problem, or for vapour that is not superheated, and so are not of use for the purpose of this thesis. Then, discrepancies between numerical and analytical models are to be expected.
- Discrepancies are found between the numerical humid air model and the analytical real gas model, because the analytical real gas model offers a more extensive approach to the behaviour of a real gas. Fluent® does not

take into account inter–molecular forces, or interactions between particles that are present in the real gas model. In other words, Fluent® applies the same method outlined in Chapter 2. The results are in partial agreement with laboratory measurements, according with the motivation of this thesis. Hence, the real gas model results are expected to be more accurate than those observed when simulating humidity in the numerical model.

- For small–amplitude waves of short periods, the results from both the numerical humid air model and the analytical real gas model are in very good agreement. However, as the wave height and period increase, the results show that the numerical humid model and the analytical real gas model differ. The biggest difference between the analytical and numerical model results appears for $T = 7\,\mathrm{s}$, occurring close the resonance period. In that event, both numerical models (dry and humid air) give almost the same results. Due to resonance effects, it is possible that the nature of the gas inside the OWC is not relevant when the device is in perfect synchrony with the incoming waves. However, the power produced by the real gas model is always about 50 % of that predicted by the ideal gas theory, independent of the wave conditions. Away from the resonance period, the discrepancies between the results from the numerical humid air model and the analytical real gas model are smaller.

- For each set of wave conditions analysed, the real gas model estimates the available energy to the turbine somewhere between 47% and 49% of the expected ideal energy. This matches the findings of the initial experimental work, where the power for the turbine tested under humid air conditions falls to an asymptotic value of 40% (see figure 5.17).

- For a hypothetical pulse of pressure inside the chamber, the drop in power is about 6%, whereas for the numerical tests considering the full OWC, the drop is about 48%. The first result is lower because the single pulse of pressure is perfect, and is in phase with the air flow, maximizing power. This condition is not present in the numerical simulation, which represents the wave–structure interaction, inserting a phase difference between pressure and air flow. Note that this condition is not present in actual devices.

- Power losses observed in OWCs currently tested (The Carbon Trust (2005))

could be explained by the real gas model. By applying the real gas model in an optimal OWC design (*e.g.* if pressure and air flow were in phase, and the OWC air chamber was thermally isolated), the minimum power loss would be about 6% of that provided by the classical formulation. For the actual estate of development, power could reach 48% of that expected by the classical theory. This is very important because, hypothetically, losses could be reduced up to 6% by optimising the device control system to match pressure with air flow, and by thermally isolating the OWC chamber to control temperature and humidity conditions.

6.2 Limitations of the study and recommendations for future research

The theoretical model in Chapter 3 was developed using the virial formulation, selected by the author from a range of options. It should be noted, however, that any other real gas model such as the Peng–Robinson model, Wohl model, or Beattie–Bridgeman model, Cengel & Boles (2015), could have been used for the purpose of this thesis. A sensitivity analysis of different real gas models should be performed in the future for comparison purposes. Moreover, this would enable analysis of the sensitivity of the results to the choice of real gas model.

The real gas model has been validated for a limited range of pressure ($p \in [p_{atm}\,, p_{atm} + 400\,Pa]$) and temperature values $T \in [20\,, 24]^{\circ}C$), as presented in Chapter 3. The theory might not be applicable to values out of these ranges. This should be examined in future studies.

This thesis has found that the power output of an OWC depends on the values of specific heat at constant pressure, and density. The specific heat at constant pressure represents the heat required to be added to a system in order to increase its temperature by one unit. For each step of the inhalation–exhalation process of the OWC chamber, a different value of specific heat and density was calculated herein. The variation of this parameter should be studied in more detail, because its value would depend on the real gas model chosen in the model. The energetic content in a portion of humid air depends on its heat exchange capacity, and mass. The energy contained in the air linked to its mass is the primary factor that reduces the overall efficiency of the OWC device. Other effects, such as changes in

the angle of attack of air on the turbine, or condensation and evaporation effects on the turbine blades, should be analysed in future studies. An understanding of all these phenomena linked together should lead to a much better estimate of the actual power produced by an OWC.

Numerical tests were performed with regular waves, which provide a simple analogy to a sea state. The model should be tested under a more complete set of tests with irregular waves.

The numerical tests were performed using a 2D model. Although such an approach is useful to analyse the main phenomena acting on an OWC device, a 3D model is recommended in the future for a more accurate study. A 3D model will allow a better observation of diffraction and radiation changes induced by the changes in humidity.

The tests in Fluent® were developed for inviscid flow. Such an approach is valid when inertial forces tend to dominate over viscous forces. From the results presented in this thesis, it is clear that when humidity is taken into account, the viscosity of the fluid might change, and then the viscous effects should be included in order to achieve a closer approximation to real conditions. The phase differences in pressure might be explained by this phenomenon. Tests should be run under the laminar conditions, to analyse the relevance of viscous effects. Moreover, turbulent conditions should also be analysed in the future to check the accuracy of tests under non–turbulent conditions. The computational cost will be higher, but the results will be more reliable.

The model used in Fluent® to simulate humid air considers a mix of dry air and water vapour, both behaving as ideal gases. Such a mixture of ideal gases is not equivalent to a real gas, as considered in this thesis. The real gas model takes into account inter–molecular interactions that lead to changes in the processes involved. To model accurately the humid air phenomena, a real gas model for gases at low temperatures should be implemented to be run in a numerical flume with water–air interaction.

A numerical model that takes into account the nature of the real gas at low temperatures could be developed using an open source platform, such as OpenFOAM.

At present, a real gas model can be tested in Fluent®, but under restricted conditions: a single–phase problem and superheated vapour (*e.g.* in this case, water vapour over 100°C). Having a numerical model that accurately simulates humid conditions for low temperatures and a range of low to high pressures would be a big step for future analyses of wave energy converters.

Moreover, a deep analysis of combined model that takes into account seabed morphology changes and humidity conditions should be implemented to estimate the total losses caused by both phenomena.

A complete experimental model under controlled humidity and temperature conditions should be developed and tested. This would represent a very important advance, given the lack of relevant thermodynamic measurements available. Prototype plants are an optimal solution for the lack of laboratory data. Measurements of temperature, humidity, pressure, and velocity inside the chamber are relatively easy to acquire, and a key prerequisite to the accurate estimation of OWC performance. It would allow the analysis of the p–V–T diagrams of an actual OWC, and the study of condensation and evaporation effects inside the OWC chamber. Moreover, the reversibility of the processes inside the OWC chamber should be studied.

6.3 Final notes

The real gas formulation offers a first step towards the accurate estimation of the working conditions of OWC devices. Experience has shown that power expectations do not match actual measurements, owing to the lack of any study to date, to the author's knowledge, of the interaction between thermodynamic, mechanical, electrical, and wave–structure related phenomena concerning an OWC. An accurate analysis would bring all of these factors together, providing a holistic understanding of the device performance.

Such analysis should be linked to predictions of seabed morphodynamics, and device–coastal interaction, which would inform array modelling. The interaction with the environment is a key factor to predict accurately the operational conditions of OWC devices in the mid–term. This step would take models closer to the simulation of real devices.

Although reaching the Levelised Cost of Energy (LCOE) provided by other ocean energy technologies, such as tidal devices, is still difficult, a complete analysis of the OWC system linked to the development of more functional devices, will make this technology more affordable, increasing its competitiveness. The bedform–coastal–device interaction, linked to the OWC chamber thermal isolation, and the device control system optimisation would be a good strategy for the OWCs of the future.

References

Abanades J., Greaves D. & Iglesias G., 2014. *Wave Farm Impact on the Beach Profile: a Case Study.* Coastal Engineering, Vol. 86, pp. 36–44. The impact of a wave farm on the beach profile is examined through a case study, based on two coupled numerical models: a nearshore wave propagation model and a morphodynamic model, which are run both with and without the wave farm.

Anaconda Project, 2017. `http://www.waveenergyscotland.co.uk/programmes/details/novel-wave-energy-converter/anaconda-novel-wave-energy-converter/`. Accessed on July 25th 2017.

Aquamarine's Oyster, 2017. `http://www.emec.org.uk/about-us/wave-clients/aquamarine-power/`. Accessed on July 25th 2017.

AquaRET Project, 2012. `http://www.aquaret.com`. Accessed on June 30th 2017.This is an e-learning tool promoting aquatic renewable technologies. The tool shows how these technologies work, where and how they fit into the landscape, and how they benefit the economy.

Archimedes Wave Swing, 2017. `http://www.awsocean.com/`. Accessed on July 25th 2017.

Baquerizo A., 1995. *Reflexión de Oleaje en Playas. Métodos de Evaluación y Predicción.* Tesis Doctoral.Universidad de Cantabria. In this thesis, the propagation of waves along the coastline is studied. Reflection and breaking–wave–induced–dissipation phenomena are considered. A new method to evaluate reflection is proposed, by separating incident and reflected waves.

Beater P., 2007. *Pneumatic drives.* Springer. 325 p.p. Library of Congress Control Number: 2006939785. This book presents a complete subject on pneumatic drives, starting from compressed air and thermodynamic properties, studying valves and finishing with digital control methods for pneumatic systems.

Benslimane S., 2013. *Experimental Study of the Effect of Blade Sweep on the Performance of Wells Turbine.* Internal Report. University of Granada. 16 pp. A study on the effects of

different types of blades, their angle on the flow around a Wells turbine and its performance is presented.

Benslimane S., 2014. *Test Wells Turbine.* Internal Report. University of Granada. 2 pp. This report presents a set of tests developed in a wind tunnel with a Wells turbine.

Bergillos R. J., López-Ruiz A., Ortega-Sánchez M., Masselink G. & Losada M.A, 2016 *Implications of delta retreat on wave propagation and longshore sediment transport - Guadalfeo case study (southern Spain).* Marine Geology, Vol. 382, pp. 1–16. The effects of delta retreat due to river damming on coastal processes are analysed here. The erosion generated in the delta is found to be propagated towards the east of the mouth. Longshore sediment transport was modified by both delta retreat and wave directionality, and it was found to be the main driver of the nearshore changes in the delta.

Bergillos R. J., Masselink G., McCall R.T. & Ortega-Sánchez M., 2016 *Modelling overwash vulnerability along mixed sand-gravel coasts with XBeach-G: Case study of Playa Granada, southern Spain.* Proceedings of the 35th International Conference on Coastal Engineering. This work aims to calibrate the XBeach–G model on a mixed sand–gravel deltaic coast (Playa Granada, southern Spain) and apply it to address the overwash vulnerability. A calibrated wave propagation model (Delft3D–WAVE) is used to obtain the inshore conditions required to drive the XBeach–G model. Results show how the application of XBeach–G can be used to address issues of storm–induced coastal vulnerability on gravel–dominated coasts.

Biel Gayé, J., 1997. *Curso sobre el Formalismo y los Métodos de Termodinámica.* Editorial Reverte, ISBN: 9788429143447. 576 p. This book was developed following a course on Thermodynamics from the University of Granada (Spain). It contains a very wide set of Thermodynamic concepts and formulations, starting with the very basics, and reaching real gas models and binary dissolutions.

Bingham H. B., Ducasse D., Nielsen K. & Read R., 2015 *Hydrodynamic Analysis of Oscillating Water Column Wave Energy Devices.* Journal of Ocean Engineering & Marine Engineering, DOI 10.1007/s40722–015–0032–4. A 40-chamber I-Beam attenuator-type, oscillating water column, wave energy converter is analysed numerically based on linearised potential flow theory, and experimentally via model test experiments. The high-order panel method WAMIT is used for the basic wave–structure interaction analysis.

Cengel Y. A. & Boles M. A., 2015 *Thermodynamics. An engineering approach..* McGraw-Hill Education. 2015. ISBN 978-0-07-339817-4. The textbook brings further refinement to an approach that emphasizes a physical understanding of the fundamental concepts of thermodynamics, focused to an engineering point of view.

Creech A.C.W., 2009. *A three-dimensional numerical model of a horizontal axis, energy extracting turbine. An implementation on a parallel computing system.* PhD Thesis. School of Engineering and Physical Sciences, Heriot-Watt University, Scotland. An Actuator Disk

Model is used to simulate tidal turbines and the validation of the model for a variety of situations.

Cruz J., 2008. *Ocean Wave Energy. Current Status and Future Perspectives.* Springer–Verlag. 431 p.p.i.s.b.n.978 − 3 − 540 − 74894 − 6. This is a compilation of a number of contributions to give the reader a global overview on ocean energy conversion.

Davidson J., Giorgi S. & Ringwood V., 2015. *Linear Parametric Hydrodynamic Models for Ocean Wave Energy Converters Identified from Numerical Wave Tank Experiments.* Ocean Engineering, Vol. 103, pp. 31–39. A new ocean wave energy modelling methodology is developed, which combines the fidelity of CFD models with the computational attractiveness of BEM-type models.

el–Twaty A. I. & Prausnitz J. M., 1981. *Generalized Van der Waals Partition Function for Fluids. Modification to Yield Better Second Virial Coeffcients.* Fluid Phase Equilibria, 5, pp. 191–197. An empirical modification of the Van der Waals partition function is proposed to give an accurate prediction of the second virial coefficient. Results are presented for Argon an water.

Evans D. V., 1982. *Wave Power Absorption by Systems of Oscillating Pressure Distributions.* Journal of Fluid Mechanics, Vol. 114, pp. 481–499. General results are derived for efficiency of energy absorption of a system of uniform oscillatory surface. This results are based on linear wave theory, and present a clear analogy with a system for absorbing oscillatory rigid bodies.

Evans D. V. & Porter R., 1995. *Hydrodynamic Characteristics of an Oscillating Water Column Device.* Applied Ocean Research, Vol. 17, pp. 155–164. A wave energy device is considered that consists of a thin vertical surface-piercing barrier next to a vertical wall in finite depth water. Equations for hydrodynamic properties are given.

Falcão A. F. de O., 2002. *Control of an Oscillating Wave Energy Plant for Maximum Energy Production.* Applied Ocean Research, Vol. 24, pp. 73–82. A stochastic model is applied to devise an optimal algorithm for the rotational speed control of an OWC wave power plant equipped with a Wells turbine, and to evaluate the average power output of the plant.

Falcão A. F. de O., 2007. *Phase Control through Load Control of Oscillating Body Wave Energy Converters with Hydraulic PTO System.* Ocean Engineering, Vol. 35, pp. 358–366. This paper addresses the case of oscillating-body converters equipped with a high–pressure hydraulic power take—off mechanism that provides a natural way of achieving latching. A method of achieving sub–optimal phase–control is developed, based on the theoretical time–domain modelling of a single–degree of freedom oscillating body in regular and irregular waves.

Falcão A. F. de O., 2010. *Wave Energy Utilization: A Review of Technologies.* Renewable and Sustainable Energy Reviews, Vol. 14, pp. 899–918. The development of

wave energy utilization since the 1970s is presented. Several topics are addressed: the characterization of the wave energy resource; theoretical background; how a large range of devices kept being proposed and studied, and how such devices can be organized into classes; the conception, design, model–testing, construction and deployment into real sea of prototypes; and the development of specific equipment (air and water turbines, high–pressure hydraulics, linear electrical generators) and mooring systems.

Falcão A. F. de O., 2013. *R & D Requirements fro Fixed Devices*. WaveNet. Results from the Work of the European Thematic Network on Wave Energy. The WaveNet was set up as a European Commission Thematic Network to share understanding and information on the development of ocean energy systems. This report summarises many of the outputs of the network and is intended to serve as a useful reference point for those interested in the status and development of the technology, the challenges faced, and the potential for the industry. A specific section of the report is devoted to first generation devices (especially OWCs), on whose design, construction and operation some experience already exists.

Falcão A. F. de O. & Justino P. A. P., 1999. *OWC Wave Energy Devices with Air Flow Control*. Ocean Engineering, Vol. 26, pp. 1275–1295.A theoretical model is developed to simulate energy conversion, from wave to turbine shaft, of an OWC plant equipped with a Wells air–turbine and with a valve (in series or in parallel with the turbine) for air–flow control.

Fluent Inc., 2006. *Fluent 6.3 User's Guide - 7.19.6 User Inputs for Porous Media*. Fluent Inc., Centerra Resource Park, 10 Cavendish Court, Lebanon, NH 03766. 2501 p.p. This user's guide presents the features and characteristics of Ansys Fluent.

Gato L. M. C. & Falcão A. F. de O., 1984 *On the Theory of the Wells Turbine*. Transactions of the ASME, Vol.106, pp. 628–633. A theoretical investigation is presented in this paper concerning the aerodynamic performance of the Wells turbine, a self–rectifying, axial–flow turbine suitable for energy extraction from a reciprocating air flow. A two–dimensional analysis is developed, and expressions, based on potential flow, are derived for the blade shape maximizing the turbine efficiency.

Gato L. M. C. & Falcão A. F. de O., 1989 *Aerodynamics of the Wells Turbine: Control by Swinging Rotor Blades*. International Journal of Mechanical Science, Vol.31 (6), pp. 425–434. This paper describes a theoretical and experimental investigation of the aerodynamic performance of a version of the Wells turbine modified such that its rotor blades can be set at a varying angle. The results show that the modified turbine can provide a way of increasing the amount of energy produced from ocean waves by efficiently phase–controlling an oscillating water column type of device.

Gel'man L. I. & Smolkin Y. V., 1966. *On the Calculation of Adiabatic Processes in Real Gases*. Journal of Engineering Physics, Vol. 11, N^{a} 33, pp. 325–328. A methodology to calculate the adiabatic index of real gases is proposed. Although this short note provides a good starting point for the purpose of this thesis.

Gkikas G. D. & Athanassoulis D. A., 2014. *Development of a Novel Non-linear System Identification Scheme for the Pressure Fluctuation inside an Oscillating Water Column Wave Energy Converter Part I: Theoretical Background and Harmonic Excitation Case.* Ocean Engineering, Vol. 80, pp. 84–99. A novel non-linear system identification method for harmonic excitations is developed. The system under identification is the pressure fluctuation inside the OWC chamber.

Gonçalves M., Martinho P. & Guedes Soares C., 2014. *Wave energy conditions in the western French coast.* Renewable Energy, Vol. 62, pp. 155–163. This paper presents a numerical study of the wave energy distribution in the western French coast, aiming to characterize wave energy along the Atlantic coast of Europe. A generation model, WAVEWATCH III is used to generate waves for the entire North Atlantic basin.

He F. & Huang Z., 2014. *Hydrodynamic Performance of Pile–Supported OWC–Type Structures as Breakwaters: an Experimental Study.* Ocean Engineering, Vol. 88, pp. 618–626. Wave transmission through a pile–supported OWC structure is studied experimentally. A small opening in the top cover of OWC chamber models the power-take-off mechanism.

Hughes S. A., 1993. *Physical Models and Laboratory Techniques in Coastal Engineering.* World Scientific. 568 p.p. i.s.b.n. $981 - 02 - 1541 - X$. This book is about the art and science of physical modelling as applied in coastal engineering. The aim of the book is to consolidate and synthesize into a single text much of the knowledge about physical modelling that has been developed worldwide.

Ibrahim T. K. & Rahman M. M., 2010. *Effects of Operation Conditions on Performance of Gas Turbine Power Plant.* National Conference in Mechanical Engineering Research & Postgraduate Studies, 3–4 December, Faculty of Mechanical Engineering, UMP Pekan, Kuantan, Pang Malasya, pp. 135–144. This work presents the effect of operation conditions (compression ratio, turbine inlet temperature, air to fuel ratio and efficiency of compressor and turbine) on the performance of gas turbine power plant. The computational model was developed utilizing the MATLAB codes.

Jalón L, 2016. *Diseño óptimo de un sistema de aprovechamiento de la energía del oleaje y gestión integral a diferentes escalas de tiempo. Optimal design of a wave energy converter and integrated management at different time scales.* PhD Thesis. Universidad de Granada. The thesis analyses the optimal design for a wave energy converter, taking into account the random nature of the waves at different time0-scales ranging from sea state until a year.

Jalón M. L., Baquerizo A. & Losada M. A., 2016. *Optimization at Different Time Scales for the Design and Management of an Oscillating Water Column System.* Energy, Vol. 95, pp. 110–123. An optimization method is used to highlight the importance of time scales in the design of a bottom-fixed OWCs. The different time scales studied are a sea state, a season, and a year.

Javaherchi Mozafari A. T., 2010. *Numerical Modeling of Tidal Turbines: Methodology Development and Potential Physical Environmental Effects.* MSc Thesis. Master of Science in Mechanical Engineer. University of Washington. 158 pp. This Master's thesis describes a general numerical methodology consisting of three numerical models. After validation, the numerical methodology is applied to study a MHK turbine with realistic boundary conditions.

Jeffery E. R., 1984 *Simulation of Wave Power Devices.* Applied Ocean Research, Vol. 6, Nº 1, pp. 31–39.Classical frequency and time domain models of a single degree of freedom wave power device are presented. In the time domain, a convolution integral is used to represent the fluid dynamic radiation force, characterised by added mass and damping in the frequency domain. This integral is replaced by an approximate ordinary differential equation (ODE) model which is faster and more convenient in simulations.

Justino P. A. P. & Falcão A. F. de O., 1999. *Rotational Speed Control of an OWC Wave Power Plant.* Journal of Offshore Mechanics and Arctic Engineering, Vol. 121, pp. 65–70. The paper deals with the control of an oscillating water column wave energy plant, equipped with a Wells turbine driving a variable speed electric generator. Three different control strategies are described. Results of numerical simulations are presented for two of them, and are found to satisfy the prescribed requirements.

Korde U., 1991 *A Power Take–Off Mechanism for Maximizing the Performance of an Oscillating Water Column Wave Energy Device.* Applied Ocean Research, Vol. 13, pp. 75–81. A power take-off mechanism for controlling the hydrodynamic response of a full scale OWC device is proposed. A system comprising an air turbine, a float, and a hydraulic power conversion apparatus is proposed.

Krewitt W., Nienhaus K., Klessmann C., Capone C., Stricker E., Graus W., et al., 2009. *Role and potential of renewable energy and energy efficiency for global energy supply* Dessau-Roßlau: Federal Environment Agency (Umweltbundesamt). Dec. Report No.: (UBA-FB) 001323/E. The report emphasises that there still is considerable unexploited potential for renewable energy, energy efficiency as well as for behavioural changes to reduce future global energy-related CO2 emissions. The overall technical and behavioural potentials for renewable energy technologies and energy efficiency improvements are significant. Further development is needed for their exploitation, in particular for overcoming economical, infrastructural and political constraints.

Kreyszig E., 2006. *Advanced Engineering Mathematics, 9th edition. Wiley Editions.* i.s.b.n. $0-471-72897-7$. This is a book on advanced Mathematics and its computational applications.

Landau L., Ajiezer A. & Lifshitz E., 1988. *Curso de Física General. Mecánica y Física Molecular.* 3ª reimpresión. MIR. 398 pp. The main physical phenomena are presented with a simple methodology and application to every–day concepts.

Le Méhauté B., 1976. *An introduction to hydrodynamics and water waves.* Springer-Verlag. This book presents the basic and more advanced concepts for wave definition and generation.

Longo S., 2012 *Wind-generated water waves in a wind tunnel: Free surface statistics, wind friction and mean air flow properties.* Coastal Engineering 1 (61) (2012) 27–41. doi:10.1016/j.coastaleng.2011.11.008. Systematic measurements of wind and water waves in a wind tunnel with a water tank inside are presented in this paper. Velocity fields are measured using 2-D Laser Doppler velocimetry (LDV) in air and instantaneous water levels are measured using resistive twin-wire probes.

Longo S. & Losada M., 2012 *Turbulent structure of air flow over wind-induced gravity waves.* Experiments in Fluids 2 (53) (2012) 369–390. doi:10.1007/s00348-012-1294-4. This paper reports systematic measurements of wind–generated water waves in a wind tunnel experiment. Here, the structure of the boundary layer on the air side of the water—air interface was analysed and compared with the boundary layer over a smooth plane rigid wall.

López. I., Andreu J., Ceballos S., MArtínez de Alegría I. & Kortabarria I., 2013. *Review of wave energy technologies and the necessary power–equipment.* Renewable and Sustainable Energy Reviews, 27, pp. 413–434. A complete analysis of the wave energy technology is presented, starting with the characterisation of this global resource in which the most suitable places to be exploited are identified, and different types of wave energy converters are classified according to their features.

López. I. & Iglesias G., 2014. *Efficiency of OWC Wave Energy Converters: a Virtual Laboratory.* Applied Ocean Research, 44, pp. 63–70. Artificial neural networks (ANNs) are applied to OWC wave energy converters. This determines the efficiency of the OWC chamber. The new model takes into account wave conditions, tidal level and turbine damping. The model is trained and validated using results from an extensive experimental campaign.

López. I., Pereiras B., Castro F. & Iglesias G., 2014. *Optimisation of Turbine-Induced Damping for an OWC Wave Energy Converter using a RANS-VOF Numerical Model.* Applied Energy, 127, pp. 105–114. In this document, a RANS—VOF model of an OWC wave energy converter is implemented and validated. OWC performances for different wave conditions and damping values are studied.

López. I., Pereiras B., Castro F. & Iglesias G., 2015. *Performance of OWC Wave Energy Converters: Influence of Turbine Damping and Tidal Variability.* International Journal of Energy Research, 39, 4, pp. 472–483. This work analyses the influence of wave conditions, damping caused by the turbine and tidal level on the efficiency of the conversion from wave to pneumatic energy that occurs in the OWC chamber. To achieve this, a comprehensive experimental campaign has been carried out, involving in total 387 tests of a model OWC under varying wave conditions, damping coefficients, and tidal levels.

Malic R., 1955. *The Equation of Polytropic Process of Real Gases.* Journal of the The Franklin Institute, Vol. 259, issue 3, pp. 235–238. An equation for the polytropic process of real gases is derived, where the main changes are characterised by a term called the "internal" pressure. This equation applies to cases when the exponent n can be taken as a constant.

Mansard E. P D. & Funke E. R., 1987. *On the Reflection Analysis of Irregular Waves.* Natl. Res. Counc. Rev. Can. Hydraulics. Laboratory Technical Report, TR-HY-O17. This book comprises a comprehensive study on wave reflection, particularly in terms of methods to measure and accurately estimate it.

Martins–Rivas H. & Mei C. C., 2009. *Wave Power Extraction from an Oscillating Water Column at the Tip of a Breakwater.* Journal of Fluid Mechanics, Vol. 626, pp. 395–414. This work studies theoretically a single OWC installed at the tip of a long and thin breakwater. The linearised problems of radiation and scattering for a hollow cylinder with an open bottom are then solved by the usual method of eigenfunction expansions and integral equations.

Martins–Rivas H. & Mei C. C., 2009. *Wave Power Extraction from an Oscillating Water Column along a Straight Coast.* Ocean Engineering, Vol. 36, pp. 426–433. A linearised theory of an OWC installed on a straight coast is analysed. Results are compared with a parallel study of an OWC installed either offshore or at the tip of a thin breakwater.

McCall R. T., Masselink G., Poate T. G., Roelvink J. A., Almeida L. P., Davidson M. & Russell, P. E., 2014. *Modelling storm hydrodynamics on gravel beaches with XBeach–G.* Coastal Engineering, Vol. 91, pp. 231–250. A process–based model for storm hydrodynamics on gravel beaches is presented. Model results are compared to measurements at four field sites and one flume experiment. The model shows good prediction of wave transformation, run–up and initial over-topping.

McCall R. T., Masselink G., Poate T. G., Roelvink J. A. & Almeida L. P., 2015 *Modelling the morphodynamics of gravel beaches during storms with XBeach–G.* Coastal Engineering, Vol. 103, pp. 52–66. This paper presents a process–based model for storm morphodynamics on gravel beaches, which includes the effect of groundwater and acceleration terms on sediment transport. Model results are compared to measurements at four field sites and one flume experiment for ten separate storm events. The results show that XBeach–G can be applied to predict storm impacts on gravel beaches with reasonable to high confidence for a range of hydrodynamic forcing conditions.

Medina-Lopez E., Moñino A., Clavero M., Del Pino C. & Losada M. A., 2016. *Note on a Real Gas Model for OWC Performance.* Renewable Energy, Vol. 85, pp. 588–597. This paper studies the thermodynamics of a real gas flow in an oscillating OWC system. Moisture present in the air surrounding the OWC turbine modifies its performance. A real gas model is presented and experimental work is carried out to quantify the influence of humidity in OWC efficiency. A decrease in the expected power is shown depending on moisture and air flow. This paper is the starting point of the present thesis.

Medina-Lopez E., Moñino A., Borthwick A.G.L. & Clavero M., 2017. *Thermodynamics of an OWC containing real gas.* Energy, Vol. 135, pp. 709–717. The Thermodynamics of Oscillating Water Column (OWC) systems are examined. A real gas model is presented to analyse the real working conditions of an OWC. Humidity, pressure and temperature changes in the OWC chamber are considered. Validation of the real gas model is presented and compared with ideal gas theory. Differences up to 6% in efficiency between ideal and real gas models are observed. This paper presents the main core of the theoretical work developed in the present thesis.

Medina-Lopez E., Bergillos R.J., Moñino A., Clavero M. & Ortega-Sánchez M., 2017. *Effects of seabed morphology on oscillating water column wave energy converters.* Energy, Vol. 135, pp. 659–673. The effects of seabed Morphology on OWC systems are studied. A numerical model is presented to analyse the effects of bedform changes on OWCs. The model is developed in Fluent® and compared with a hypothetical flat seabed. The seabed is reproduced with XBeach-G® for sea states in Playa Granada (Spain). Energy dissipation relates to bedform volume, decreasing efficiency for evolved seabeds. This paper presents the numerical model used in this thesis.

Mendoza E., Silva R., Zanuttigh B., Angelelli E., Andersen T., Martinelli L., Nørgaard J. & Ruol P., 2014. *Beach Response to Wave Energy Converter Farms Acting as Coastal Defence.* Coastal Engineering, Vol. 87, pp. 97–111. New experimental results are presented on transmission coefficients beyond WECs, and WEC farms performance for coastal defence are evaluated for two study sites. All the WEC farms were found to cause beach accretion, at least in small areas.

Paixão Conde J. M., Teixeira P. & Didier E., 2011. *Numerical Simulation of an Oscillating Water Column Energy Converter: Comparison of Two Numerical Codes.* Proceedings of the XXI International Offshore and Polar Engineering Conference, Maui, Hawaii, June–2011, pp. 668–674. Results from the application of two numerical codes to the simulation of an oscillating water column wave energy converter are presented. One of the codes (FLUINCO) is based on the finite elements technique, while the other (FLUENT) is based on the finite volume technique.

Pelamis Project, 2017. `http://www.pelamiswave.com/`. Accessed on July 25th 2017.

Pitzer K. S. & Curl R. F., 1957. *The Volumetric and Thermodynamic Properties of Fluids. III. Empirical Equation for the Second Virial Coefficient.* Thermodynamic Properties of Fluids, Vol. 79, pp. 2369–2370. This paper presents an equation to calculate the second virial coefficient of a normal fluid. This equation fits the volumetric data and its second derivative yields agreement with measured values of pressure derivatives of the gas heat capacity.

Planck M., 1905. *Treatise on Thermodynamics.* Dover Publications Inc., 1905. ISBN-13: 978-0486663715. This book is a leading work on Thermodynamics. Most of the main concepts used nowadays are introduced in this document.

Ocean Power technologies, 2017. http://www.oceanpowertechnologies.com/powerbuoy-technology/. Accessed on July 25th 2017.

Prausnitz J., Lichtenthaler R. & Gomes de Azevedo E., 1999. *Molecular Thermodynamics of Fluid–Phase Equilibria.* Prentice–Hall. 864 pp. i.s.b.n. 0−13−977745−8. A broad introduction to thermodynamics of phase equilibria is presented.

Price T. J., 2005. *James Blyth: Britain's first modern wind power pioneer.* Wind Engineering, 29–3, pp. 191–200. This paper investigates Professor Blyth's life, examining his motivation to generate electricity from wind and his association with contemporaries, including Lord Kelvin. The paper argues that it was Blyth and not the American Charles Brush, who was the first to produce wind–powered electricity.

Puertos del Estado, 2016. https://www.puertos.es/. Accessed on February 2nd 2017.

Raghunathan S., 1995. *The Wells Turbine for Wave Energy Conversion.* Prog. Aerospace. Sci., Vol. 31, pp. 335–386. This extensive paper provides a comprehensive summary of research on Wells turbines.

Reikard G., Pinson P. & Bidlot J.R. 2011. *Forecasting ocean wave energy: the ECMWF wave model and time series methods.* Ocean Engineering, Vol. 38, pp. 1089–1099. The forecasting properties of a well-known physics-based model, the European Center for Medium-Range Weather Forecasts (ECMWF) Wave Model, are analysed, and two statistical techniques, time–varying parameter regressions and neural networks.

Sarmento A. J. N. A. & Falcão A. F. de O., 1985. *Wave Generation by an Oscillating Surface–Pressure and its Application in Wave–Energy Extraction.* Journal of Fluid Mechanics, Vol. 150, pp. 467–485. A two-dimensional analysis, based on linear surface-wave theory, is developed for an oscillating-water-column wave-energy device in water of arbitrary constant depth. Both the cases of linear and non–linear power take–off are considered. The results show that air compressibility can be important in practice, and its effects may in general be satisfactorily represented by linearisation.

Sarmento A. J. N. A., Gato L. M. C. & Falcão A. F. de O., 2003. *Turbine–Controlled Wave Energy Absorption by Oscillating Water Column Devices.* Coastal Engineering, Vol. 17, N^o 5, pp. 481–497. The paper deals with phase control as a method of increasing the energy absorption by OWC devices, from regular as well as from irregular waves. Results of numerical simulations are presented for three different control strategies applied to energy absorption from irregular waves by an OWC device of simple, two-dimensional geometry.

Serhadlioğlu S., Adcock T., Houlsby G., Draper S. & Borthwick A.G.L., 2013. *Tidal stream energy resource assessment of the Anglesey Skerries.* International Journal of Marine Energy, 3–4, e98–e111. This study analyses the effects of tidal

stream power devices off Anglesey (UK). A two–dimensional depth–averaged shallow water model of the tidal dynamics of the south-west UK and Irish Sea is developed and used to investigate disturbance to the local flow field due to the operation of tidal arrays, and also to evaluate the extractable power at the site. In the model, upstream and downstream heads are related by Linear Momentum Actuator Disk Theory.

Sheng W., Alcorn R., & Lewis S., 2013. *On Thermodynamics of Primary Energy Conversion of OWC Wave Energy Converters.* Renewable Sustainable Energy, 5, 023105. An investigation to the thermodynamics of air flow in the chamber of an oscillating water column wave energy converter is done, in which the oscillating water surface in the water column pressurizes or de-pressurises the air in the chamber. The research is focused on ideal gas formulation.

Singh S. & Kumar R., 2012. *Ambient Air Temperature Effect on Power Plant Performance.* International Journal of Engineering Science & Technology, Vol. 4, N^{a} 8, pp. 3916–3928. This paper analyses the effect of the ambient air temperature on various parameters of power plant, such as mass flow rate of air, fuel consumption, steam, power output of turbine, efficiency and heat rate of gas turbine, steam turbine and combined cycle plant.

SI Ocean Energy Project, 2014. *Ocean Energy: Cost of Energy and Cost Reduction Opportunities.* Strategic Initiative for Ocean Energy. `http://www.si-ocean.eu/en/Home/Home/`. The Strategic Initiative for Ocean Energy (SI OCEAN) aims to provide a coordinated voice for the ocean energy industry in Europe and to deliver practical recommendations to remove barriers to market penetration. This report investigates the cost of energy from early arrays, and predicts how this is likely to reduce over time.

Stefanakos C.N., Athanassoulis G.S.,Cavaleri L, Bertotti L. & Lefevre J.M., 2004. *Wind and Wave Climatology of the Mediterranean Sea. Part II: Wave Statistics.* Proceedings of the Fourteenth International Offshore and Polar Engineering Conference, Toulon, France, May 23-28. The work presented in this conference paper is part of the WW MEDATLAS project, whose aim is the edition of a Wind and Wave Atlas of the Mediterranean Sea, both in electronic and printed form.

Beattie J. A. & Stockmayer W. H., 1942. *The second virial coefficient for gas mixtures..* Journal of Chemical Physics, 10, pp. 473–476. DOI: 10.1063/1.1723750. The second virial coefficients B for methane, normal butane, and three mixtures of these gases are evaluated from experimental data.

Stull R.B., 2000. *Meteorology for scientists and engineers.* Pacific Grove, CA. This is a book on practical meteorology. It is written for students and professionals in science and engineering who are interested in basic concepts. Equations are converted into algebra for easier understanding.

Teixeira P., Davyt D., Didier E. & Ramalhais R., 2013. *Numerical Simulation of an Oscillating Water Column Device Using a Code Based on Navier–Stokes Equations.* Energy, 61, pp. 513–530. An onshore OWC device is analysed by using a Navier–Stokes code. An aerodynamic model is implemented to consider the presence of the turbine.

The Carbon Trust, 2005. *Oscillating Water Column Wave Energy Converter Evaluation Report.* Marine Energy Challenge. This report revises the current state of the art related to OWCs. It also analyses several prototypes and provides estimates of efficiency and performance which are very useful for comparison purposes.

Thiebaut F., Griffiths J., Pellat A., O'Sullivan D. & Alcorn R., 2010. *Servomotor Controlled Piston Rig for the Simulation of an Oscillating Water Column Air Chamber.* Third International Conference on Ocean Energy. October 2010, Bilbao, Spain. The engineering design and operational results of a test rig are presented in detail and compared with a basic thermodynamic analysis for validation and further understanding. These results cast a new light on flow and temperature measurement methods and on the use of an orifice for model testing.

Tsonopoulos C., 1974. *An Empirical Correlations of Second Virial Coefficients.* AlChE Journal, Vol. 20, N° 2, pp. 263–272. A new correlation of second virial coefficients of both polar and non–polar systems is presented. The method uses the Pitzer-Curl correlation for non–polar compounds, but in a modified form. The second virial coefficient is fitted satisfactorily to two additional parameters per compound for hydrogen bonding compounds (alcohols, water).

Tsonopoulos C. & Heidman J. L., 1990. *From the Virial to the Cubic Equation of State.* Fluid Phase Equilibria, Vol. 57, pp. 261–276. Second virial coefficients are used extensively in low-pressure vapour-liquid equilibrium calculations to predict the vapour–phase fugacity coefficient. Tsonopoulos's 1974 B (second virial coefficient) correlation is reviewed, with particular emphasis on the dependence of the polar parameter on the reduced dipole moment. New results for the B of water are analysed.

Uihlein A. & Magagna D., 2016. *Wave and tidal current energy – A review of the current state of research beyond technology.* Renewable and Sustainable Energy Reviews, Vol. 58, pp. 1070–1081. This review covers the current state of research in ocean energy. Particular focus is placed on research that extends beyond technology or technological improvements. This article also highlights areas where research gaps exist and where future research efforts should be directed.

United Nations Development Programme, Bureau for Development Policy, 2000. *Energy and the challenge of sustainability.* World Energy Assessment. New York. I.S.B.N. $92-1-126126-0$. The publication highlights the societal, economic, environmental and security issues linked to energy. It analyses how energy can serve as an instrument to reach the goal of sustainable human development. It concludes that adoption

of policies that encourage the delivery of energy services in cleaner and more efficient ways is a prerequisite to address development problems.

Van Bussel G.J.W., 2008. *Wind Energy On line Reader.* TU Delft University. `http://mstudioblackboard.tudelft.nl/duwind/Wind%20energy%20online%20reader/Video_frames_pages/actuator_disk_model.htm`. This Wind Energy On line Reader is a fully hyper–linked multimedia document that supports students of TU Delft, TU Eindhoven and U Twente in getting familiar with wind turbine technology. The on line reader has been developed through the 3TU cooperation framework to support the courses AE3-W02 at TU Delft; 4P720 at TU Eindhoven and 472012 at the University of Twente.

Wavedragon Project, 2017. `http://www.wavedragon.net/`. Accessed on July 25th 2017.

Whittaker T., 2003. *A two fluid numerical model of the Limpet OWC.* 5th European Wave Energy Conference, Cork, Ireland, 2003. pp 119 – 131. A CFD model to simulate the Limpet OWC in Scotland is presented.

Wisniak J., 2003. *Heike Kamerlingh–The Virial Equation of State.* Indian Journal of Chemical Technology, Vol. 10, pp. 564–572. This document describes the works of Heike Kamerlingh Onnes (1853-1926) on thermodynamics, the equation of state, and optical, magnetic, and electrical phenomena. Kamerlingh Onnes proposed the virial equation of state (a significant improvement over the one of van der Waals), extended the concept of corresponding states, investigated the behaviour of gases at very low temperatures, and discovered the phenomenon of superconductivity. He was awarded the 1913 Nobel Prize for Physics for his investigations on the properties of matter at low temperature, which eventually led him to liquefy helium in 1908.

Yang W. & Su M., 2004. *Influence of Moist Combustion Gas on Performance of a Sub-Critical Turbine.* Energy Conversion & Management Vol. 46, pp. 821–832. A model is introduced to calculate the thermodynamic properties of the moist combustion gas, and another model is formulated to calculate the performance of the turbine based on the one–dimensional flow equations. Using these models with the geometric parameters of the turbine fixed, at the design working condition, the performance of the turbine is calculated and analysed for different absolute humidities.

Wu J., 1990. *Are sound waves isothermal or adiabatic?.* American Journal of Physics Vol. 58 (7), pp. 694–696. In this letter to the editor, Prof Wu from the University of Vermont, presents certain interesting concepts concerning the properties of sound waves (which were misleading in some books). At high frequencies, Wu reports that sound waves are isothermal, whereas for low frequencies, they are adiabatic.

Appendices

Appendix I: OWC classic formulation

In order to set appropriately the context and the scope of the study, a brief review of the classic OWC formulation is presented, as defined by Martins–Rivas & Mei (2009–I). If a Wells turbine – or any linear response turbine – is used for the power take-off system, the mass flow rate Q_T^m through the turbine can be defined in terms of the pressure drop in linear form:

$$Q_T^m = \rho Q_T = \frac{KD}{N} p \,, \tag{1}$$

where K depends on turbine parameters, D is the turbine diameter, N is the turbine rotation velocity, and ρ is the air density inside the OWC chamber.

Substituting into equation (2.2), obtaining Q_{owc} taking into account equation (5.5), and operating:

$$Q_{owc} = \frac{KD}{N\rho} p + \frac{V}{C_s^2 \rho} \left(\frac{dp}{dt} \right) \,, \tag{2}$$

where C_s is the speed of sound in air.

Following Martins–Rivas & Mei (2009–I) and applying harmonic solutions, we obtain:

$$\widehat{Q}_{owc} = \frac{KD}{N\rho} \widehat{p} - i\omega \frac{V}{C_s^2 \rho} \widehat{p} \,, \tag{3}$$

where both $\widehat{Q}_{owc}$ and $\widehat{p}$ are complex amplitudes defined in the classic problem.

If as discussed before a steady–state flow is considered, the continuity equation simply reads:

$$Q_{owc} = \frac{KD}{N\rho} p \,, \tag{4}$$

with Q_{owc} and p defined as real quantities. In general terms, the power input to the turbine is expressed as:

$$P = p Q_{owc} \,. \tag{5}$$

Following Martins–Rivas & Mei (2009–I), the average power $\overline{P}$ extracted from

the pneumatic power inside the chamber is:

$$\overline{P} = \frac{1}{2}\frac{KD}{N\rho}|\widehat{p}|^2 = \frac{1}{2}\frac{KD}{N\rho}\frac{|\tilde{\Gamma}|^2(H/2)^2}{(\frac{KD}{N\rho}+\tilde{B})^2+(\tilde{C}+\frac{\omega V}{C_s^2\rho})^2}\,, \tag{6}$$

and the capture length, understood as an efficiency expression, is:

$$kL = \frac{8k\overline{P}}{\rho_w g H^2 C_g} = \frac{gka}{\omega C_g}\frac{\chi|\tilde{\Gamma}|^2}{(\chi+\tilde{B})^2+(\tilde{C}+\beta)^2}\,. \tag{7}$$

Coefficients $\tilde{B}$, $\tilde{C}$, $\tilde{\Gamma}$, χ and β are the mathematical representation of the oscillation damping, the restitution of the added mass, the flow in the chamber associated to with diffraction problem, and the turbine characteristics. H is the wave height, C_g is the wave group celerity, $g = 9.81\,m/s^2$ is the gravity acceleration, k is the wave number and a is the OWC radius.

Summarising:

$$\tilde{\Gamma} = \Gamma/\left(\frac{ag}{\omega}\right) \tag{8}$$

$$\tilde{B} = B/\left(\frac{a}{\omega\rho_w}\right) \tag{9}$$

$$\tilde{C} = C/\left(\frac{a}{\omega\rho_w}\right) \tag{10}$$

$$\chi = \frac{\rho_w KD\omega}{\rho N a} \tag{11}$$

$$\beta = \frac{\omega^2 V_0 \rho_w}{C_s^2 a\rho} \tag{12}$$

Appendix II: Air and water vapour properties

	Value	*Units*
Air properties		
R_a	286.7	J/kg· K
$C_{p,a}$	1010	J/kg· K
ρ_a	1.25	kg/m^3
M_a	0.0288	kg/mole
$T_{c,a}$	132	K
$p_{c,a}$	$37.71 \cdot 10^5$	Pa
Water vapour properties		
R_v	461	J/kg· K
$C_{p,v}$	1840	J/kg· K
M_v	0.0182	kg/mole
$T_{c,v}$	647	K
$p_{c,v}$	$220.89 \cdot 10^5$	Pa

Table 1: Dry air and water vapour properties.

Appendix III: Turbine performance coefficients

In general terms, the turbine performance is described by the following non-dimensional coefficients:

- Flow coefficient:
$$\Phi = \frac{V_x}{U}\,, \tag{13}$$
- Pressure drop:
$$p^* = \frac{\Delta p}{\rho w^2}\,, \tag{14}$$
- Solidity:
$$\sigma = \frac{A_a}{\pi(D/2)^2}\,, \tag{15}$$
where V_x is the axial velocity, $U = ND/2$ is the blade circumferential velocity, w is the relative incoming velocity, A_a is the total blades area.

In the following table, the turbine geometry specifications are given.

Property	*Value*
R_{int}	0.0055 m
R_{ext}	0.015 m
R_{med}	0.0102 m
D	0.03 m
Turbine area	$3.5906 \cdot 10^{-4}\ m^2$
c	0.0076 m
Number of blades	7
Blades area	$2.4271 \cdot 10^{-4}\ m^2$
σ	0.82

Table 2: Turbine geometry specifications.

Appendix IV: Basic theory of the Actuator Disk Model (ADM)

The actuator is an infinitely thin disk located perpendicular to the flow. This extracts pressure energy rather than kinetic energy, Creech (2009). As the fluid approaches the disk, the pressure increases upstream as the fluid velocity slow down, see figure 1.

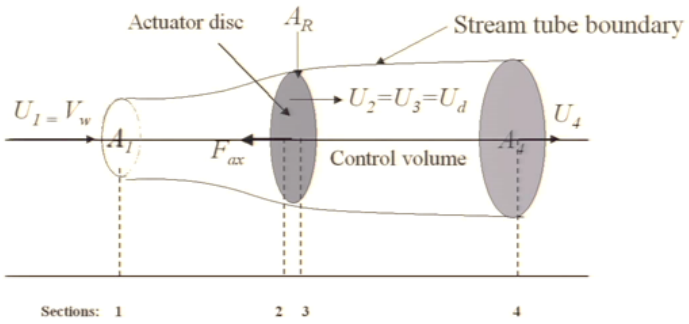

Figure 1: 3D Actuator Disk Model schematic.[Source: Van Bussel (2008)]

Inside the streamtube surrounding the disk the mass, momentum and energy conservation are applied. The flow assumptions are: homogeneous, incompressible and inviscid fluid, steady state flow and uniform flow conditions over the disk. So the three equations of conservation are:

$$\rho U A = \rho_1 U_1 A_1 = \rho U_d A_R = \rho U_4 A_4 = \dot{m} \tag{16}$$

$$\dot{m}\,(U_1 - U_4) = T + F_x \tag{17}$$

$$\dot{m} = \left(\frac{U_1^2}{2} - \frac{U_4^2}{2}\right) = T U_d \tag{18}$$

So, the induction velocity U_d can be obtained from equations 17 and 18 as the semi-sum of the inlet and outlet velocities, U_1 and U_4, respectively. The axial induction factor is:

$$a = \frac{u_i}{V_w} \tag{19}$$

where u_i is the axial component of the induction velocity U_d.

Hence, thrust and power can be defined as:

$$T = \rho V_w^2 2a(1-a)A_R \tag{20}$$

$$P = \rho V_w^3 2a(1-a)^2 A_R \tag{21}$$

and the thrust and power coefficients are as follows. A comparison between them can be seen in figure 2.

$$C_T = \frac{T}{1/2\rho V_w^2 A_R} = 4a(1-a) \tag{22}$$

$$C_P = \frac{P}{1/2\rho V_w^3 A_R} = 4a(1-a)^2 \tag{23}$$

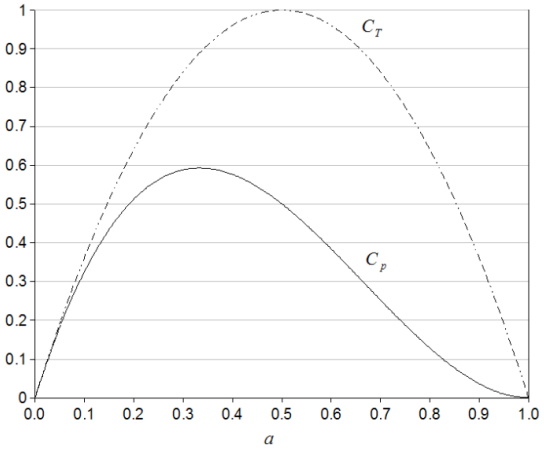

Figure 2: Graph of a in front of C_T and C_P.[Source: Creech (2009)]

List of Acronyms

OWC — Oscillating Water Column
WEC — Wave Energy Converter
ADM — Actuator Disk Model
LDV — Laser Doppler Velocimeter
CFD — Computational Fluid Dynamics
LCOE — Levelised Cost Of Energy

List of Symbols

a—OWC radius

a—Axial induction factor

A—Wave amplitude

A_0—Incoming wave amplitude

A—Actuator Disk Cross section

B—Second virial coefficient

$B' = B/M$—Second virial coefficient per gas mole

$\widehat{B}$—Second virial coefficient (Berlin representation)

$\tilde{B}$—Oscillation damping coefficient

$\mathbb{B}$—First coefficient for radiation problem

$\tilde{\mathbb{B}}$—Non–dimensional first coefficient for radiation problem

c—Turbine blades chord length

c—Wave velocity

C—Third virial coefficient

$\widehat{C}$—Third virial coefficient (Berlin representation)

$\mathbb{C}$—Second coefficient for radiation problem

$\tilde{\mathbb{C}}$—Non–dimensional second coefficient for radiation problem

C_g—Wave group celerity

C_p—Specific heat for real gas at constant pressure

C_p^m—Specific heat for modified gas at constant pressure

C_p^*—Specific heat for ideal gas at constant pressure

$C_{p\,a}$—Specific heat for dry air at constant pressure

$C_{p\,g} = C_p$—Specific heat for real gas at constant pressure

$C_{p\,v}$—Specific heat for water vapour at constant pressure

$\tilde{C}_p$—Non–dimensional specific heat at constant pressure

C_P—Power coefficient

C_s—Speed of sound in air
C_s^*—Speed of sound in ideal gas
C_{sg}—Speed of sound in a real gas
C_T—Thrust coefficient
C_v—Specific heat for real gas at constant volume
C_v^*—Specific heat for ideal gas at constant volume
$C_y = T\left(\frac{\partial S}{\partial T}\right)_y$—Specific heat for constant variable y
$\tilde{C}$—Restitution coefficient
C_2—Inertial resistance factor
d—Turbine porosity
D—Turbine diameter
e—Vapour pressure
e_s—Saturation vapour pressure
$e_0 = 0.611\,\mathrm{kPa}$—Saturation vapour pressure at $T = 273\,\mathrm{K}$
E—Energy term for energy conservation equation
f—Spectral frequency
f_0, f_1, f_2—Temperature correlation functions
f_E—Wave energy flux
$\overrightarrow{F}$—External body forces
g—Acceleration due to gravity
h–Molar enthalpy
h^*–Molar enthalpy of the ideal gas
$\tilde{h}$—Non–dimensional molar enthalpy
h—Water depth
h—Hub-to-tip ratio
h_{owc}—Water depth at OWC location
h_{ref}—Reference water depth
H—Wave height
H_0—Wave height in deep–water
H^*—Enthalpy for ideal gas
H_g—Enthalpy for real gas
I—Unit tensor
k–Wave number
k_0–Initial wave number
k—Thermal conductivity

k_T–Isothermal compressibility factor
kL–Capture length
K—Turbine characteristic number
K_L—Loss coefficient
K'_L—Porous zone equivalent loss coefficient
K_R—Reflection coefficient
$L = 2.5 \cdot 10^6$ J/kg–Latent vaporization heat
L—Work exerted on a system
L—Wavelength
L^{adiab}—Adiabatic work exerted on a system
$m = \frac{C_y - C_p}{C_y - C_v}$—Index m
m_a—Mass of dry air
m_v—Mass of water vapour
$\dot{m}$—Mass flow
M—Molar weight
M_a–Molar weight of dry air
M_v—Molar weight of water vapour
n—General polytropic index
N—Turbine rotation velocity
N—Number of moles
N_b—Number of blades
p—Manometric pressure inside OWC, in general terms
p_a—Pressure of dry air
p_c—Critical pressure
$p_{c\,a}$—Critical pressure for dry air
$p_{c\,v}$—Critical pressure for water vapour
p_g—Pressure of real gas
p_g^{in}—Pressure of real gas during inhalation part of the cycle
p_g^{ex}—Pressure of real gas during exhalation part of the cycle
p_{in}—Pressure at the turbine inlet
p_{out}—Pressure at the turbine outlet
p_r—Reduced pressure, $p_r = p/p_c$
P_0—External total reference pressure
$\widehat{p}$—Complex pressure amplitude in the OWC
P—Total pressure inside the OWC

P—Power
P^*—Non-dimensional pressure drop
P_i—Power for ideal gas formulation
P_r—Power for real gas formulation
P_{owc}—Power in the OWC chamber
P_{PTO}—Power at turbine
$\overline{P}$—Average power
P–Experimental power in turbine for humid conditions
P_{dry}–Experimental power in turbine for dry conditions
P^*–Non-dimensional power
$\mathbb{Q}$—Heat
Q—Volumetric flow rate
Q_{owc}—Volumetric flow rate inside OWC
$\widehat{Q}_{owc}$—Complex OWC air flow amplitude
Q_T—Volumetric flow through the turbine
Q_T^m—Mass flow through the turbine
Q^D—Volumetric flow rate due to diffraction
Q^R—Volumetric flow rate due to radiation
r—Absolute humidity
$R_a = 286.7\,\mathrm{J/K \cdot kg}$—Dry air constant
$R_g = R_0/M$—Real gas constant
R_h—Turbine internal radius (hub)
R_t—Turbine external radius (tip)
$R_v = 461\,\mathrm{J/K \cdot kg}$—Water vapour gas constant
$R_0 = 8.31\,\mathrm{J/K \cdot mol}$—Universal gas constant
RH—Relative humidity
s—Molar entropy
s^m—Molar entropy of the modified gas
s^*—Molar entropy of the ideal gas
$\tilde{s}$—Non–dimensional molar entropy
S—Entropy
S_{rev}—Entropy of a reversible process
S_{rev}^{adiab}—Entropy of a reversible adiabatic process
S—Paddle stroke
S_{ag}—Net air gap section

S_f—Wave spectral density
S_h—Source term of volumetric heat sources and radiation terms for the energy equation
S_i—Source term for the momentum equation
S_m—Source term of added mass for the mass conservation equation
$S|_{in}$—Turbine inlet section
$S|_{out}$—Turbine outlet section
S_{owc}—OWC horizontal section
$S_{turbine}$—Turbine section
S_0—Initial paddle stroke
t—Time
t—Simulation time
T—Temperature
T—Wave period
T—Thrust
T_c—Critical temperature
$T_{ca} = 132\,\mathrm{K}$—Critical temperature for dry air
$T_{cv} = 647\,\mathrm{K}$—Critical temperature for water vapour
T_{freq}—Most frequent peak wave period
T_{in}—Temperature at the turbine inlet
T_{min}—Minimum peak wave period
T_{max}—Maximum peak wave period
T_{out}—Temperature at the turbine outlet
T_{out}^{ad}—Temperature at the turbine outlet following enthalpy conservation (with adiabatic equation)
T_p—Peak wave period
T_r—Reduced temperature, $T_r = T/T_c$
$T_0 = 273\,\mathrm{K}$—Reference temperature
u—Internal energy per mole unit
u^*—Molar internal energy of the ideal gas
$\tilde{u}$—Non–dimensional molar internal energy
U—Blade circumferential velocity
U—Internal energy
U_{ag}—Air gap velocity
U_d—Induction velocity

U_{in}—Air velocity at turbine inlet
U_{out}—Air velocity at turbine outlet
U_{owc}—Vertical water surface velocity inside OWC
U_{paddle}—Paddle displacement velocity
U_{ring}—Velocity in a ring-like section (full section with central hub, without blades)
v—Velocity
$v = V/N$—Molar volume
v^m—Molar volume of the modified gas
v^*—Molar volume of the ideal gas
$\overrightarrow{v}$—Velocity vector
V—Volume
V_g—Real gas volume
V_{owc}—Air volume inside the chamber
V_w—Velocity at the inlet of the stream tube
V_x—Turbine axial velocity
w—Air velocity relative to the turbine
x—Main horizontal direction
x_{paddle}—Paddle displacement along horizontal axis
$\mathbb{Z}$—Compressibility factor per gas mole

Greek

α—Thermal dilatation coefficient
α—Permeability
β—Coefficient depending on turbine characteristics
δ—Porous zone thickness
$\overline{\delta}$—Bedform mean amplitude
δC_p^*—Deviation from ideal specific heat at constant pressure
δH^*—Deviation from ideal enthalpy
Δp—Pressure drop
η—Surface elevation
η—Efficiency
Φ—Non-dimensional flow in turbine
$\gamma = C_p/C_v = 1.4$—Adiabatic index for ideal gas. Heat capacity ratio for air
Γ—Coefficient for diffraction problem

$\tilde{\Gamma}$—Non-dimensional coefficient for diffraction problem
ϵ—Hydrodynamic efficiency in energy extraction by OWC
$\varepsilon = R_a/R_v$—Ratio of gas constants for dry air and water vapour
χ—Coefficient for turbine characteristics
χ_{mol}—Molar fraction of vapour in dry air
$\overline{\lambda}$—Bedform mean length
Λ–Diffusion coefficient
μ—Chemical potential of a gas
μ^*—Chemical potential of the ideal gas
μ—Dynamic viscosity
ψ—Phase
ρ—Density
$\rho = N/V$—Molar density
ρ_a—Dry air density
ρ_g—Real gas density
ρ_g^{in}—Real gas density at the turbine inlet
ρ_g^{out}—Real gas density at the turbine outlet
ρ_w—Water density
ρ_0—Air density outside the chamber
Ψ—Displacement from equilibrium position
σ—Turbine solidity
$\overline{\tau}$—Stress tensor
ω—Relative incoming velocity
ω—Acentric factor
ω—$2\pi/T$, wave frequency

Super index

*—variable for ideal gas
^{m}—variable for modified gas

Sub index

$_0$, $_{ref}$—reference variable

$_g$—variable for real gas